CORROSION AND THERMAL PROTECTION OF METALS WITH THIN FILMS

A Dissertation

by

CAROLYN LONG

Submitted to the Graduate and Professional School of
Texas A&M University
in partial fulfillment of the requirements for the degree of

DOCTOR OF PHILOSOPHY

Chair of Committee,	Jaime C. Grunlan
Committee Members,	Homero Castaneda
	Shoufeng Lan
	Ya Wang
Head of Department,	Guillermo Aguilar

December 2021

Major Subject: Mechanical Engineering

ABSTRACT

The deterioration of metallic components in caustic environments is a problem that has safety and monetary repercussions. The effects of corrosion and thermal degradation on steel are issues that have plagued manufacturers and industrial end users alike, resulting in the need for excessive engineering, monitoring and repair. Even with these drawbacks, the natural abundance and high strength of steel keeps it widely used. Barrier coatings exist to protect the vulnerable metal, acting as insulation between the corrosive agents and high temperatures to ensure the preservation of the desirable mechanical properties. Unfortunately, the best commercially available barrier coatings are either hazardous to the environment, as is the case for corrosion protection, or expensive, such as the ceramic thermal barrier coatings. Layer-by-layer assembly has be extensively used in the creation of polymer nanocomposites thin films for a number of barrier applications. This dissertation describes methods to functionalize polymer-clay thin films to improve their barrier properties for corrosion and thermal protection.

Nanobrick wall coatings have demonstrated high gas barrier properties but do not hold up to corrosive agents. Crosslinking of the polymer matrix and silanization of the substrate prior to deposition improves the corrosion barrier. Crosslinking leads to the reduction of water uptake in the polymer and silanization improves the adhesion at the interface between the substrate and thin film. The combined functionalization creates a successful primer layer when tested in a multilayer insulating coating, which remains effective for at least five days.

Similar nanobrick wall coatings have been used as flame retardant barrier coatings. The addition of an amine salt buffer in the deposition process, and a higher concentration of polymer, generates a thick microscale coating that acts as a heat shield when applied to steel. In this

dissertation, a 14-bilayer film is shown to thermally protect steel, through the creation of a macroscale insulating bubble. The performance is comparable to commercially available ceramic thermal barrier coatings, but is more cost effective and has a simple deposition process.

Char promoting additives are utilized to improve the observed barrier property of these thick nanobrick wall films. These additives influence not only the char generated but also the architecture of the film during pyrolysis. The creation of a more complex structure with varying nano and microdomains, in addition to the macroscale bubble, hinders thermal diffusion and further improves the heat shielding property of these unique coatings.

DEDICATION

To Belle and Talia who persevered through the long hours, kept me company, and could always bring a smile to my face. To my parents, Brenda and Brian, who had more faith in my abilities than I ever could have and provided endless love and support. And to the rest of my family, who supported me through thick and thin on this endeavor, I'll always be thankful for each of you.

CONTRIBUTORS AND FUNDING SOURCES

Contributors

The work herein was performed under the supervision of a committee comprised by: Professor Jaime C. Grunlan as chair and thesis advisor, Professor Homero Castaneda from the Texas A&M Department of Material Science, Professor Shoufeng Lan from the Texas A&M Department of Mechanical Engineering, and Professor Ya Wang from the Texas A&M Department of Mechanical Engineering.

The collaboration in Chapter III was carried out in collaboration with Professor Homero Castaneda from the Texas A&M University Department of Material Science. The collaborative work discussed in Chapter IV was carried out in partnership with Professor Patrick Shamberger and Dion Antao of the Texas A&M University Department of Mechanical Engineering.

Funding Sources

TABLE OF CONTENTS

LIST OF FIGURES

LIST OF TABLES

CHAPTER I – INTRODUCTION

1.1 Background

Metals are prominently used in our industrialized society. Steel is heavily utilized because of its low cost, high strength, and ease of manufacturability.[1,2] Unfortunately, steel is susceptible to degradation, particularly when left exposed to the environment or when subjected to high temperatures. Upon exposure to oxygen or water in the environment, iron oxidizes to form rust.[3] As this process continues, the oxidation eats away at the material, compromising the mechanical strength of the surrounding steel. When exposed to elevated temperatures this oxidation is not only exacerbated, but thermal fatigue can result as well.[4] Thermal fatigue is the initiation of fatigue cracking stemming from drastic changes in temperature experienced by, or within, a metal. This temperature shock creates uneven strain and cracking occurs. In both cases, the iron becomes embrittled and failure becomes much more probable.[5] Methodologies to protect the steel from the deterioration of the mechanical properties is critical given its abundant use.

Many of the commercial methods for metal protective coatings are either toxic to the environment (as in the case of some anti-corrosion coatings) or expensive (as in the case of thermal barrier coatings).[6,7] The most widely used corrosion barrier coatings are multilayer insulating coatings that make use of conversion coatings as the primer layer. However, conversion coatings have been found to be hazardous to the environment and detrimental to people's health and have been largely regulated out of the marketplace.[8] The most effective thermal barrier coatings are ceramic based, with a metallic bond coating, generally deposited via plasma spray coating.[9] While these coatings are highly effective, they are also complex and costly and therefore only used in specific applications such as on gas turbine blades, where the benefits outweigh the costs. Both

applications can benefit from more environmentally-benign and cost effective alternatives. Polymeric nanocomposite coatings are films that contain a polymeric matrix and inorganic filler that, when deposited using layer-by-layer (LbL) assembly, have demonstrated excellent gas barrier and flame retardant properties.[10–12] LbL assembly allows for the creation of a thin film that is highly tailorable by adjusting processing parameters such as polymer species, ionic strength, and solution pH or concentration.[13] Further, with the addition of clay nanoparticles, a nanobrick wall structure can be created that greatly improves the barrier properties of the film.[10] These coatings, paired with additional functionalization, can offer comparable properties to traditional corrosion and thermal barrier coatings, while also being cost effective, environmentally-benign, and easy to deposit as a surface coating on a wide range of substrates.[14]

1.2 Objective and Dissertation Outline

The work described herein aims to provide environmentally-benign and cost-effective coatings for protecting metallic substrates from caustic environments. This is accomplished through functionalization of polymer-clay films deposited via layer-by-layer assembly.

Chapter II provides an overview of corrosion and thermal fatigue, along with commonly used methodologies for protecting steel from these phenomena. Conversion coatings for corrosion multilayer barrier coatings and thermal barrier coatings for the protection of metals are introduced and the problems with each are highlighted. Polymer nanocomposites are detailed, along with how layer-by-layer deposition can improve these films. Finally, different types of functionalization for polymer nanocomposite coatings are reviewed, including crosslinking, silanization, the addition of small molecule additives such as amine salts, and the role intumescence can play in providing thermal protection.

Chapter III demonstrates the functionalization of layer-by-layer films to improve the nanocoating for use as a corrosion barrier primer. Polyethylenimine (PEI) and vermiculite clay (VMT) are used in the layer-by-layer deposition of a 300 nm thick nanobrick wall thin film. The corrosion prevention performance of the coating is improved through crosslinking with glutaraldehyde (GA) and silanization of steel with aminopropyltriethoxysilane (APTES) prior to film deposition. Finally, the nanobrick wall film is tested with an epoxy topcoat, to demonstrate the viability of the recipe as a primer. Epoxy with the crosslinked and silanized nanobrick wall primer coating outperforms a neat epoxy coating.

Chapter IV demonstrates the use of a "thick growing" polymer nanocomposite utilizing an amine salt for the creation of a novel and efficient heat shielding coating. A 35 µm coating, composed of 14 deposited bilayers of tris(hydroxymethyl)aminomethane (THAM)-buffered PEI and VMT, decreased the maximum temperature observed on the back side of a 0.32 cm thick steel plate by over 100 °C when heated with a butane torch. The efficiency of the film is attributed to the creation of a macroscale ceramic bubble in tandem with the nanocomposite coating properties, which provides heat shielding for the steel substrate.

Chapter V demonstrates improved thermal resistivity of the polymer nanocomposite heat shielding coating through various coating additives. THAM, pentaerythritol (PER), and ammonium pentaborate (PB) are combined with polyethylenimine in a polymer-clay coating and the resultant film growth and the thermal resistivity are measured. The salts, THAM and PB, are found to contribute most to the overall growth of the films, generating an increase of film thickness of 50% or more. However, PER has a greater impact on the heat shielding. When combined with THAM the coating on steel can achieve a temperature differential of over 140 °C due to a layering effect that occurs within the architecture of the macroscopic insulation bubble.

Chapter VI is a summary of this dissertation work and describes future work that can be undertaken to evaluate the versatility of these films and ultimately improve viability of these films for industrial use. The dissertation demonstrates the power of layer-by-layer assembly in creating nanobrick wall thin films for applications in corrosion barrier and heat shielding. Different strategies have been evaluated to functionalize these films to improve the coating performance for vastly different barrier applications. The proposed future work includes investigating alternative substrates for heat shielding protection. Preliminary experimentation has demonstrated the ability of the heat shielding coating, detailed in chapter IV, to protect a carbon fiber composite from thermal degradation. Additional testing to determine the extent of mechanical property preservation is outlined. Another proposed study investigates utilizing polyelectrolyte complexes (PEC) as an alternative to LbL assembly for both corrosion resistance and heat shielding. PEC have already been demonstrated as viable alternatives in gas barrier and flame retardant applications.[15–17] The use of this type of deposition process for corrosion barrier and heat shielding is a natural progression of the research.

CHAPTER II – LITERATURE REVIEW

2.1 Hazards of Metallic Degradation

Virtually every industry has metals integrated into their products and services, from transportation to construction, energy and beyond. Unfortunately, this prevalent use of metals has resulted in costly issues proceeding from some of the less favorable aspects of metals.[18,19] Among these unassailable characteristics include a metal's tendency to corrode and experience thermal fatigue. Ultimately, each of these traits has the potential to degrade the mechanical properties of metals (reduction in ultimate stress, torsion resistance, cyclic fatigue, etc.).[20,21] This mechanical deterioration has safety consequences along with large economic ramifications.[3,22,23] The effects of corrosion consumes 3% of the world's gross domestic product annually.[24] Part of this impact stems from the need for excessive, and sometimes redundant, engineering, maintenance, and replacement of materials over time to prevent failure.[25] In the event of catastrophic failure there is often extensive repair work, and the associated cost, and in extreme cases loss of life.

2.1.1 Corrosion

One of the primary drawbacks to the prevalent utilization of metals is their susceptibility to corrosion, which stems from the tendency to exchange electrons and oxidize.[26,27] Invariably, when exposed to the environment, metals do not stay in their refined form. Rather, there is a slow exchange of electrons with corrosive agents (i.e. O_2, H^+, H_2O and Cl^-) that results in corrosion causing the embrittlement of the remaining metal.[19,24] The rate at which this occurs is dependent on an equilibrium between opposing electrochemical reactions: (1) the anodized reaction, in which the metal is oxidized and electrons are released into the metal, and (2) the cathodic reaction, in which a solution species is reduced and electrons are removed from the metal. This process is

exacerbated in harsh environments, where metals are exposed to salt water, acids or alkalies.[3] The most well-known form of corrosion is the rusting of iron and steel. Metals such as zinc and aluminum corrode more readily than iron, but the oxides formed from their corrosion create a coating that protects the metal from further attack. Conversely, the rust biproduct from the corrosion of iron and steel, shown in **Figure 2.1**, is brittle and easily flakes off the surface of the metal, causing continual exposure of a fresh, vulnerable, surface. This allows for the continual deterioration of the mechanical properties due to embrittlement of the steel.

Rust: $Fe_2O_3 (XH_2O)$

O_2

Fe^{2+}

OH^-

e^- e^-

Anode:

Cathode:

$Fe \rightarrow Fe^{+2} + 2e^-$

$O_2 + 2H_2O + 4e^- \rightarrow 4OH^-$
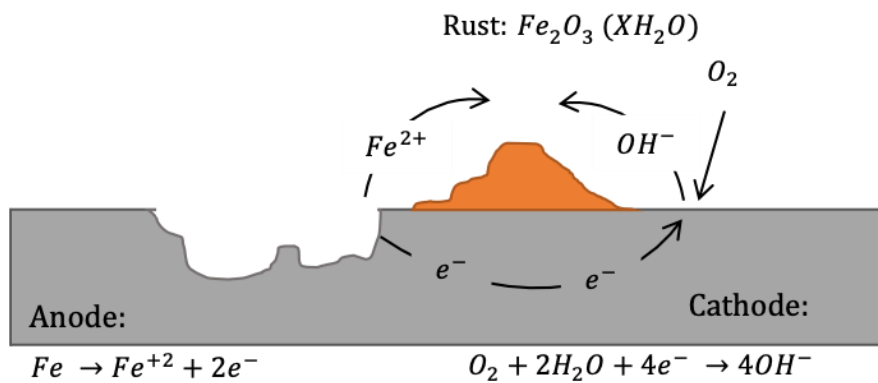
Figure 2.1. The corrosion process of steel when exposed to corrosive agents in the environment.

2.1.2 Thermal Fatigue

The relatively low thermal resistance that metals exhibit is another difficulty faced by some industries that rely on metals for their mechanical strength and natural abundance.[4,28] Heat is transported as the thermal energy causes vibrations at the atomic level which transfers from atom to atom across the bulk, called conductive heat transfer. Materials have a coefficient of thermal conductivity, with higher coefficients related to higher levels of conductive heat transfer through the material. The rate of heat conduction is dependent on the heat the object is exposed to, the thermal conductivity of the material, and the emissivity of the material (i.e. the ability to radiate

6

heat).[7] The tendency of metals to readily conduct heat is due to their relatively nonexistent band gap, which allows for easy transfer of electrons.[29] While in some instances, such as electronics or heat sinks, this ready conduction of heat is a desirable trait, there are other times when the high strength of metals is required without the high conductance. When exposed to temperatures above 500 °C, metal parts and components respond rapidly, and their mechanical properties can be compromised.[30] In ductile materials, an increase in temperature will decrease the number of cycles to failure, reducing the lifespan of the material.[31] This thermal fatigue results from uneven stresses and strains due to thermal shock, spatial temperature gradients within a material, and exposure to extreme temperatures under constrained thermal deformation.[5,32–34] **Figure 2.2** is a schematic showing the cracking that results from thermal fatigue. These cracks result in the embrittlement of the steel. This decrease in mechanical strength is detrimental in many applications, such as automotive, structural support, metal roofing, and metal piping applications.[35]
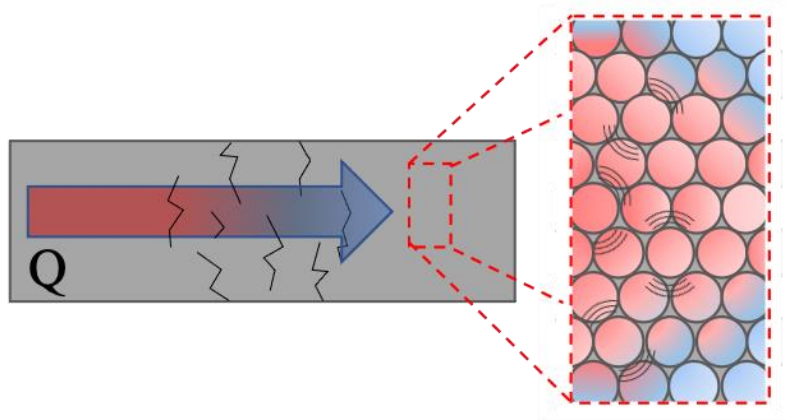
Figure 2.2. Thermal fatigue schematic of steel, when cracking results from thermal exposure.

2.2 Barrier Coatings

2.2.1 Corrosion Barrier Coatings

Several strategies, including cathodic protection, corrosion inhibiting additives, and multilayer insulating coatings, have been developed to prevent or suppress corrosion.[26,36,37]

Cathodic protections makes use of the electrical nature of corrosion, offering protection through an alternative current.[3] There are two types of cathodic protection: impressed current and sacrificial anode, shown being used in tandem in **Figure 2.1(a)**.[38] Impressed current cathodic protection uses anodes that are connected to a power source that provides the electrical flow. The current provided polarizes the surface of the base metal to the thermodynamic potential of the anode. As a result, the corrosion current no longer flows because the cathode and anode potentials are equal. Sacrificial anode cathodic protection makes use of a second, more active metal that corrodes in place of the base metal.[39] This protective metal has a stronger electrochemical potential so it preferentially exchanges electrons with the environment. Another avenue for corrosion prevention are smart coatings containing corrosion inhibiting agents that, when exposed to a specific parameter, such as pH or O_2 content, activate to stop the onset of corrosion.[39,40] This can be in the form of a self-healing coating or an additive that creates an additional barrier once the original coating is breached (**Figure 2.1(b)**). The final type of corrosion prevention is a multilayer insulating coating. This coating generates a physical barrier between the base metal and the corrosive environment, and generally consist of a pretreatment primer layer, several intermediate layers, and a topcoat, as shown in **Figure 2.1(c)**.[41,42] Among these strategies, applying multilayer coatings to a metal surface is the most common mechanism employed due to its low cost and easy application.
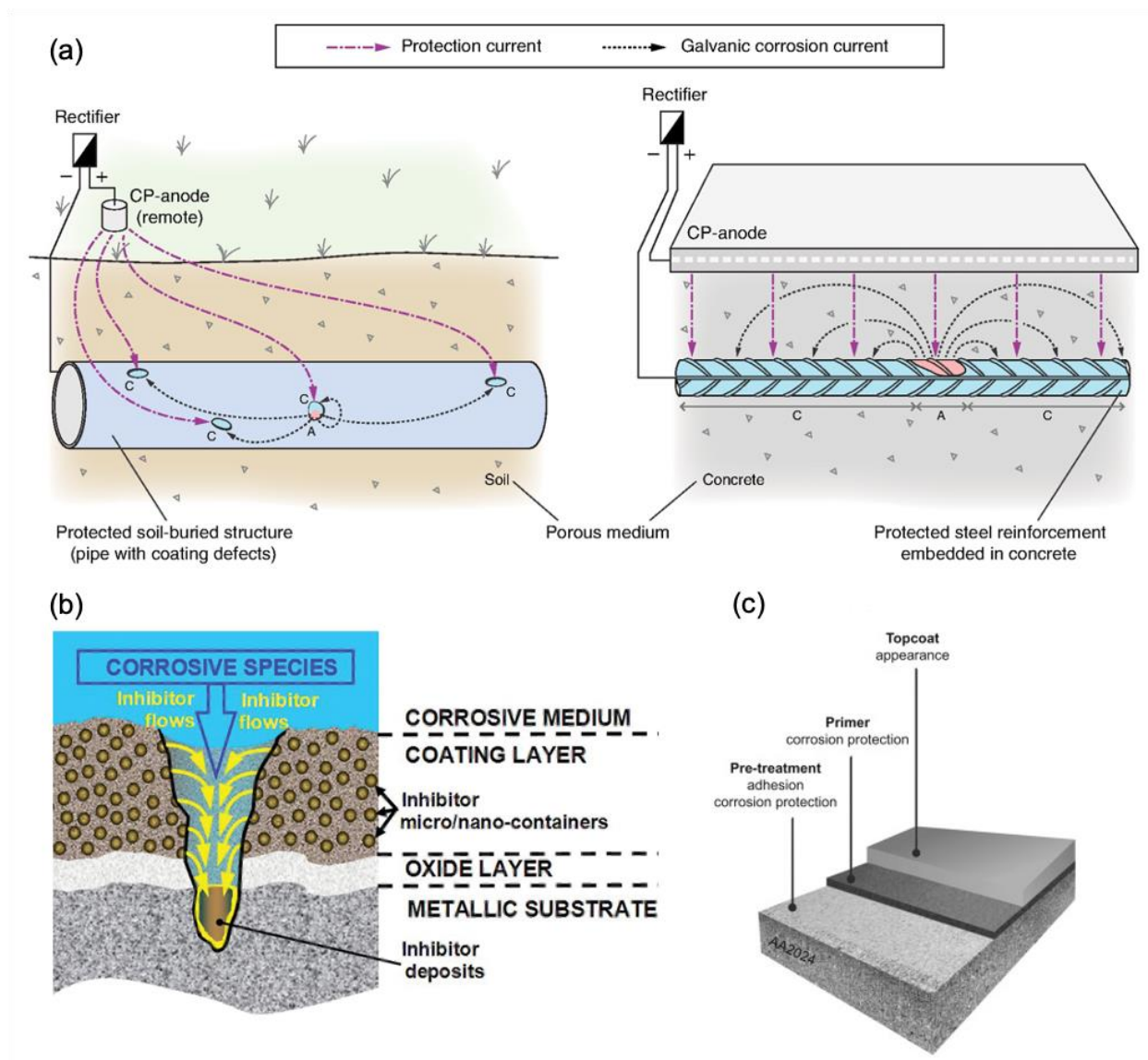
Figure 2.3. Schematic depiction of the different mechanisms for corrosion protection: (a) cathodic protection (reprinted with permission from [reference 38]),[38] (b) the self-healing effects of corrosion inhibition (reprinted with permission from [reference 40]),[40] and (c) multilayer insulating coatings (reprinted with permission from [reference 42]).[42]

Traditional primer layers used in multilayer coatings on various metals make use of conversion coatings.[43,44] For protecting steel, the most effective primer layers are phosphate conversion coatings (i.e. zinc phosphate), which promote corrosion resistance through improved adhesion between a topcoat layer and the steel substrate [44,45]. Unfortunately, phosphate conversion coatings have been found to be harmful to the environment and human health, with many

municipalities limiting the amount of phosphate that can be discharged into the environment.[46] Consequently, environmentally-benign pretreatment coatings have received significant attention in recent year to replace these conversion coatings.[47–49]

2.2.2 Thermal Barrier Coatings

One method employed to impede heat transfer through a metal is by utilizing surface coatings that stem thermal transport to the metal. These thermal barrier coatings (TBC) must exhibit low thermal conductivity, low surface absorptivity (i.e., low emissivity), and porous micro and nanostructures.[9,50,51] All of this allows for the maximization of temperature difference between an exposed surface and the vulnerable metal substrate. This coupled with maximizing failure time, or the time it takes for the substrate to reach a prescribed temperature, are active variables evaluated in thermal barrier coatings to increase the life of the underlying substrate.[50,52] The ability to expose metals to higher temperatures leads to greater component durability that in some applications, such as gas turbine engines, increases the efficiency of the system and decreases the overall cost.[53,54]

There currently exist two main coating technologies for creating a thermal barrier to heat transfer across a metal substrate. The most common type of TBCs are ceramic-based, often utilizing zirconium oxide as a thermally grown oxide layer in a multilayer structure with a metallic bond coat (**Figure 2.2(a)**).[55–57] This type of ceramic layer exhibits a high thermal resistivity across 100 to 200 µm, partly because of relatively low thermal conductivity ($0.8-2.25$ W·m^{-1}·C^{-1}), that creates an obstacle to thermal transport, prolonging the life of the metal and allowing for operation both in high-temperature and in oxidizing conditions.[58–60] While zirconia coatings offer a high degree of protection to under extreme temperature (e.g., temperatures in excess of 1400 °C found inside turbine engines), they are also expensive and involve somewhat complex processing.[61] As

a result, these oxide layers are primarily used in high-value applications, such as gas turbine blades.[62]
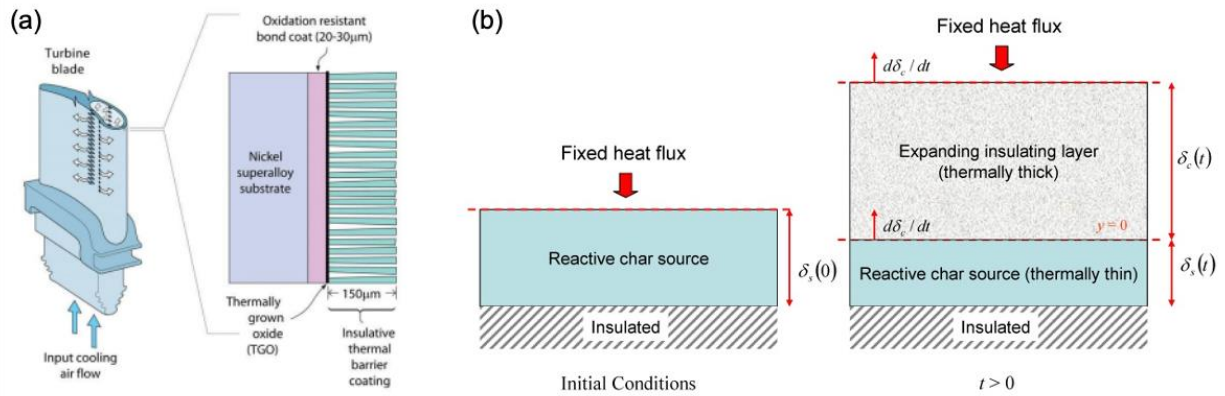
Figure 2.4. Current types of thermal barrier coatings: (a) ceramic based (reprinted with permission from [reference 57])[57] and (b) polymeric based that intumesce when exposed to heat (reprinted with permission from [reference 52]).[52]

A second, more novel type of TBC is a low-cost polymer-based film that intumesces to form a macroscale insulating layer when exposed to high temperatures (**Figure 2.2(b)**).[52,63–65] Standalone polymers are not ideal thermal barriers due to their low thermal stability, with most degrading under relatively low temperature (>200 °C) conditions.[66] However, the ability of a polymeric systems to intumesce, expand, and form an insulating char layer, has made them a viable thermal barrier in some circumstances.[12,67] The intumesced layer is porous, suppressing heat transfer by forcing thermal transport through the low thermal conductivity gas voids and polymer nanocomposite coating.[68] Protecting structural steel in particular has been a focus of this research, creating a passive coating that offers protection in extreme cases and prolonging the mechanical property of the steel in the event of fire.[69–71] These intumescent coatings are expendable, meant to protect the underlying substrate during extreme catastrophic events. Similar coatings have been studied for use on textiles, focusing on the need to retard the spread of flames by utilizing nanocomposite coatings that intumesce.[11,12]

2.3 Polymer Nanocomposite Coatings

Polymer nanocomposite coatings are utilized in a wide range of applications including gas barrier, heat shielding, thermoelectrics, and dielectrics.[72–76] Comprised of a polymeric matrix and an inorganic filler species the properties can be tailored depending on materials used, substrate, processing conditions, and deposition technology.[77] The type of nanofiller and morphology of the dispersion have a large impact on the resultant properties. Some common nanofillers include lamellar clays, carbon nanotubes, graphene, nanocellulose, and halloysite.[72] **Figure 2.4** shows three types of polymer composite morphologies: (1) conventional composites where the polymer and filler are separate phases, (2) intercalated nanocomposites where a single or multiple polymer chains are able to intercalate between the fillers, and (3) exfoliated nanocomposite when the filler is completely and uniformly dispersed in the continuous polymer matrix.[78] The influence the nanofillers have on the end properties is attributed to multiple factors including the polymer used, the nature and type of nanofiller, concentration of the nanofiller within the polymer matrix, and the particle orientation and distribution.
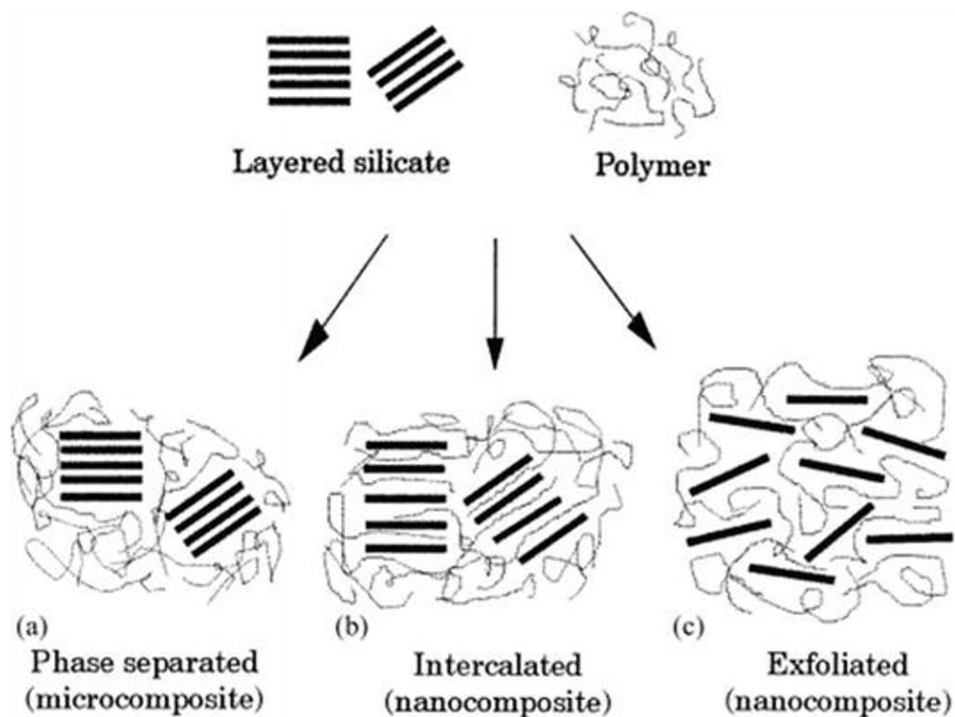
Figure 2.5 Polymer nanocomposite configurations: (a) conventional phase separated composites, (b) intercalated nanocomposites, and (c) exfoliated nanocomposites (reprinted with permission from [reference 78]).[78]

Silicate clay nanoplatelets have been used extensively in polymer nanocomposite thin films.[75] Common silicate clays include montmorillonite (MMT), vermiculite (VMT), and laponite. Clays are effective nanofillers because of their lamellar structure, high specific area, low cost, and high cation exchange capacity.[72] A well-ordered multilayer morphology and high loading of the nanoclays within the polymer matrix results in improved thermal, mechanical, and gas barrier properties.[79] Additionally, the use of higher aspect ratio inorganic loading increases these properties as this allows for greater contact area with the polymer matrix, increasing the load transfer from the matrix to the filler. One of the most effective ways to achieve this ordered structuring is through layer-by-layer assembly deposition.

2.3.1 Layer-by-layer assembly

Layer-by-layer (LbL) assembly is a water-based technique that has been extensively used to generate thin film polymeric coatings on solid substrates.[80,81] LbL coatings are produced mainly through electrostatic interactions, although hydrogen bonding and covalent bonding can be used to achieve additional functionality.[82–84] The assembly process begins by first exposing a negatively charged substrate to a solution containing a cationic polyelectrolyte and then subsequently exposing it to an anionic solution with predetermined rinse and dry steps between to remove excess, loosely adhered material.[85] This is considered one bilayer (BL) and the steps are repeated, building on previous layers, until a desired number of BLs is obtained. End properties are tunable by adjusting the electrolyte species,[86,87] pH,[88,89] ionic strength,[90] molecular weight,[91,92] solution concentrations,[93] processing steps,[94] temperature,[95] charge density,[96,97] or adding fillers to create a polymer nanocomposite.[98,99] Additionally, by using three or four materials sequentially a trilayer or quadlayer system, respectively, can be formed allowing for additional functionality.[100,101]
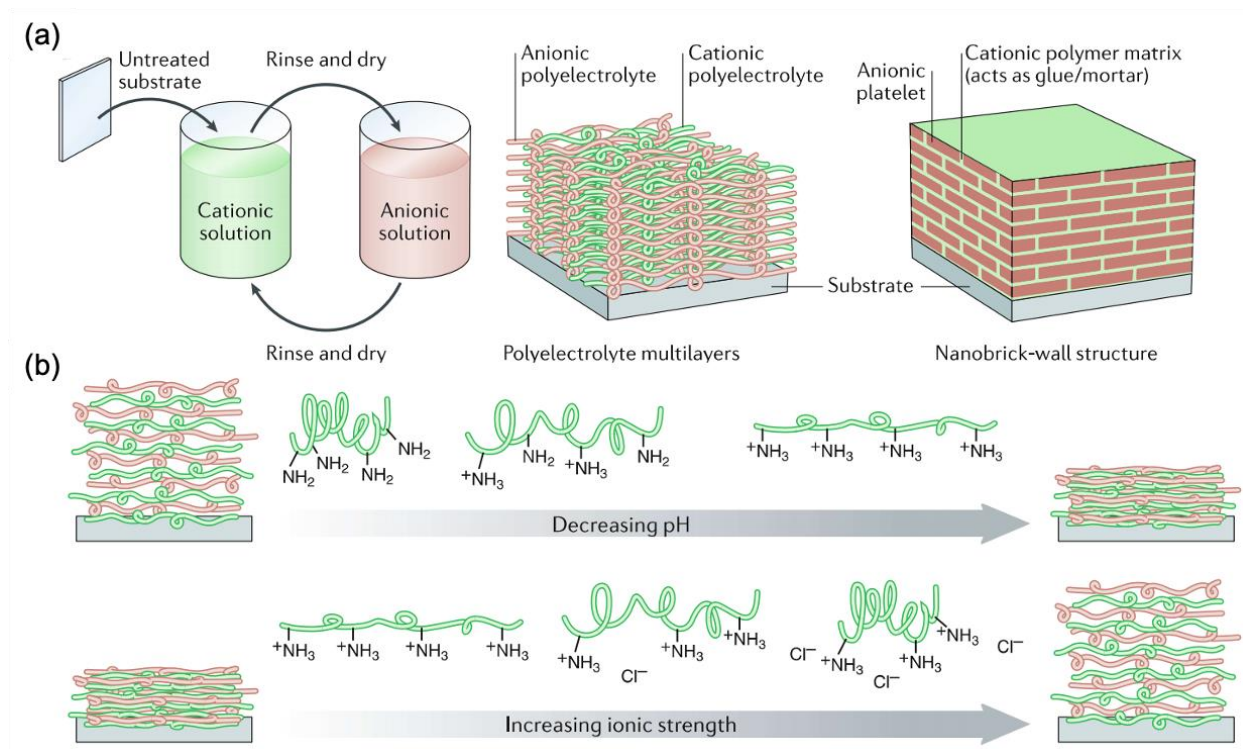
Figure 2.6. Schematic representation of (a) the layer-by-layer assembly process and resulting polyelectrolyte multilayers and polymer nanocomposite, and (b) the influence pH and ionic strength of the polyelectrolyte species can have on the thickness of the film (reprinted with permission from [reference 12]).[12]

2.3.2 Nanobrick Wall Structure

The addition of fillers, and the subsequent creation of a polymer nanocomposite, allows for nanoscale control with layer-by-layer assembly. Other methodologies for producing polymer nanocomposites only achieve filler loading of about 30 to 40 % and clay filler agglomerates within the polymer matrix.[75,102] Utilizing LbL assembly, filler loading levels have exceeded 90%.[103] In addition to this high filler loading, the layer-by-layer technique generates high alignment of clay platelets within the coating, called a nanobrick wall structure (**Fig. 2.7(a)**). This creates a passive barrier mechanism shown to be highly effective in gas barrier, flame retardant, and corrosion applications.[49,101,104,105] The high barrier is gained through highly exfoliated and uniformly dispersed high aspect ratio platelets that orient parallel to the substrate.[10] These favorably aligned

15

platelets create a long diffusion pathway, referred to as the tortuous path, as shown in **Figure 2.7(b)**, that decreases permeability of molecular species. Increasing the lateral dimension, decreasing the thickness of the filler (i.e. increasing the aspect ratio), and/or increasing the percent of clay content within the film increases tortuosity (**Fig. 2.7(c)**). The mathematical representation for the tortuosity is given by the relative permeability:

$$\frac{P_o}{P} = 1 + \mu\alpha^2\left(\frac{\phi^2}{1-\phi}\right)$$ (1)

where P_o is the polymer matrix permeability, P is the composite permeability, μ is a filler geometric factor, α is the filler aspect ratio and ø the volume fraction of the filler.[106]
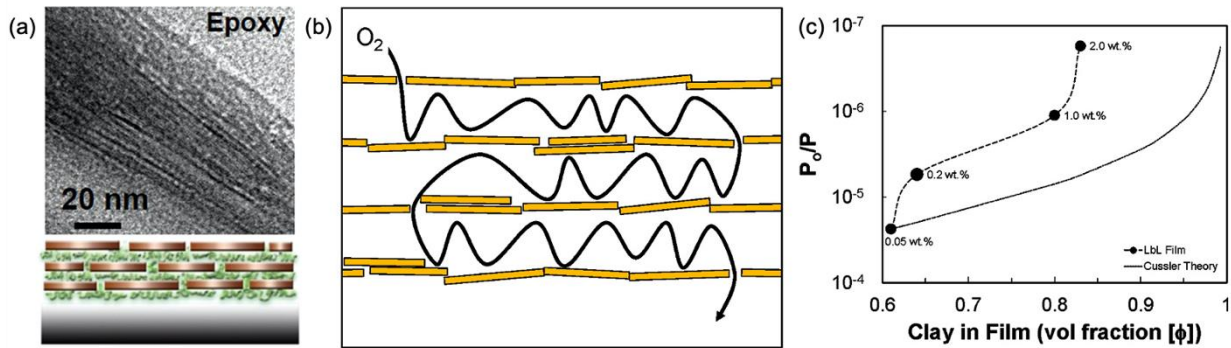
Figure 2.7. (a) TEM cross-sectional image of a nanobrick wall structure and corresponding schematic (reprinted with permission from [reference 49])[49], (b) schematic of tortuosity, and (c) effect of volume fraction of clay in the film on the tortuosity factor (reprinted with permission from [reference 103]).[103]

2.4 Functionalization of Polymer Nanocomposites

Although the effectiveness of layer-by-layer is far reaching and allows for a lot of customizability within the bounds of the assembly technique, additional benefits can be derived from functionalization of the polymer nanocomposite. Common methodologies for improving the polymer nanocomposite performance include crosslinking of the polymer matrix, silanization of the substrate or filler, and the addition of small molecule additives to the solutions.

2.4.1 Crosslinking

Crosslinking is the chemical joining of two polymer chains, often through covalent bonding, to form a larger polymer network.[107] The generated network reduces the free volume within the film through more dense packing of the molecular lattice. Different methods of crosslinking include chemical, thermal, and UV.[108–112] Crosslinking can have a number of different effects on polymer properties, including increasing thermal stability, providing a more rigid structure that increases the mechanical strength, and decreasing the solubility of the polymer.[113–115] The inherent hydrophilic nature of most polymers used in layer-by-layer assembly make these polymers susceptible to water absorption and film swelling.[116] This will eventually result in an increase in the free volume of the polymer, which allows for permeants to diffuse through the film more quickly in high humidity or aqueous environments. Crosslinking helps prevent water absorption and consequently improves the barrier properties of films under such high humidity or aqueous conditions, as shown in **Figure 2.8**.[108,117]
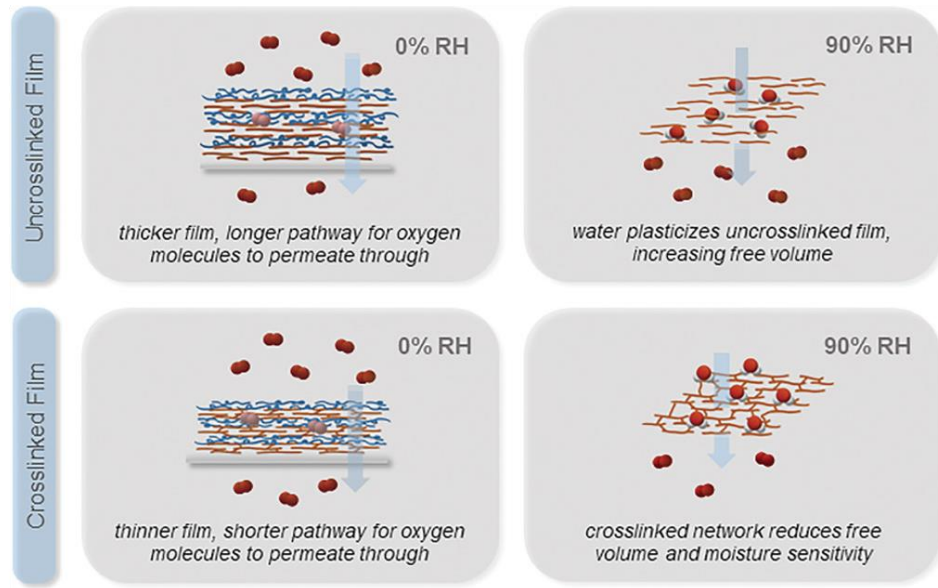
Figure 2.8. Crosslinking schematic detailing moisture resistance of uncrosslinked versus crosslinked films (reprinted with permission from [reference 116]).[116]

2.4.2 Silanization

Silanization involves the functionalization of a surface with a silane. Silanes are hybrid molecules that contain a hydrolytically sensitive center that reacts with inorganic substrates.[118] Most organosilanes have one organic substituent and three hydrolysable substituents. Silanization is driven by the hydrolysis of these substituents. Alkoxy groups (i.e. ethoxy or methoxy) hydrolyze in the presence of water and are converted to hydrophilic silanol groups (Si-OH) that can bond with hydroxide groups on a metal's surface (Me-OH) through hydrogen bonding.[119,120] A condensation step then occurs at the interface, which results in metallo-siloxane covalent bonds (Me-O-Si). **Figure 2.9** is a schematic of this process, demonstrating the use of aminopropyltriethoxysilane (APTES) in functionalizing graphene oxide (GO).[121] This silanization was shown to improve the bonding strength between the GO and a polymer matrix, which in turn improved the overall mechanical properties of the polymer nanocomposite. Silane functionalization can range from altering surface properties to promoting hydrophilicity,[118] creating a more hydrophobic surface,[122] used as an interface to promote adhesion,[119] and as a protective coating to improve durability.[123]
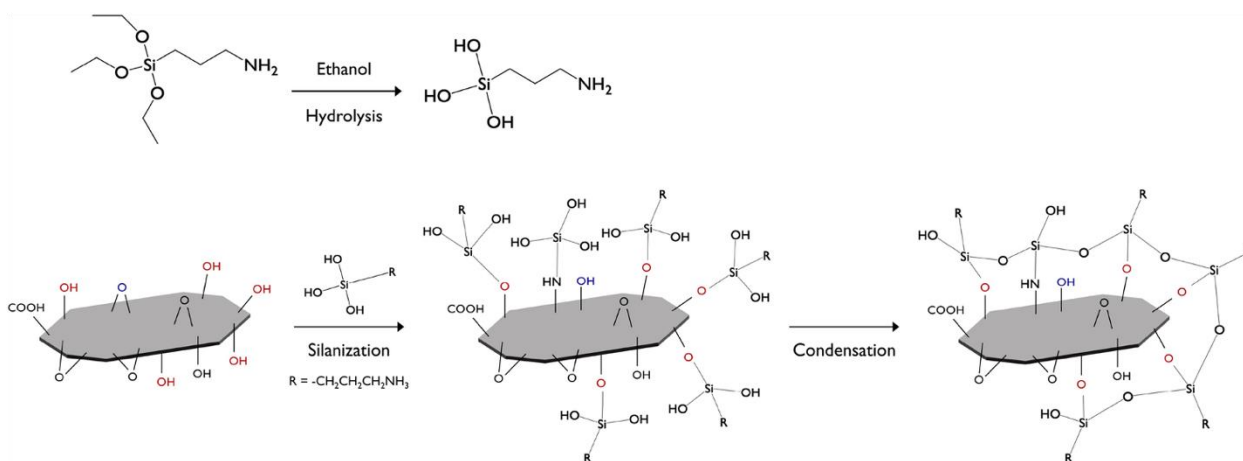
Figure 2.9. Schematic of the silanization of graphene oxide with aminopropyltriethoxysilane (reprinted with permission from [reference 121]).[121]

2.4.3 Small Molecule Additives

Small molecule additives have been utilized to great effect in polymer nanocomposite coatings. These additives improve the properties for applications such as semiconductors, flame retardants, and thermal barrier coatings.[124–126] Not only do these additives become incorporated into the bulk of the composite, but they also often interact with the other components influencing both the growth of the material and the end application.[127,128] Small molecule additives have been used to promote nucleation, generate better crystallization, improve self-assembly of polymers, induce crosslinking, and increase film thickness[129–132] Amine salts, such as tris(hydroxymethyl)aminomethane (THAM), have been shown to increase the thickness of polymer films through charge screening.[133] For a polymer system with clay filler, the amine salt also influences the deposition of the nanoclay platelets. Previous studies have shown that akylamines interact with the surface of the nanoclays allowing for intercalation of polymer between dispersed nanoclay, with the result of multiple stacks of clay being deposited in a single coating step.[134] The resulting film thickness is over an order of magnitude greater than its thin clay counterpart (i.e. coating without amine salt), with the thickness of 10 BLs of the thick clay system being 5-6 µm and 10 BLs of the thin system being around 80 nm.[135,136] Another example of the use of small molecule additives is pentaerythritol (PER), which has been used extensively as a char promoter in flame retardant applications. The addition of a char promoter to a film is vital in the creation of an intumescent system that, in turn, creates a thermal barrier under the right conditions.[137]

2.4.4 Intumescent Polyelectrolyte Systems

Intumescence is a form of active chemistry whereby the polymer swells when heated to create a protective barrier for the material underneath. This is an important mechanism in flame

retardant systems, resulting in an insulation layer that protects the flammable substrate.[138–140] The intumescent mechanism requires an acid source (such as ammonium polyphosphate), blowing agent (such as melamine), and carbon source (such as pentaerythritol) acting together in the condensed phase to form a bubbled char layer.[12,65] The process starts with the release of an inorganic acid as the material begins to heat (<250 °C). The acid then reacts with the carbonization agent, via dehydration, to form a carbonaceous layer on the surface. At the same time the blowing agent undergoes pyrolysis and releases non-flammable gases, such as N_2 and CO_2. These gases, in addition to driving away hot convective air, cause the char layer to expand and contribute to the porous architecture as gases trapped within the char layer form bubbles.[30] A solidified intumescent char layer then results as crosslinking and condensation create a stable, protective shell on the surface of the substrate. This thick char layer insulates through low thermal conductivity and a porous architecture, reducing thermal transport to the vulnerable substrate.[141]
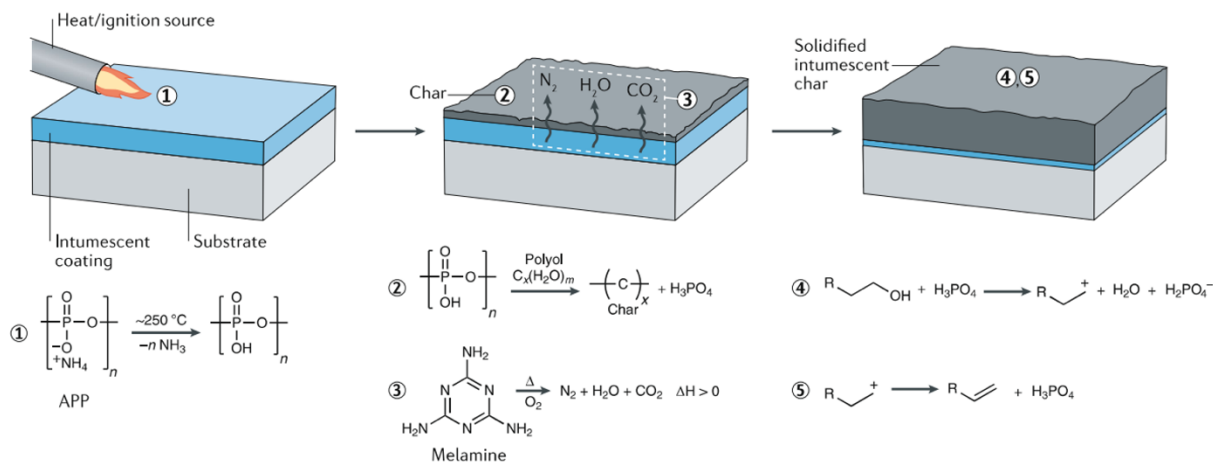
Figure 2.10. Schematic of the intumescent process with ammonium polyphosphate (APP) as the acid source, polyol as the carbon source, and melamine as the blowing agent (reprinted with permission from [reference 12]).[12]

20

CHAPTER III – CROSSLINKING AND SILANIZATION OF CLAY-BASED MULTILAYER FILMS FOR IMPROVED CORROSION PROTECTION OF STEEL*

3.1 Introduction

Thin organic-inorganic hybrid films can provide a barrier against corrosive species (i.e. water, oxygen, and aggressive ions).[8,142] Inorganic fillers, especially clay nanoplatelets, have attracted attention due to their high in-plane strength and stiffness coupled with their impermeability to various gas species.[143–145] Layer-by-layer (LbL) deposition of polymer-clay nanocomposite thin films generates a nanobrick wall structure.[106] This structure forms a tortuous pathway, hindering the diffusion of small molecule species. The nanobrick wall has proven effective in gas barrier and moisture barrier applications, which makes it a viable candidate as an effective corrosion resistant coating.[144,146,147] The present study focuses on improving a LbL deposited primer layer by reducing water transport across the film through crosslinking of the polymer mortar and improving film adhesion to the steel substrate through silanization. Viable pretreatment layers exhibit both improved adhesion between an intermediate or topcoat and the vulnerable substrate and independent corrosion resistance.

The nanobrick wall structure is formed by alternately depositing layers of cationic polyethylenimine (PEI) and anionic vermiculite (VMT) clay on steel. This PEI/VMT multilayer system has previously been shown to exhibit high gas barrier and some corrosion resistance stemming from the strong ionic bonding and the nanobrick wall structure that hinders corrosive

species diffusion.[147] The high aspect ratio of VMT results in increased gas barrier properties over other clay alternatives, such as montmorillonite (MMT) or laponite (LAP).[148] This thin film is crosslinked with glutaraldehyde (GA) to prevent water absorption and improve chemical, mechanical, and thermal stability.[114,149] A silane pre-treatment with aminoproplytriethoxysilane (APTES) promotes improved adhesion between the primer and steel, reducing delamination and microscale defects in the coating.[119,150] This silanized and crosslinked nanobrick wall coating was tested as part of a multilayer system, utilizing a bisphenol-A based epoxy topcoat. By combining the already corrosion resistant epoxy with this nanocomposite primer, an improved and prolonged resistance to corrosive species is demonstrated. While crosslinking and silanization have been demonstrated to improve barrier properties, this study is the first time the methodologies have been combined to demonstrate improved corrosion resistance. This improvement demonstrates the viability of the functionalized nanobrick wall film to be used as an environmentally-benign primer layer in an multilayer insulating barrier coating for the protection of steel.

3.2 Experimental

3.2.1 Materials and Substrates

Branched polyethylenimine (M_w = 25,000 g/mol), glutaraldehyde (25 wt%), and (3-aminopropyl)triethoxysilane were purchased from Sigma-Aldrich (Milwaukee, WI). Microlite 963++ vermiculite clay (7.8 wt % in water) was purchased from Specialty Vermiculite Corp (Cambridge, MA) and diluted to a 1 wt % suspension. Deionized (DI) water (with a resistivity equivalent to 18 MΩ) was used to prepare all solutions and rinses. All solutions were left at their intrinsic pH. 15.24 × 15.24 × 0.08 cm plates of A36 ground low-carbon steel was purchased from McMaster Carr (Aurora, OH) and cut to 2.54 × 2.54 cm coupons for coating. Metal substrates were cleaned by rinsing with DI water, methanol, and again DI water prior to bath

sonicating in DI water and then isopropanol (IPA) for 2 minutes each, with IPA rinses between, and dried with filtered air. The steel was then immersed in a 1 M sodium hydroxide and 100 mM sodium nitrite solution overnight to passivate the surface for better adhesion prior to deposition. Bisphenol A based epoxy (DER-671-X75) and a polyamide hardener (Versamide 140, Olin, Clayton, OH), were combined at 82.4 wt % and 17.6 wt %, respectively, and used as a topcoat.

3.2.2 Thin Film Preparation

Steel substrates were coated with bilayers of PEI/VMT using layer-by-layer (LbL) assembly, which was carried out with a home-built robotic system [151]. Films were assembled by first immersing the substrate into a 0.1 wt% PEI solution for 1 minute, followed by rinse and dry to remove any excess polymer. From there, the substrate was immersed in the 1 wt% VMT solution for 1 minute and then rinsed and dried again, which completes one bilayer (BL). This procedure, shown schematically in **Figure 3.1**, was then repeated until the desired number of bilayers were deposited. Epoxy was coated using a birdbar with a 5 mil gap (127 µm) to generate a 2.5 mil (63.5 µm) thick coating once dry.
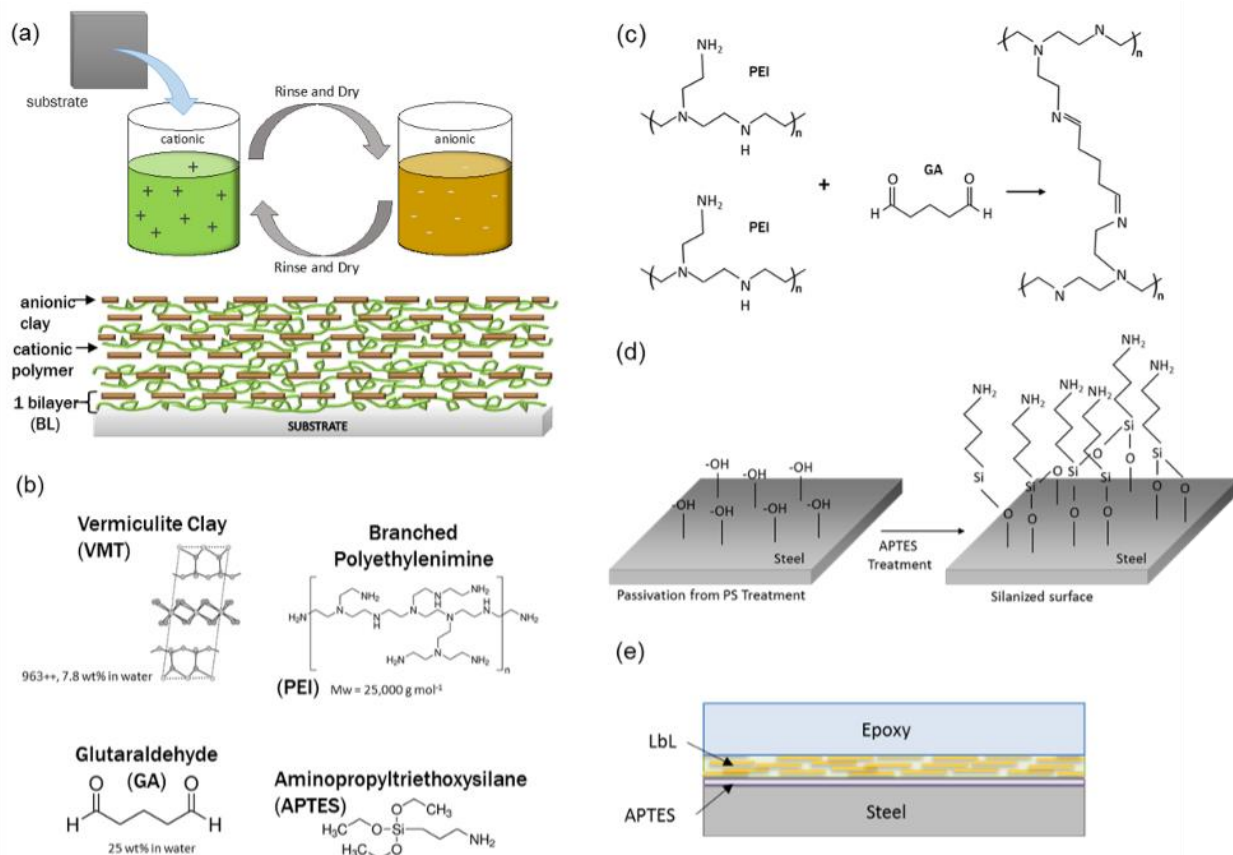
Figure 3.1. (a) Schematic of layer-by-layer (LbL) deposition process and corresponding nanobrick wall film and (b) materials used. Schematics of (c) PEI crosslinking using GA and (d) silanization of steel with APTES and (e) the final multilayer coating system.

3.2.3 Crosslinking and Silanization

Following LbL deposition, films were immersed in GA solutions of varying concentration to allow for crosslinking of the PEI layers, using immersion times of 1, 4 and 16 hours. Additionally, the number of deposited BL (i.e. the thickness of the film) before crosslinking was evaluated by first comparing films crosslinked at 10, 15, and 20 BL. Films were then corrosion tested when crosslinked at 15 and 30 BL and compared to films crosslinked at only 30 BL.   Prior to additional LbL deposition or testing, the sample was immersed in a 0.1 M sodium borohydride (NaBH4) solution (in ethanol) for one hour to reduce the Schiff base formed between GA and PEI.[109] Aminopropyltriethoxysilane was deposited on the surface of the steel

prior to the LbL coating using vapor phase deposition, which took place under vacuum. The substrate and 0.5 mL of APTES were placed in a vacuum desiccator overnight. LbL coating was done the following day after the sample was removed from vacuum. The crosslinking chemistry and silanization procedure are shown in **Figure 3.1**.

3.2.4 Characterization

Corrosion testing was carried out by using a typical three electrode set up including the sample as the working electrode (with an exposed area of 1.766 cm^2), calomel saturated electrode as the reference and platinum mesh as the counter electrode. The experimental interfacial characterization included electrochemical impedance spectroscopy (EIS) (Gamry, Warminster, PA). During testing, films were exposed to 3.5 wt% NaCl solution. Samples without an epoxy topcoat were tested for 24 hours and compared to uncoated steel samples tested under the same conditions. Samples tested with an epoxy topcoat were examined over a 5-day period, with measurements taken every hour for the first 24 hours and then once a day for each subsequent day. Multilayer films were compared to an epoxy coated sample prepared without any pre-treatments or LbL primer. Films were grown on polished silicon wafers (University Wafer, Boston, MA) for thickness and swelling measurements. A 5-minute plasma cleaning treatment, using a PDC-32G plasma cleaner (Harrick Plasma, Ithaca, NY), was performed on silicon wafers prior to deposition. An Alpha-SE ellipsometer (J.A. Woollman Co., Inc., Lincoln, NE) was used to measure film swelling and a P-6 Stylus profilometer (KLA-Tencor, Milpitas, CA) was used to measure film thickness after intermittent crosslinking. For swelling measurements, the films were exposed to DI water for 15 minutes and thickness measurements taken prior to and after exposure. Adhesion testing was done using a crosshatch adhesion test, following ASTM D3359.

3.3 Results and Discussion

3.3.1 Improved Corrosion Barrier Through Crosslinking

Nanobrick wall multilayer thin films are well known for their tremendous gas barrier behavior.[106,152] The diffusion of molecules through the film is hindered by the high tortuosity created by the clay platelets. To further improve the film's resistance to diffusion, glutaraldehyde crosslinking of the amine groups in PEI is used to generate a polymeric network that reduces water uptake in the PEI/VMT film and availability of amine groups to stem chloride ion diffusion through the film. Unfortunately, the clay filler in the polymer composite film hinders effective crosslinking through the bulk of the film.[153,154] To create a cohesive polymer network, optimal crosslinking conditions for the polymer-clay thin film are evaluated here using swelling measurements, where films with a greater extent of crosslinking display less swelling. **Figure 3.2** shows the influence of immersion time, GA solution concentration, and film thickness (i.e. number of BL deposited) have on crosslinking. The extent of swelling is reduced in films crosslinked with higher GA concentration, extended exposure time, and lower thickness. These parameters likely allow more GA to diffuse into the nanobrick wall structure. Once 5% GA is reached, there does not appear to be greater crosslinking with greater concentration. These parameters likely allow more GA to diffuse into the nanobrick wall structure, creating a more dense polymer network. The denser network improves the moisture resistivity of the film, reducing overall swelling and susceptibility to aggressive ion transfer through the film.
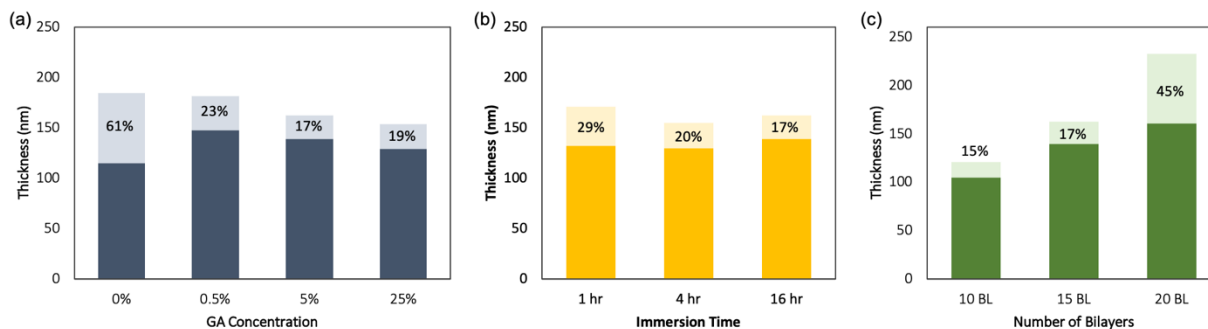
Figure 3.2. Swelling measurements for PEI/VMT multilayer films crosslinked at varying (a) GA concentration with crosslinking overnight on 15 BL, (b) crosslinking immersion time with 5% GA concentration on 15 BL, and (c) bilayers deposited before crosslinking with 5% GA overnight. The darker part of the bar is film thickness prior to testing and the lighter color is the thickness following exposure to water for 15 minutes.

Electrochemical impedance spectroscopy (EIS) testing was done on a reduced set of variables to demonstrate how crosslinking the polymeric mortar in the nanobrick wall film creates an improved corrosion barrier. To examine the influence of film thickness, deposition was done at two 15 BL intervals, with subsequent crosslinking after each, and compared with a 30 BL film crosslinked after only the final bilayer. Improved corrosion barrier can be seen in the increase of impedance values at low frequency, $|Z|_{0.1Hz}$. Values for each test are provided in **Table 3.1**. The films crosslinked at a greater GA concentration, and at both 15 and 30 BL, exhibit a higher $|Z|_{0.1Hz}$ value. These results further suggest that films exposed to GA at fewer BL (i.e. decreased thickness) have a greater extent of crosslinking and correspondingly improved corrosion resistance.

Table 3.1. Impedance values for crosslinked films.

GA Concentration (wt%)	Crosslinked at 30 BL Resistivity $|Z|_{0.01Hz}$ ($\Omega*cm2$)	Crosslinked at 15 and 30 BL Resistivity $|Z|_{0.01Hz}$ ($\Omega*cm2$)
0%	2,925	-
0.5%	7,407	9,327
5%	9,197	19,006
25%	6,166	14,032

Following this established intermittent crosslinking procedure, a reduced set of GA concentrations were evaluated to determine the best concentration for promoting corrosion resistance. For this analysis, films were crosslinked with 2, 5 and 10 wt% GA. **Figure 3.3** shows the Nyquist and Bode plots for these tests. Each of the crosslinked films provides some level of corrosion protection, outperforming the uncrosslinked 30 BL film. The film crosslinked with 5 wt% GA has the best corrosion resistance. Crosslinking with 2 wt% GA likely does not achieve the same level of networking, allowing for increased diffusion of corrosive species through the film. This can be seen in both the reduced $|Z|_{0.01Hz}$ value, compared to either the 5 wt% or 10 wt% crosslinked films, and a reduced magnitude observed in the Nyquist plot. Conversely, the exposure of the film to a greater concentration of GA (i.e. 10% or more) possibly results in plasticizing of the film due to excess unreacted small molecules present. It is also possible that the corrosive nature of GA, particularly at high concentration, initiates corrosion prior to testing, expediting failure of the film.
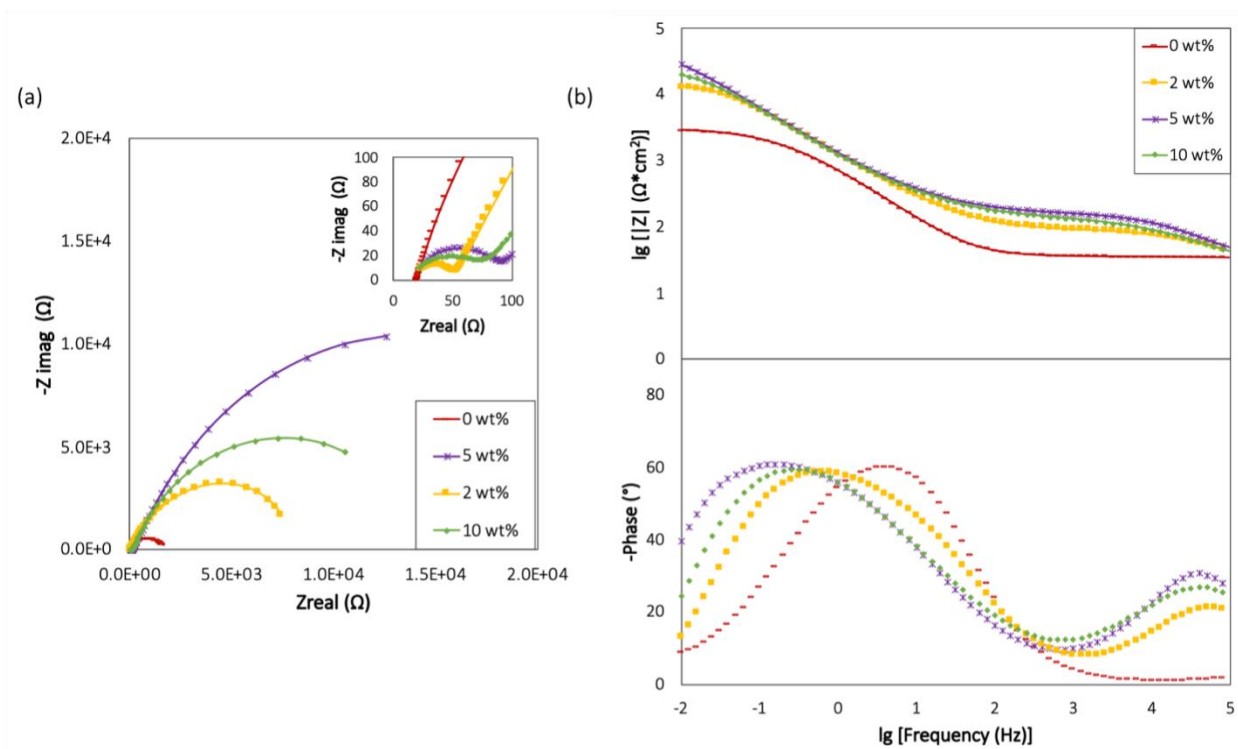
Figure 3.3. EIS (a) Nyquist and (b) Bode plots for 24 hours of testing 30 BL PEI/VMT, crosslinked with various GA concentrations: 0 (red), 2 (yellow), 5 (purple), and 10% (green).

3.3.2 Silanization for Adhesion

Corrosion resistance garnered by crosslinked nanobrick wall thin films is further improved with silane functionalization of the steel surface prior to film deposition. While the independent corrosion resistance achieved by a pretreatment coating is important, the primary role of this layer is to improve the adhesion between a topcoat and the underlying metal. Bonding of cationic PEI to steel is promoted by first exposing the metal to a 1M sodium hydroxide and 100mM sodium nitrate solution to generate a hydroxide layer on the surface. As a result, the polymeric layer hydrogen bonds with the generated inorganic hydroxylated surface. While sufficient for promoting adhesion between PEI and steel during the deposition process, this pre-treatment offers little adhesion once the film is dry. By introducing aminopropyltriethoxysilane, an organic surface is created that promotes improved hydrogen

bonding. Vapor phase deposition of the APTES onto the surface of the metal allows for less variability in the formation of the Si-O-Si bonds between the silane and the metal.[155,156]

When PEI is deposited onto the APTES-treated steel, the PEI strongly bonds with the amine groups in the APTES chains through hydrogen bonding between the two organic layers. This superior adhesion is confirmed through the use of a crosshatch adhesion test, following ASTM standard D3359, shown in **Figure 3.4(a)**. The film deposited on the steel without APTES has no apparent adhesion, with full delamination from the surface, while the film deposited following silanization exhibits improved adhesion. EIS testing demonstrates the extent to which this improved adhesion influences the corrosion resistance. Independently, the APTES offers no corrosion resistance, likely hydrolyzing and delaminating from the steel quickly upon exposure to the testing solution. Conversely, the benefits of the silanization between the film and substrate can be seen in the larger magnitude displayed in the Nyquist curve (**Fig. 3.4(b)**). Further, the impedance value, $|Z|_{0.01Hz}$, reported in **Table 3.2**, is greater and is indicative of improved corrosion barrier. As APTES adds no thickness to the overall system, the improved corrosion resistance can be attributed to the adhesion generated through better bonding.
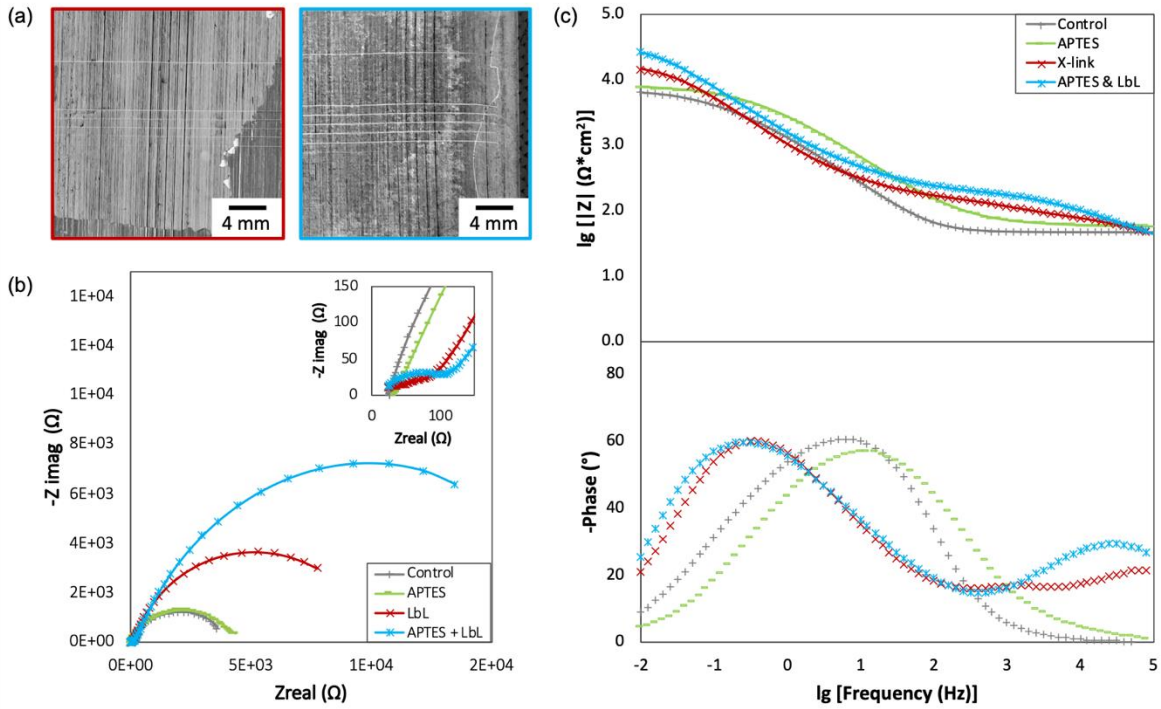
Figure 3.4. (a) Digital images of adhesion testing with (left) and without (right) APTES pretreatment, where the darker grey is the remaining coating following the test. (b) Nyquist plot after 24 hours of EIS testing and (c) corresponding Bode impedance (top) and phase (bottom) plots.

Table 3.2. Thickness and impedance values due to APTES treatment.

Sample	Thickness (nm)	Impedance $|Z|_{0.01Hz}$ ($\Omega{*}cm^2$)
Control Steel	-	6,438
APTES	1.3 ± 0.1	7,729
Nanobrick Wall	314.6 ± 9.7	19,006
APTES + Nanobrick Wall	315.0 ± 14.9	26,152

3.3.3 Multilayer Insulating System

The most successful corrosion resistant barrier coatings make use of multiple layers in tandem to protect a metal substrate. To demonstrate the viability of the silanized and crosslinked nanobrick wall thin film for use as a primer layer in a multilayer system, an epoxy topcoat was applied and tested over 5 days. This is a corrosion-resistant bisphenol-A based epoxy coating

31

[157,158]. A control of the epoxy coating alone is compared to epoxy paired with APTES, and a 30 BL PEI/VMT film, crosslinked at 15 and 30 BL with 5% GA, with and without silanization. Evaluation of the Bode plots show the contrast between the epoxy control and the system with the crosslinked and silanized nanobrick wall primer. While the neat epoxy system, shown in **Figure 3.5(a)**, starts with the greatest $|Z|_{0.01Hz}$ value, the apparent corrosion resistance deteriorates over 5 days. Independently, the silanization and the crosslinking of the PEI/VMT film (**Fig. 3.5(b) and (c)**) do not perform well. The silanized epoxy starts out lower than the neat epoxy sample and deteriorates from there, demonstrating that APTES is not a good interface between the steel and epoxy topcoat. The nanobrick wall film also starts out poorly, but its reduction in performance over 5 days is less and seems stable after the first dip in performance. Only the crosslinked and silanized nanobrick wall film (**Fig. 5(d)**) exhibits sustained corrosion resistance over the 5-day testing period.
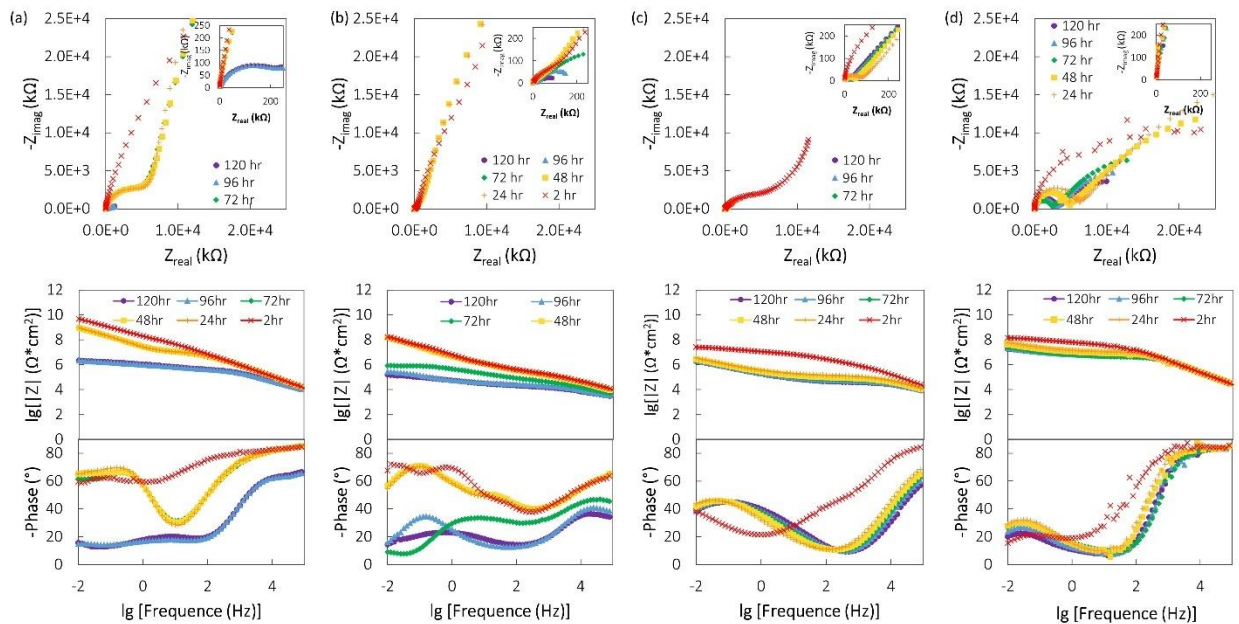
Figure 3.5. EIS Nyquist (top) and Bode (bottom) plots comparing films with an epoxy topcoat and pretreatment layer of (a) hydroxylated steel alone, (b) APTES treated steel, (c) a 30 BL crosslinked (with 5% GA) PEI/VMT coating, and (d) the same nanobrick wall primer on APTES-treated steel.

Fitting these multilayer films to an equivalent circuit model provides insight into the overall interfacial characterization, including the corrosion resistance of each system. **Figure 3.6(a) and (b)** shows film resistivity and charge transfer resistance over the 5 days of testing, respectively. The resistance of the coating is indicative of the overall barrier performance. The system performance is also evaluated with the charge transfer resistance. Charge transfer occurs at the interface between the coating and the substrate as electrons enter the metal and metal ions diffuse out. Initially, APTES alone outperforms the LbL deposited coating, likely due to poor adhesion between PEI and the steel. The trend observed, particularly in the charge transfer resistance, is similar when comparing the APTES and control coating, indicative of the performance of the epoxy coating without the additional polymer nanocomposite primer. The APTES sample does not perform as well, which is possibly a result of poor interfacial bonding between the silane and the epoxy. Additionally, an improvement in film resistance is temporarily observed in the APTES sample. As the water infiltrates the epoxy, but prior to the dissolution of the APTES layer, APTES may hydrolyze, briefly imparting greater interaction with the epoxy and increasing the overall resistance of the system. APTES alone does not show a robust corrosion barrier, so the overall barrier performance begins to degrade, ultimately having the least film and charge transfer resistivity of the tested samples. Most importantly, the fitting data confirms that the only film that performed well over all 5 days of testing was the combination of APTES, and crosslinked nanobrick wall film, with the epoxy topcoat (APTES + LbL). At the beginning of the test, the sample's film resistivity is equivalent to the independent epoxy system. As the test solution diffuses through the epoxy, and the neat epoxy film resistivity drops, the film resistivity of the sample paired with the silanized and crosslinked nanobrick wall film remains stable. Additionally, the prolonged resistance displayed by the silanized and crosslinked nanobrick wall film

pretreatment to the charge transfer is accounted for by the improved adhesion between the PEI/VMT coating and the steel through APTES silanization.
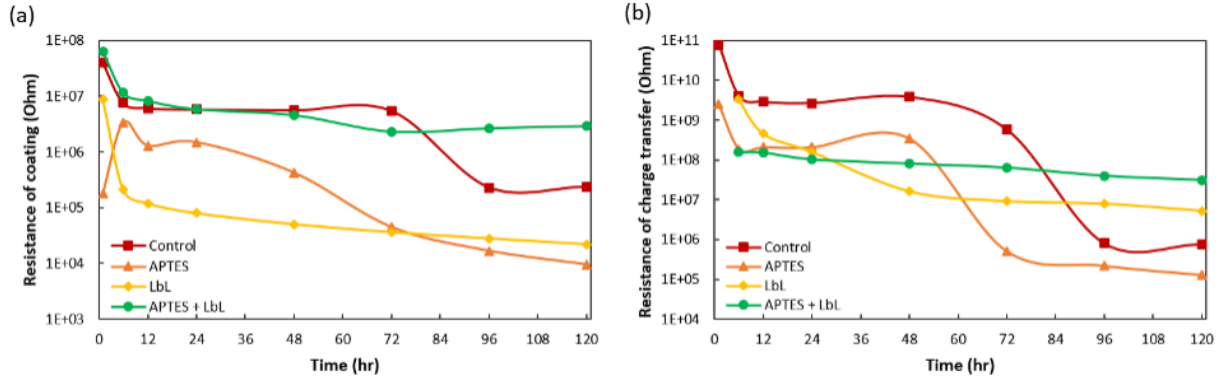
Figure 3.6. Equivalent circuit modeling of (a) resistivity and (b) charge transfer resistance of various systems with an epoxy topcoat: control (red), APTES alone (orange), 30 BL PEI/VMT crosslinked (yellow), and the combination of APTES and the same crosslinked PEI/VMT (green).

3.4 Conclusions

The use of a layer-by-layer deposited nanobrick wall primer provides good corrosion protection to a steel substrate. Once silanized and crosslinked, the potential for these PEI/VMT coatings increases greatly, offering not only improved corrosion protection but also improved adhesion to the steel. These properties make them a good option as an alternative pre-treatment layer for multilayer insulating coatings. The network generated by the crosslinked PEI promotes moisture resistance and a reduced vulnerability to aggressive ions permeating the coating. The APTES promotes improved adhesion that hinders delamination and reduces the available surface for corrosion induction. Combining the two methodologies with the nanobrick wall structure, which already hinders molecular diffusion through the tortuous path created by clay nanoplatelets, provides environmentally-benign corrosion protection.

CHAPTER IV – EFFICIENT HEAT SHIELDING OF STEEL WITH MULTILAYER

NANOCOMPOSITE THIN FILM*

4.1 Introduction

In the present study, tris(hydroxymethyl)aminomethane (THAM) was added to a cationic

polyethylenimine (PEI) solution and alternately deposited on steel with vermiculite (VMT) clay,

because of its low thermal conductivity ($0.04 − 0.012$ W·m^{-1}·C^{-1}), high aspect ratio, and low

thermal emissivity,[159] to generate a nanobrick wall thin film that provides one-time thermal

protection to the steel. These so- called thick growing PEI-VMT coatings have demonstrated

improved flame-retardant properties with fewer deposition steps than their thinner counterparts

grown without salt additive.[130,136] The addition of THAM to the PEI results in a thicker growing

film and charge screening in the polyelectrolyte chain and causes a form of clay complexation that

results in more stacking in each layer.[82,160] As akylamines interact with the surface of the clay

platelets, there is intercalation of polymer that results in stacks being deposited in a single

deposition step.[134] By comparison, a system grown without the amine salt is approximately 2

orders of magnitude thinner than the present system.[130] The blowing behavior (i.e., gas generation)

exhibited by PEI and the amine salt, when exposed to a high temperature, creates clay-reinforced

bubbling that contributes to the thermal protection of the underlying metal. The use of this

nanobrick wall architecture, in combination with the thermal properties of the individual

components, provides a unique and relatively thin thermal barrier coating that may be used to

protect a variety of metals that may be exposed to catastrophic high-temperature events.

_____

4.2 Experimental

4.2.1 Materials and Substrates

Branched polyethylenimine (PEI) (Mw = 25 000 g/mol) and tris(hydroxymethyl)aminomethane (THAM, crystalline) were purchased from Sigma-Aldrich (Milwaukee, WI). Microlite 963++ vermiculite clay (VMT, 7.8 wt % in water) was purchased from Specialty Vermiculite Corp (Cambridge, MA) and diluted to a 1 wt % suspension. Deionized (DI) water, with a resistivity greater than 18 MΩ, was used to prepare all solutions and rinses. The pH of the cationic solution and rinse was adjusted to 6, while the pH of the anionic solution and rinse was adjusted to 10, using 5 M HCl and NaOH, respectively. A 50 mM THAM solution was prepared prior to adding the cationic species. Films were grown using 0.1, 0.5, 1, or 5 wt % solutions of PEI (with THAM). Ground A36 low-carbon steel was purchased from McMaster-Carr (Aurora, OH) in 10.16 cm $\times$ 10.16 cm $\times$ 0.32 cm plates. Steel substrates were cleaned with a DI water, methanol, and again DI water rinse prior to bath sonicating in DI water and then isopropanol (IPA) for 2 min each, with IPA rinses between, and dried with filtered air. The steel was then immersed in a 1 M sodium hydroxide and 100 mM sodium nitrite solution overnight to passivate the surface to improve coating adhesion.

4.2.2 Thin-Film Preparation

Substrates were coated with PEI- VMT multilayers using layer-by-layer assembly, which was carried out with a home-built robotic system.[151] Films are assembled by first immersing the substrate into the polycationic solution for 5 min, followed by immersion in a rinse solution of 50 mM THAM for 1 min. The substrate is then immersed in the clay solution and a rinse of DI water for 5 and 1 min each, which completes one bilayer (BL). Subsequent bilayers use 1 min dips in each solution. After all the layers are deposited, the films are dried in ambient conditions

overnight and then stored in a desiccant box prior to testing. Films were prepared with 6, 10, and 14 BL, following a previously outlined procedure,[130] at varying concentrations of PEI solution. A schematic of the deposition procedure, and resulting nanobrick wall structure, can be found in **Figure 4.1**.
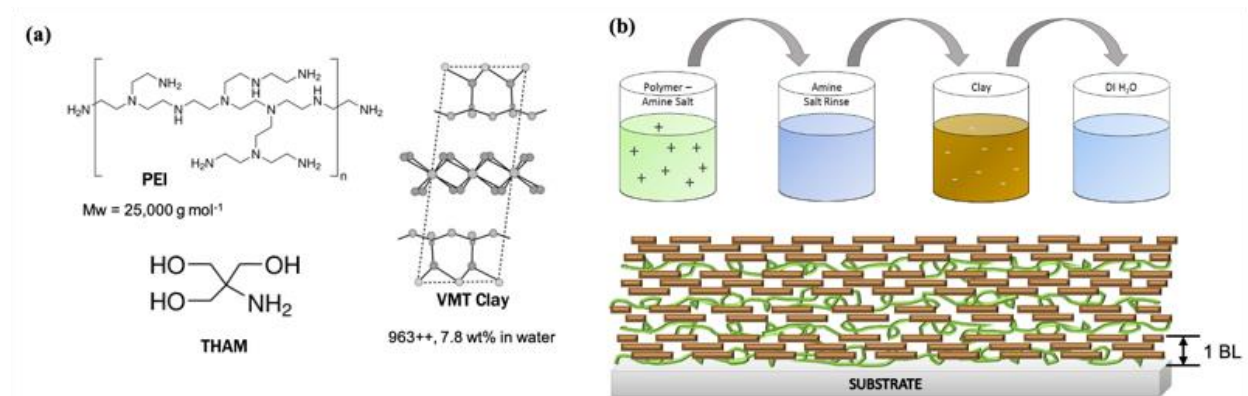
Figure 4.1. (a) Chemical structures of polyethylenimine (PEI), tris(hydroxymethyl)aminomethane (THAM), and vermiculite (VMT) clay. (b) Schematic of layer-by-layer deposition of the PEI-THAM/VMT nanobrick wall coating.

4.2.3 Nanocomposite Film Characterization

Flame tests were carried out with a butane hand torch (Triggertorch MT-76 K; Master Appliance Corp.; Racine, WI). Samples were placed in a holder, with a $15.24 \text{ cm} \times 20.32 \text{ cm}$ front plate, to orient the plate perpendicular to the torch. Films were subjected to the flame for 20 min. The temperature was measured using two K-type thermocouples (McMaster-Carr; Aurora, OH). One thermocouple (TC1) was placed on the center of the back side (i.e., the uncoated side) of the plate, centered along the axis of the butane torch. Another thermocouple (TC2) was placed on the back side as well, offset 2.54 cm above TC1 (**Figure 4.2**). For decreased thermal resistance, silver paint (Electron Microscopy Science; Hatfield, PA) was used to adhere the thermocouple to the steel plate. Samples were compared to an uncoated steel plate tested under the same conditions. A DektakXT surface profilometer (Bruker; Tucson, AZ) was used to measure film thickness and

roughness on polished silicon wafers (University Wafer; Boston, MA). A 5 min plasma cleaning treatment, using a PDC-32G plasma cleaner (Harrick Plasma; Ithaca, NY), was performed on silicon wafers prior to deposition. The clay composition of freestanding films was measured with a Q50 Thermogravimetric Analyzer (TA Instruments; New Castle, DE). Films weighing approximately 7−9 mg were tested in an air atmosphere. First the films were held at 100 °C for 20 min to remove water, and then the temperature was increased at a heating rate of 10 °C·min^{-1}. The surface morphologies of the films prior to and after burning were observed by sputter coating the samples with 5 nm of platinum/ palladium prior to imaging using a a field-emission scanning electron microscopy (SEM) instrument (model JSM-7500, JEOL; Tokyo, Japan). Fourier transform infrared (FTIR) spectroscopy results of the burned and unburned film were collected in the range of 4000−700 cm^{-1} (16 scans and 4 cm^{-1} resolution) at room temperature using an FTIR/FIR spectrophotometer (PerkinElmer Frontier, Waltham, MA) equipped with a diamond crystal. Emissivity measurements were done using a separate spectrometer, a Thermo Nicolet 380 FTIR (ThermoFisher, Waltham, MA) with an attenuated total reflectance (ATR) accessory.
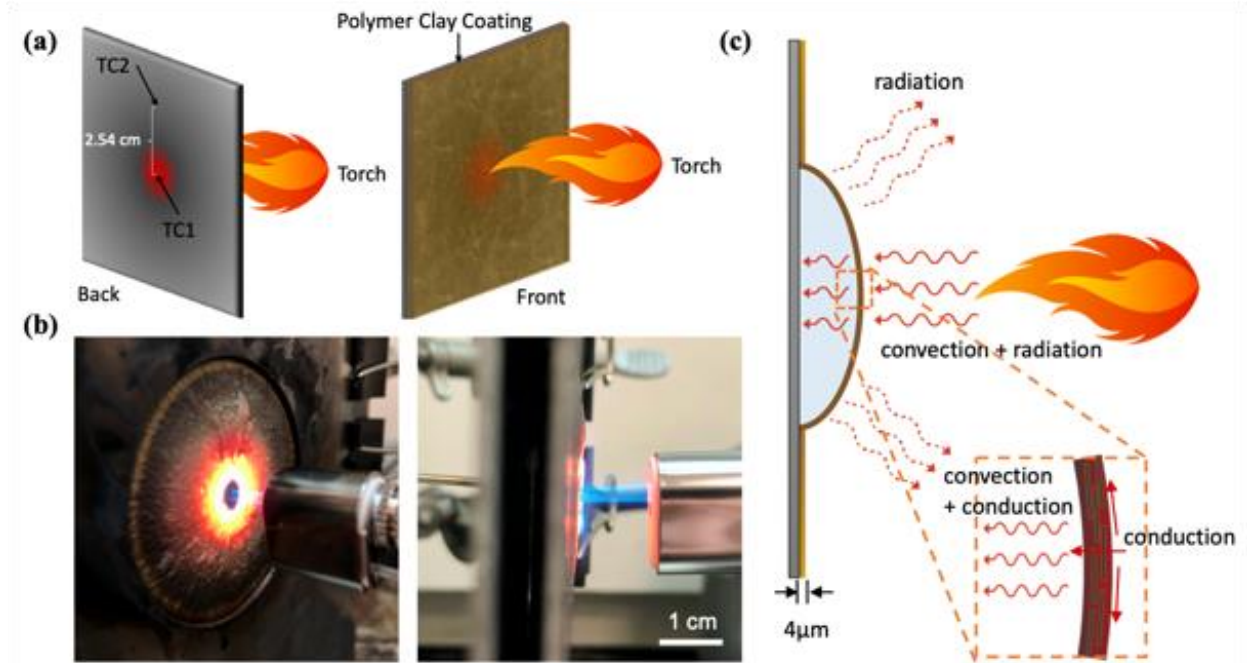
Figure 4.2. (a) Schematic of the flame test setup, with location of center (TC1) and edge (TC2) thermocouples shown. (b) Digital images of flame testing, showing formation of a macroscale bubble [view from an angle (left) and side view (right)]. (c) Schematic of observed bubbling behavior and heat-transfer mechanisms.

4.2.4 Thermal Modeling

A 3D finite element model was created within ANSYS FLUENT to extract the net thermal resistance (Rnet) of the multilayer films exposed to the butane torch flame. A square plate (15.24 cm length sides and 0.3175 cm thickness) was defined, composed of A36 low carbon steel (density of 7.8 g·cm−3, heat capacity of 0.48 J·g−1·C−1, and thermal conductivity of 50 W·m−1· C−1). The element size of the model was no greater than 0.4 mm spacing at the boundaries. Fixed time steps of 0.5 s were used on all models. Heat transfer was modeled at the heated side using a forced convection boundary condition with a Gaussian heat-transfer coefficient and temperature distribution, resulting in a Gaussian heat flux distribution to approximate previous studies in butane torch interaction with metal surfaces.[161–163] The maximum free stream temperature (FST) of the heated side was 1432.85 °C (i.e., the approximate maximum temperature of a butane torch).

The back side used a free convection model with constant environmental temperature (27.85 °C). The side walls of the plate were treated as adiabatic boundaries, and the system was initialized at 27.85 °C. The heat-transfer coefficient on the back side (33) $W \cdot m^2 \cdot C^{-1}$), the maximum heat-transfer coefficient (120 $W \cdot m \cdot C$), and the width of the Gaussian distribution (σ is 1.5 cm) were defined to minimize the residuals between simulated and experimental data in the transient temperature data of the heated bare steel plate (**Figure 4.3**).
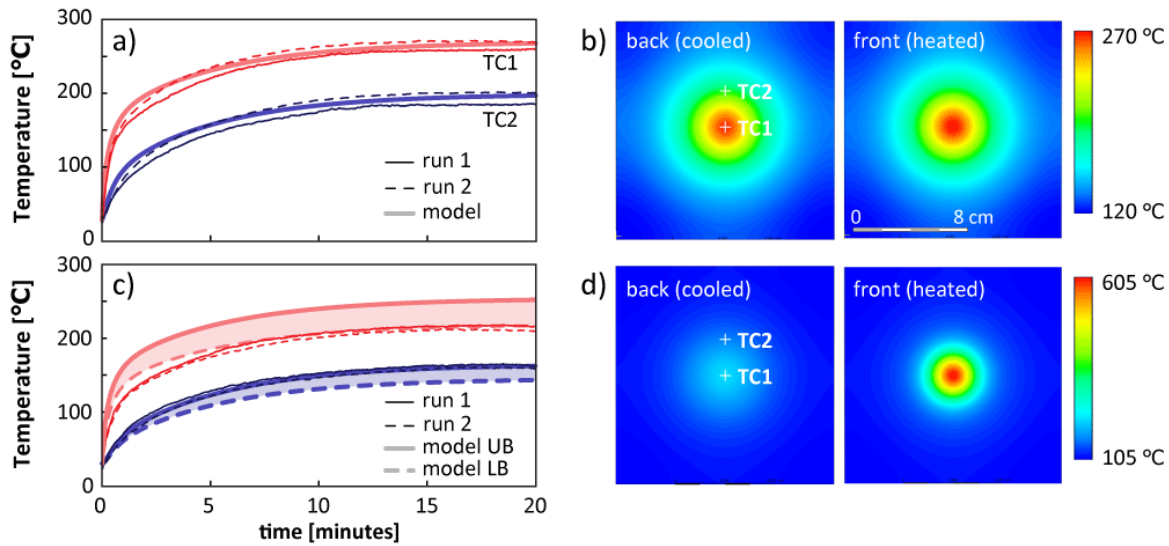
Figure 4.3. Measured and simulated temperature on the back (uncoated) side of the steel plate, as shown in **Figure 4.2** for a) baseline steel plate with no polymer-clay multilayer film, and c) 0.1% PEI-THAM/VMT 6 BL film, as an example. Red lines are the temperature measured in the center of the hot spot, blue lines are offset to the edge of the hot zone by 2.54 cm. In c), multiple simulations are run to best align with the temperatures measured at TC1 and TC2, in the center and on the edge of the hotspot, respectively, resulting in the upper and lower bounds of net thermal resistance shown in **Figure 4.8**. b) and d) illustrate the resulting temperature distribution on the front and back side of the simulated plate at a time of 20 min for the baseline and the 0.1% PEI-THAM/VMT 6 BL film, respectively.

These boundary conditions were held constant, and a finite thickness film was introduced with uniform thermal resistance. Heat transfer is modeled across the metal/film interface using the coupled thermal condition in the metal/film boundary without additional contact resistance. The net thermal resistance of this film was determined by minimizing the difference between simulated and experimental observations at TC1 and TC2 and the model. This approach neglects any

contributions to increasing thermal resistance introduced by changes in the heat-transfer coefficient or absorptivity of the coating, assuming that the effective thermal conductivity of the multilayer film provides the dominant resistance to heat transfer in the system. Furthermore, this approach also neglects radial variability in the thermal resistivity of the TBC layer of the film that may result from the different maximum temperature achieved at different locations in the film.

4.2.4 Emissivity Measurements

In thermal radiation, the sum of transmissivity (τ), reflectivity (ρ), and absorptivity (α), is always equal to 1. Kirchhoff's law notes that the absorptivity and emissivity (ε) are equivalent at equilibrium. By measuring the reflectance using Fourier transform infrared spectroscopy (FTIR), with an attenuated total reflectance (ATR) accessory, there is no transmission, therefore:

$$\rho(\lambda) + \varepsilon(\lambda) = 1 \tag{1}$$

where both ρ and ε are functions of wavelength, and ρ is measured by FTIR (Thermo Scientific, Nicolet 380). The spectral emissive power per unit area (emissive flux) for a blackbody ($B(\lambda, T)$) is a function of the wavelength (λ) and the blackbody temperature (T). The relationship is given by Planck's law:

$$B(\lambda, T) = \frac{2hc^2}{\lambda^5} \frac{1}{e^{\frac{hc}{\lambda k_B T}} - 1} \tag{2}$$

where k_B is the Boltzmann constant, h is the Planck constant, and c is the speed of light in vacuum. The spectrally averaged emissivity (ε) of a surface at a given temperature T can be determined from equation 3 below by integrating the measured emissivity as a function of wavelength (λ) and weighting it with the spectral emissive flux for a black body at that temperature (T):

$$\varepsilon = \frac{\int B(\lambda, T) \times \varepsilon(\lambda) d\lambda}{\int B(\lambda, T)} \tag{3}$$

Measurements were done at room temperature, and a weighting blackbody temperature of 700 °C was used as an approximation of the temperature of the surface exposed to the flame. The emissivity values reported are the weighted and spectrally-averaged emissivity over a range of wavelengths (2.5 to 25 µm).

4.3 Results and Discussion

4.3.1 Polymer-Clay Nanocomposite Composition and Growth

For layer-by-layer film growth, the PEI-THAM solution and rinse were adjusted to pH 6, while the VMT suspension and DI water rinse were adjusted to pH 10. In addition to creating high ionic strength solutions, this allows for the necessary acid to be present in the system to aid in char formation that occurs during intumescence, which has been demonstrated to be an effective flame retardant.[12] In order to have a complete intumescent system, a blowing agent and carbon source are needed to act in the condensed phase to form the char layer. Other studies have established that in addition to acting as a thickening agent and "mortar" for the nanobrick wall, THAM and cationic PEI are also blowing agents that release nitrogen, water and carbon dioxide as they decompose.[76,164] As the film intumesces, the char encases the nanoclay platelets and a ceramic shell forms, insulating the underlying metallic substrate from the high temperatures.

To demonstrate the role of the charring and blowing actions, and the extent to which the clay and cationic polymer contribute to the heat shielding properties, the thermal insulating property of films grown on steel with varying number of bilayers (and PEI solution concentration) is evaluated. Varying the number of bilayers deposited (i.e., thickness) influences the heat-shielding behavior of these films. **Figure 4.4a** shows film thickness with varying concentration of PEI and bilayers deposited. The film growth is linear, indicative of a static composition being

42

deposited with each bilayer. Changing the concentration of PEI in the films, by altering deposition solution concentration, leads to much thicker growth, with 5% PEI producing five times the thickness as a coating grown with only 0.1% PEI. This is expected, as film growth kinetics are influenced by the polyelectrolyte solution concentration, where increasing concentration leads to increased adsorption.[165,166] Solutions with a greater concentration of polymer experience greater polyelectrolyte mass transport from the solution to the multilayer. Thermogravimetric analysis (TGA), shown in **Figure 4.4b**, indicates that there is significantly more PEI being deposited when the deposition solution has a greater concentration.
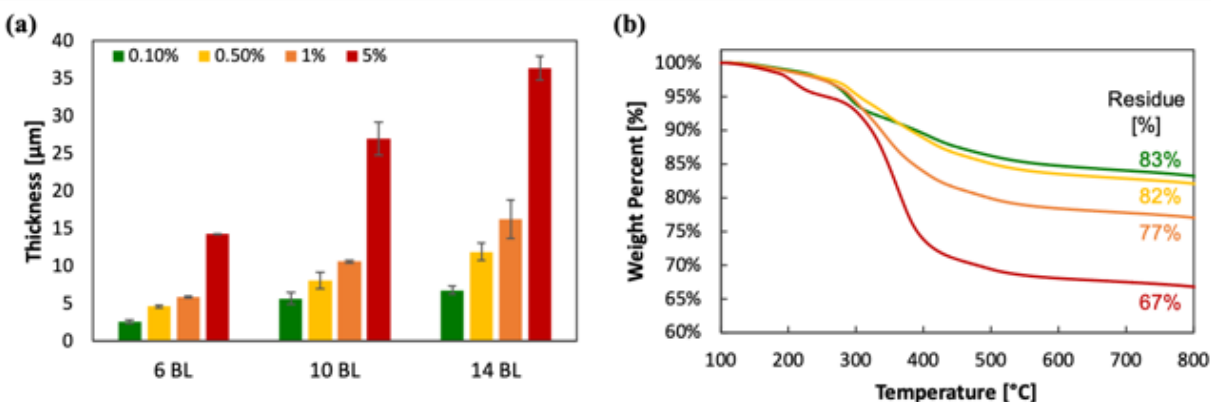
Figure 4.4. (a) Layer-by-layer growth of films with varying PEI concentration in deposition solution (deposited on silicon wafer). (b) Thermogravimetric analysis for 14 BL films with varying PEI concentration: 5% PEI (red), 1% PEI (orange), 0.5% PEI (yellow), and 0.1% PEI (green).

4.3.2 Heat Shielding of Nanobrick Walls

PEI-THAM/ VMT films were grown on one side of a 0.32 cm thick A36 carbon steel plate. Heat shielding experiments were carried out with a small butane torch, with a maximum flame temperature of approximately 1430 °C, oriented perpendicular to the coated side of the steel plate at a distance of approximately 1 cm. The coating was exposed to the flame for 20 min. Two thermocouples (TC) were attached to the back side of the plate, one centered along the axis of the butane torch flame and a second offset by a distance of 2.54 cm. A front plate was used to mount

43

the test piece, with a 5.08 cm diameter aperture centered on the axis of the torch flame. A schematic of the test setup is depicted in **Figure 4.2a**. Upon exposure to the flame, macroscopic bubbling was observed in the film, as shown in **Figure 4.2b**. This bubbling likely results from gases released from the blowing of THAM and PEI that are trapped between the film and substrate, causing the film to expand to form a clay- reinforced bubble. **Figure 4.2c** shows a schematic of the thermal resistance mechanisms that contribute to preventing heat transfer across the film. By evaluating these properties and how different film deposition parameters affect them, conclusions can be drawn about the mechanisms behind their observed thermal resistance.

Upon comparing the heat shielding behavior of the films prepared with varying concentration of PEI it is evident that increasing the concentration results in an improved thermal barrier. Exposing an uncoated steel plate to the flame of a butane torch for 20 min results in the temperature on the backside of the plate to be approximately 260 °C. The temperature measured when the steel is coated with 14 BL of 0.1% PEI-THAM/VMT is about 190 °C. When the 14 BL 5% PEI-THAM/VMT coated steel undergoes the same test, the temperature on the uncoated side of the steel is 137 °C after 20 min (i.e., a 53 °C further increase in the temperature differential, ΔT $= TC1_{(uncoated)} - TC1_{(coated)}$, with the same number of deposition steps). The resulting ceramic bubble and observed temperature for each 14 BL coating, and the uncoated control, over the 20 min of testing can be seen in panels a and b of **Figure 4.5**, respectively. The larger temperature differential with increasing PEI concentration is likely due to a combination of the increase in polymer for blowing and charring and the increased thickness. When the bubble forms, the ceramic shell is thicker and more stable, with minimal surface cracking observed. This clay-based shell has the same nanobrick wall structure as the unheated film, with the char acting as the mortar, hindering the release of the blowing gases from the bubble. In addition to the more stable

44

macroscale bubble, nanoscale bubbling also results as the film intumesces, which can be seen with scanning electron microscopy (SEM), as shown in **Figure 4.5c**. This multiscale porosity also contributes to suppressing heat transfer across the film.
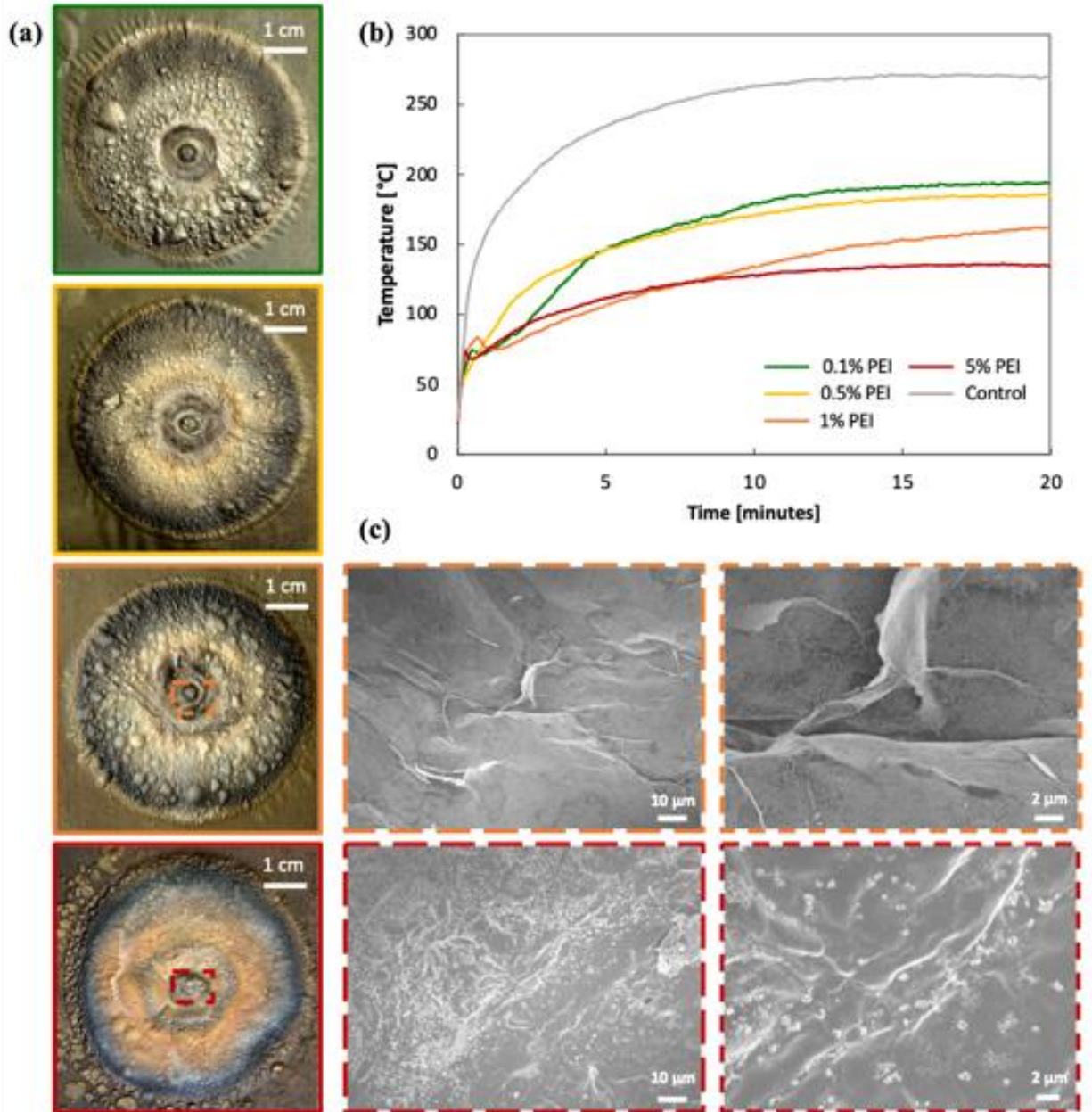
Figure 4.5. (a) Digital images after burn of 14 BL PEI-THAM/VMT films prepared with PEI concentrations of 0.1% (green), 0.5% (yellow), 1% (orange), and 5% (red). (b) Temperature of coated and uncoated steel as a function of exposure time to the butane torch flame. (c) SEM images of 1% (orange) and 5% (red) PEI films showing nanoporosity after burning [at lower (left) and higher (right) magnification].

At a PEI deposition solution concentration of 0.1%, the role of bilayers is apparent, as films that have less deposition steps do not form the same cohesive macroscale bubble upon exposure to the flame relative to films with a greater number of layers (**Figure 4.6a**). The inconsistent bubbling that results with fewer bilayers exhibits lower thermal resistance [i.e., smaller temperature differential (ΔT) in **Figure 4.6c**]. This result highlights the roles of the film thickness and the gas bubbles in thermal shielding. A film with more bilayers impedes heat transfer across a greater thickness. Additionally, the bubbles that contain the gases released during pyrolysis further increase the effective thermal resistivity of the film and suppress heat transfer between the now delaminated film and the underlying substrate. The same analysis was done, comparing heat shielding at varying BL, on films grown with 5% PEI in the deposition solution. The trend of increasing bilayers resulting in increased heat shielding is also observed with the greater PEI concentration, supporting the hypothesis that films with more adsorbed polymer perform better. Furthermore, for films grown with more polymer, bubble growth is more consistent across bilayers and the observed temperature differential is larger.
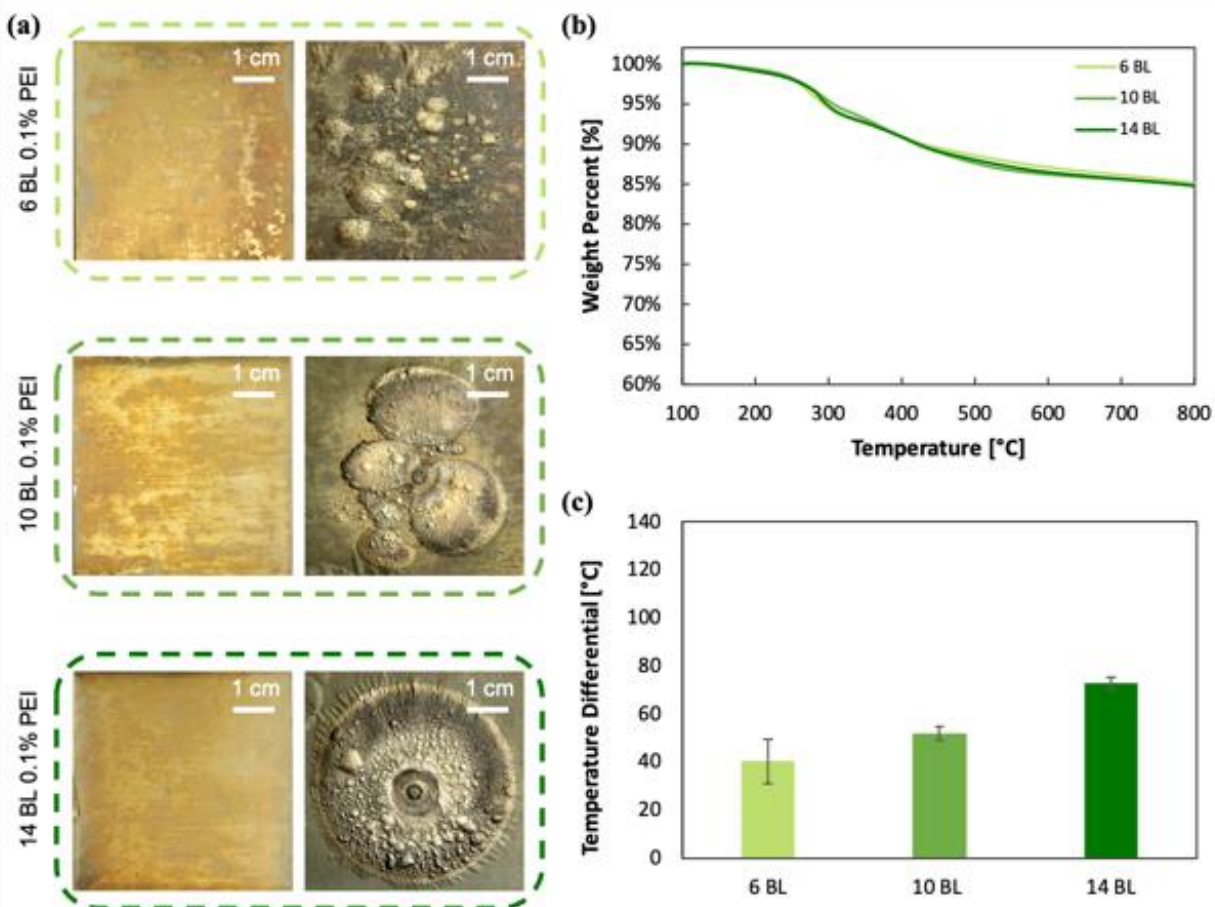
Figure 4.6. Heat shielding of 6, 10, and 14 BL 0.1% PEI films: (a) digital images of films preburn (left) and post burn (right), (b) thermogravimetric analysis, and (c) temperature differential between uncoated and coated steel ($\Delta T = TC1(\text{uncoated}) - TC1(\text{coated})$) after the system has achieved equilibrium.

Infrared spectra of the 5% PEI-THAM/VMT film prior to and after burning are shown in **Figure 4.7**. Prior to heating, peaks for the amines and hydroxides, found in both PEI and THAM, are apparent at 1600 and 3500 cm^{-1}, respectively. The peaks around 1000 cm^{-1} and below are the VMT. The peaks associated with the amines and hydroxides are not present when looking at an area directly exposed to the heat from the butane torch. This suggests that the PEI and THAM have both undergone pyrolysis, leaving VMT and char as the thermal barrier. By evaluating the film approximately a centimeter away from the central burn site, a reemergence of the PEI and THAM peaks can be seen. TGA reveals that both the PEI and THAM degrade around 300 °C, while VMT

remains stable (**Figure 4.6b**).[76,130,167] Peaks indicating the presence of these components a centimeter from the film region exposed to the flame indicates that the in-plane thermal conductivity is sufficiently low to result in a large radial temperature gradient within the film. While this IR analysis provides further insight into the composition of the film upon exposure to the flame, it provides no insight regarding the thermal resistivity of the film, which is addressed in section 4.3.3.
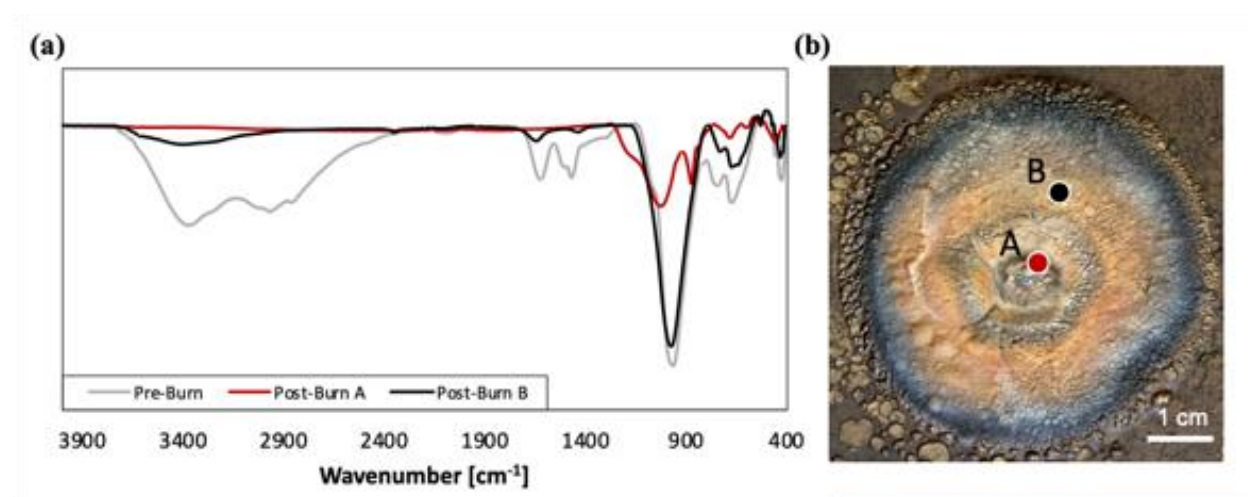
Figure 4.7. (a) FTIR analysis of a 14 BL 5% PEI-THAM/VMT film prior to flame testing and following flame testing in two locations: near the center of the bubble (A), where the flame was applied, and about 1 cm from the center (B). (b) Digital image of the film post burning that shows locations of FTIR analysis.

4.3.3 Mechanism of Thermal Shielding

When the nanocomposite coating is subjected to a temperature gradient, heat transfer results from vibrational conduction in the solid phase, conduction (or convection) through air in any voids, and radiation losses to the surroundings. The net thermal resistance of the film, including the effects of micro- and macroscopic porosity, is extracted from 3D transient models using a commercial finite element package, as shown in **Figure 4.8**. Importantly, this approach neglects any changes in the heat- transfer coefficient or absorptivity of the coating and also

48

neglects radial variability in the thermal resistivity of the film. As a result, this approach creates an approximate aggregate thermal resistance (R_{net}) associated with the intumesced polymer−clay multilayer film, assuming that this provides the dominant resistance to heat transfer in the system. R_{net} varies systematically with polymer−clay multilayer film structure, increasing somewhat with the number of bilayers, and increasing dramatically in the 5% PEI films, relative to the 0.1%−1% PEI films. This is consistent with the thickness measurements (**Figure 4.4a**), which indicate that the 5% PEI films have dramatically higher thickness when compared to similar films with 0.1%−1% PEI.
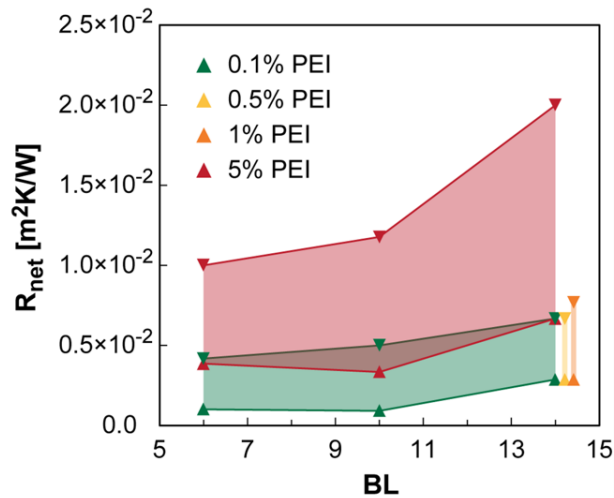
Figure 4.8. Net thermal resistance of polymer−clay multilayer films extracted from thermal model. Downward and upward triangles illustrate upper and lower bounds on thermal resistance. The 0.5% and 1% PEI-THAM/VMT films all have 14 BL but were separated for legibility.

The ceramic bubble structure was found to be an integral part of the heat shielding, as films that exhibited less bubbling were not as thermally insulating. This macro-scale bubble results as the polymer and amine salt in the nanocomposite film undergo pyrolysis and generate gas. It was found, during testing, that if a film made of the same number of bilayers and PEI concentration did not form a cohesive macroscale bubble, then the temperature differential decreased. Further, films that generate a thicker and more stable bubble, due to larger amounts of blowing material,

create more thermal resistance. The films made with 5% PEI are not only thicker than films made with less PEI but also contain more material that contributes to the macroscale bubble growth. Upon generation of a stable bubble, the energy from the temperature gradient must now travel through the low thermal conductivity film and pass through the gaseous medium in the bubble that further dissipates the energy, before it reaches the underlying metal substrate.

In addition to the presiding functionality of the macroscale bubble, the film's nanobrick wall morphology, in tandem with nanoscale pores and overall thickness, contribute to the observed thermal resistance. The number of bilayers deposited has a direct effect, creating additional resistance through more layers. While the increase in PEI concentration alters how much material is deposited with each bilayer, affecting the thickness and internal morphology, there is also a change in the extent of intumescence that occurs, where films made with a greater concentration of PEI generate more blowing and charring. Not surprisingly, the intumescence occurs heterogeneously across the exposed film, as the maximum temperature of the film decreases radially outward from the flame axis, and the local thermal resistance at the center and edges of the exposed films are likely different. This heterogeneity results in a poor simultaneous fit of the central and edge temperatures as measured on the back side of the plate. To account for this variation, approximate upper and lower bounds on R_{net} were extracted, using the best fits to the central and edge temperature measurements independently (**Fig. 4.2**).

Emissivity measurements were done on samples pre- and post-exposure to a flame, following a procedure outlined by Okada.[168] While these emissivity measurements were not performed during the flame testing, the measured emissivity is expected to be representative for the film exposed to higher temperatures. The emissivity is weighted to a blackbody at 700 °C, which is the approximate flame temperature once it reaches the plate. This measurement provides

insight into the influence of radiative transport for these nanocomposite thin films. Thermal emissivity of the films is given in **Figure 8**, revealing values comparable to those of highly polished metals.[169] Infrared emissivity has been shown to be reduced for some nanocomposites when compared to the individual components, which is likely due to the electrostatic interaction between the layers.[170,171] The relatively low thickness of these films may also affect emissivity, with thinner films often exhibiting reduced emissivity. These physical factors, combined with the expected low emissivity of VMT, generate a radiative shielding effect that contributes to the overall lower thermal resistance of the system. Additionally, for the 14 BL films, exposure to the flame (and subsequent charring and formation of bubbles) further reduces the emissivity. The low emissivity (or absorptivity) of the film reduces the radiative transport from the flame to the film itself, reflecting incident thermal energy in the IR range. This low emissivity also suppresses re-emission of radiation, which will lead to an increase in the film temperature. The increased film temperature is beneficial, because the intumescence and charring within the film, which impart its functional heat shielding properties, require higher temperatures to degrade the PEI and THAM.
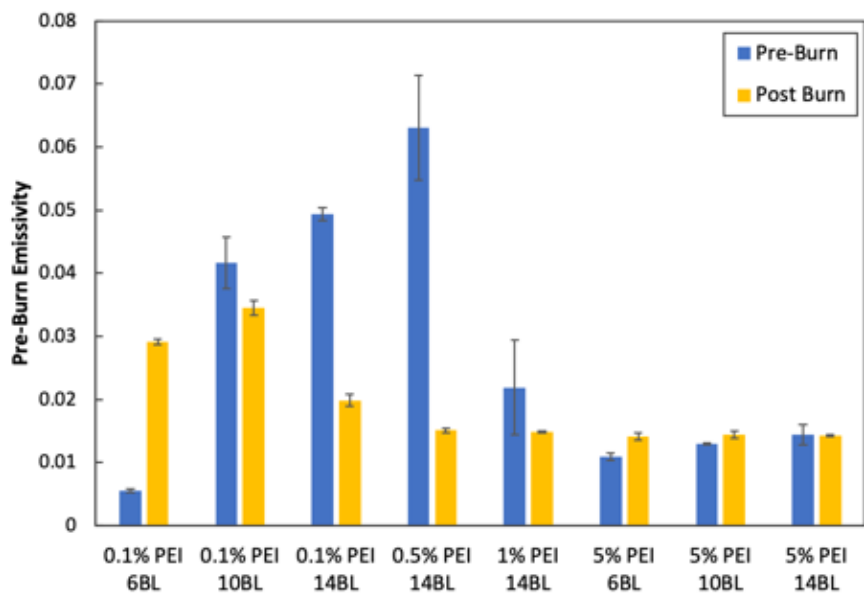
Figure 4.9. Emissivity of PEI-THAM/VMT films prior to and following flame testing.

4.4 Conclusions

Polymer−clay nanocomposite multilayer films are shown to be effective expendable thermal barrier coatings. These multilayer thin films act through a combination of chemical and structural characteristics that suppress heat transfer to the substrate. The addition of an amine salt to the film results in thicker growing nanocomposite multilayer thin films, with more material available for heat shielding. A prominent heat shielding mechanism observed is the creation of a macro-scale bubble. As the films are exposed to high levels of heat, the polymer and amine salt undergo char-forming pyrolysis, which encases the nanoclay platelets and releases gases. These gases cause the film to expand and form a ceramic bubble that effectively insulates the metal substrate. Increasing the number of polymer−clay bilayers, and consequently the material deposited, results in greater thermal resistance from larger and improved bubble formation. The generated temperature differential is further improved by increasing the PEI concentration in the deposition solution, which results in more polymer and clay adsorbed during each deposition step. The resulting thicker ceramic shell generated during flame testing (and more material available for blowing) results in heat shielding performance that is comparable to orders of magnitude thicker ceramic-based thermal barrier coatings.

CHAPTER V – SMALL MOLECULE ADDITIVES IN MULTILAYER POLYMER-CLAY

THIN FILMS FOR IMPROVED HEAT SHIELDING OF STEEL

5.1 Introduction

Small molecule additives were paired with polyethylenimine (PEI), independently and together, and grown using layer-by-layer assembly, with vermiculite (VMT) clay. LbL growth of the PEI and VMT creates a nanobrick wall structure, shown in **Figure 5.1**, which has proven to be highly effective both as a gas barrier and fire resistant coating.[106,152,172] PEI was utilized both as the mortar holding the VMT in place and as an active ingredient in the heat shielding mechanism, acting as a blowing agent during pyrolysis. VMT clay was chosen as the nanoplatelet because of its high aspect ratio and thermal stability.[66,173] Small molecule additives tris(hydroxymethyl)aminomethane (THAM), pentaerythritol (PER), and ammonium pentaborate (PB) were evaluated due to their unique heat shielding characteristics. THAM has been shown to be an effective blowing agent in flame retardant and heat shielding applications.[125,130,174] Upon exposure to high temperatures, as the THAM undergoes pyrolysis, gases are released that help with the formation of a bubbled insulating layer. In flame retardant applications, PER is often utilized as an additive due to its ability to promote carbonaceous char.[175,176] Char is important because it helps to insulate the flammable substrate, cutting off one of the key contributors for fire propagation.[12] PB is a flame retardant additive used to insulate a substrate through a glassy char that has been shown to have high thermal resistivity.[177,178] When PB is exposed to temperatures in excess of 800 °C, a glassy boric oxide char is formed, which stems fire propagation and creates a more durable char.[179,180]

These additives were investigated, individually and in tandem, to improve LbL film growth and the subsequent heat shielding properties exhibited. Ultimately, the combination of THAM and PER outperformed the other additive groupings. Improved heat shielding was achieved through a combination of consistent macroscale bubble creation, a micro- and nanoscale layering porosity effect, and molecularly disordered char. These two small molecule additives work synergistically to improve the thermal resistivity of the system, offering a cost effective heat shielding coating that is comparable to ceramic-based thermal barrier coatings.
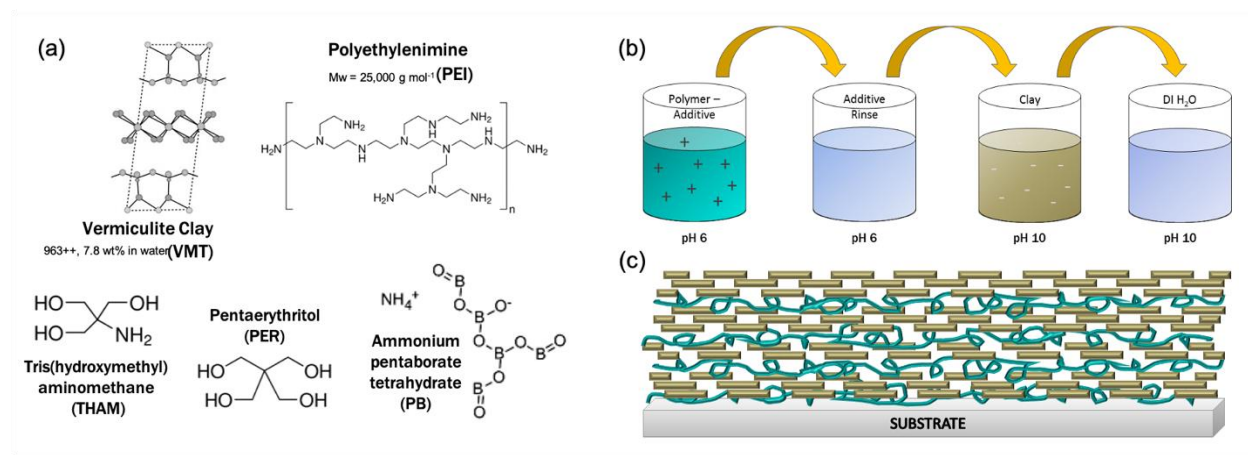
Figure 5.1. (a) Structure of polyethylenimine , vermiculite clay, tris(hydroxymethyl)aminomethane, pentaerythritol, and pentaborate. Schematics of the (b) layer-by-layer (LbL) assembly process and (c) resulting multilayer nanobrick wall coating.

5.2 Experimental

5.2.1 Materials and Methods

Branched polyethylenimine (PEI) (M_w = 25,000 g/mol), tris(hydroxymethyl)aminomethane (THAM, crystalline), ammonium pentaborate tetrahydrate (PB, ≥99%), and pentaerythritol (PER, 98%) were purchased from Sigma-Aldrich (Milwaukee, WI). Microlite 963++ vermiculite clay (VMT, 7.8 wt % in water) was purchased from Specialty

Vermiculite Corp (Cambridge, MA). Deionized (DI) water, with a resistivity equal to 18 MΩ, was used to prepare all solutions and rinses. Films were grown using an aqueous solution containing 5 wt % PEI, combined with 50mM additives. Additives were added independently (THAM, PB, and PER), and in combinations (THAM + PB, THAM + PER, PER + PB, and THAM + PER + PB), mixed into the PEI solution and the cationic rinse. Additive solutions were prepared prior to adding the PEI. VMT was diluted to a 1 wt % suspension and stirred overnight prior to use. The cationic solution and corresponding rinse pH were adjusted to 6, and the anionic solution and rinse pH were adjusted to 10, using 5 M HCl and NaOH, respectively. A36 ground low-carbon steel was purchased from McMaster Carr (Aurora, OH) as 10.16 cm × 10.16 cm × 0.32 cm plates. Metal substrates were cleaned with a DI water rinse followed by a methanol rinse and then DI water rinse again to remove any large debris. This was followed by bath sonicating in DI water and then isopropanol (IPA) for 2 minutes each, with IPA rinses between, before being dried with filtered air. The steel was then immersed in a 1 M sodium hydroxide and 100 mM sodium nitrite solution overnight to passivate the surface for better adhesion prior to deposition.

5.2.2 Thin Film Preparation

Steel substrates were coated with PEI/VMT multilayers using layer-by-layer (LbL) assembly, which was carried out with a home-built robotic system.[151] Prior to deposition, one side of the steel was taped off to ensure an uncoated side for testing. Films were assembled by first immersing the substrate into a polycationic solution for 5 minutes, followed by dipping in a rinse solution containing the additive(s) for 1 minute. From there, the substrate was immersed in the anionic clay solution for 5 minutes, and then dipped into a DI water rinse for 1 minute, which completes one bilayer (BL). Subsequent bilayers use one minute dips in each solution. The process was repeated until the desired number of bilayers were deposited. Once all the bilayers were

deposited, films were dried in ambient conditions overnight and then stored in a desiccant box prior to testing. All films were prepared with 14 BL, varying the additive species amongst samples. A schematic of the deposition procedure, and resulting nanobrick wall structure, is shown in **Figure 5.1**.

5.2.3 Torch Testing

Steel samples were mounted between two A36 steel plates (15.24 cm x 20.32 cm), with a 5.08 cm diameter circle hole to access the sample from front and back. A K-type thermocouple (McMaster-Carr; Aurora, OH) was mounted on the back side of the steel plate in the center of the hole. Silver conductive paint (Electron Microscopy Science; Hatfield, PA) was used to improve thermal contact between the steel plate and the thermocouple. A butane torch (Bernzomatic precision torch ST2200T; Worthington Industries, Columbus, OH) was oriented perpendicularly to the coated side of the sample and a flame was applied for 20 minutes. The nozzle of the butane torch was placed 1 cm away from the sample and in line with the thermocouple. Coated steel samples were compared to an uncoated steel plate tested under the same conditions.

5.2.4 Nanocomposite Film Characterization

Individual additives and each type of film were analyzed with a Q50 Thermogravimetric Analyzer (TA-instruments; New Castle, DE). Films weighing approximately 7 – 9 mg were tested in an air atmosphere. First, the materials were held at 120 °C for 20 minutes to remove water, then the temperature was increased at a heating rate of 10 °C/min. The clay composition of the freestanding films was measured using the same process. The thickness of films was measured using a dial indicator (Chicago Dial Indicator Co.; De Plaines, IL). The surface morphologies of the films after burning were observed with optical microscope (Keyence VHX-600K Digital Microscope; Itasca, IL) and then additional imaging was obtained using a field-emission scanning

electron microscope (SEM) (model JSM-7500, JEOL; Tokyo, Japan). Prior to imaging, samples were sputter coated with 5 nm of platinum/palladium. Raman spectroscopy (Horiba Jobin-Yvon LabRam HR Raman confocal microscope; Kyoto, Japan) was done to analyze the type and extent of char each film generated. Films were scanned between 800 and 2000 cm^{-1} using a 633 nm laser with 300 gr/mm grating.

5.3 Results and Discussion

5.3.1 Additive Influence on Film Growth

Films were gown with varying combinations of THAM, PER and PB added to the PEI solution and cationic rinse during layer-by-layer deposition with VMT. First, each additive was evaluated independently, then in combinations of 1:1 molar ratios, and finally all three additives were added together in a 1:1:1 ratio, using 50mM concentration for each additive. A PEI/VMT film was also grown without any additive as a control. Each coating was grown with a 5 wt% PEI aqueous solution. The influence the additives have on film growth is shown in **Figure 5.2(a)**. Both THAM and PB salts increase the growth independently by about 50%. When combined, the growth increased more than 75%, likely because more salt within the film contributes to greater charge screening and intercalation of the VMT.[125,130] Pentaerythritol is not a salt but still influences the growth, generating a film that is marginally thicker than the neat PEI/VMT. This is possibly due to hydrogen bonding that caused more PEI to remain attached during the coating process. The addition of the PER can also be seen to mitigate some of the thickening effects of the other additives. THAM + PER and PB + PER are thinner than the individual salt counter parts. Conversely, films grown with all three additives do not suffer from any impediment PER causes, instead generating a thickness roughly double (100%) that of the neat PEI/VMT film. Here the additives seem to be working together, with the charge screening and intercalation benefits from

the salt additives combining with the hydrogen bonding from the PER. From **Figure 5.2(b),** it appears that the additives have no apparent influence on the amount of clay deposited in each sample.
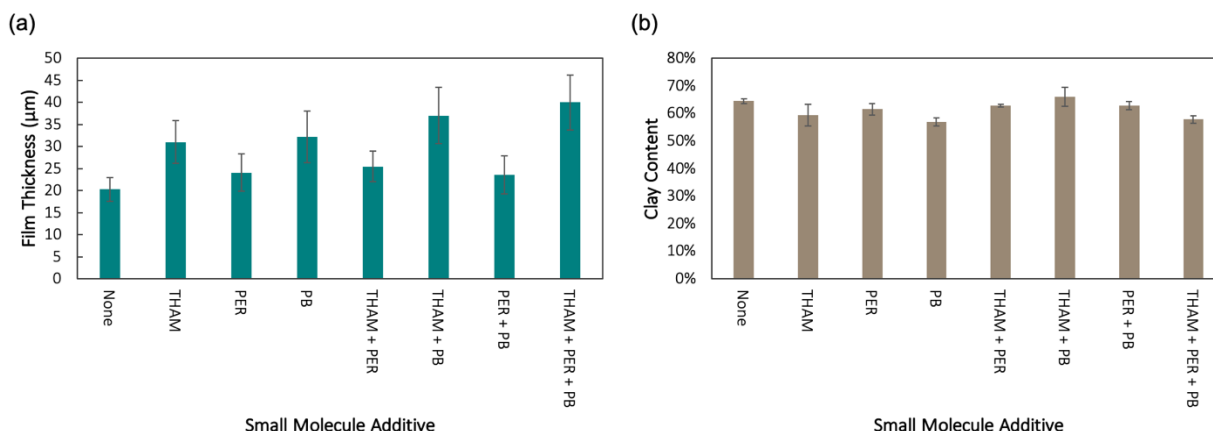
Figure 5.2. (a) Thickness of 14 BL PEI/VMT films with varying additive(s) and (b) clay content of films measured using thermogravimetric analysis.

5.3.2 Multilayer Coating Heat Shielding

Films with varying additives were tested by exposing the coated side of the steel to the flame from a butane torch for 20 minutes and compared by recording the temperature change on the back side (i.e. uncoated side) of each sample. **Figure 5.3(a)** shows the setup of the flame test. In tandem with film testing, the individual components were evaluated with thermogravimetric analysis (TGA) (**Fig. 5.3(b)**). PEI and two of the additives, THAM and PER, decompose completely before 400 °C, undergoing pyrolysis and releasing gases. When PB is exposed to high temperatures, instead of completely decomposing, it forms a boric oxide glassy residue. VMT remains stable at high temperatures, but a slight reduction in weight can be seen as the surfactants that are part of the aqueous suspension decompose Upon exposure to flame, the PEI and additives in the sample undergo pyrolysis, degrading and releasing gases. The gases become trapped

between the remaining clay filled char layer and the steel, forcing the film to expand to form an insulating shell. Films with PB likely generate a more durable char due to the presence of the boric oxide. Ultimately, though the char may have higher strength, the boric oxide hinders the expansion of the insulating shell, which results in poorer shielding performance.
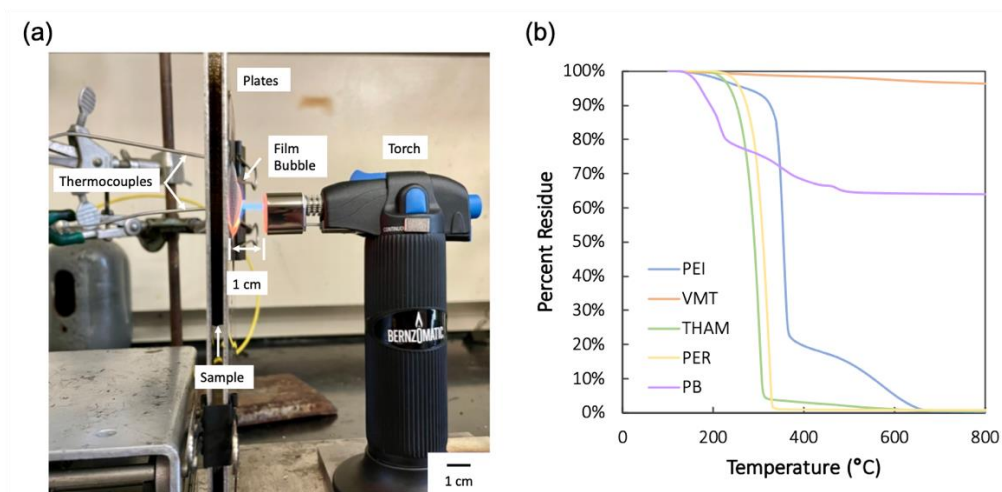
Figure 5.3. (a) Digital image of the flame test setup, with components and sample labeled, and (b) thermogravimetric analysis of the individual materials used in making the multilayer films.

The temperature curves for each of the samples during the 20 minutes of flame testing can be seen in **Figure 5.4**. As detailed in a previous study, the formation of a large bubble is paramount to achieving high thermal resistivity.[174] Generally, the films with PB perform poorly, with the film containing the individual pentaborate additive only obtaining a 60 °C differential. This is likely due to the glassy residue that PB generates, which restricts the growth of the protective bubble. The film without any additives outperformed the PB and PB + PER films, likely due to the high level of polymer available for blowing. The only film with PB that has consistent bubble generation is the film with all of the additives (i.e. THAM + PER + PB). For this film, the combined effects of the THAM and PER largely overcome the limitations of the PB additive. This combined sample, in addition to films containing individual THAM and PER (and THAM + PER), generate higher

thermal resistivities and exhibit consistent bubble formation. THAM + PER generates the greatest temperature differential. To evaluate if this result simply stems from the presence of more additive, the growth of the films and the subsequent thermal resistivity was evaluated for THAM + PER at ratios of 3:1 and 1:3. No difference in film growth is observed with changing ratio, but there is a reduction in shielding performance as one or the other of the additive mechanisms dominates. Consequently, the superior performance of THAM + PER is a result of the combined mechanisms, each acting in tandem to improve the thermal resistivity.
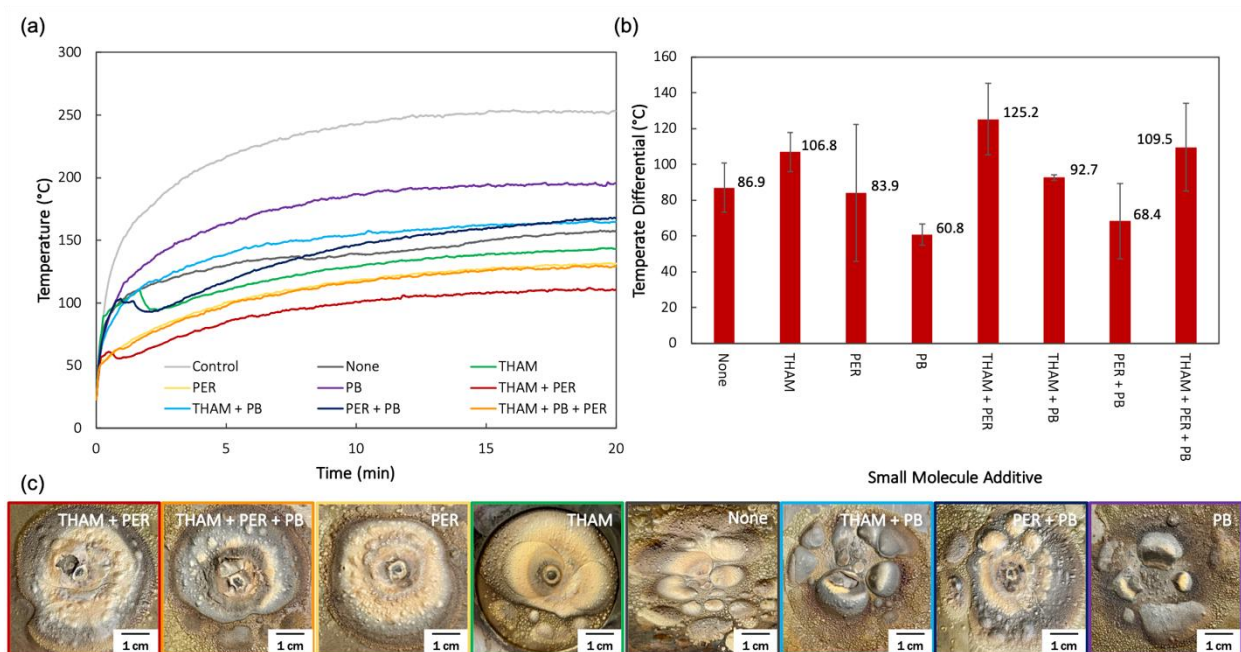
Figure 5.4. (a) Temperature curves during torch testing of 14 BL films on steel, (b) the resultant temperature differential when compared to the uncoated control substrate ($\Delta T_{film} = T_{max,control} - T_{max,film}$), and (c) the morphology of each of the samples following the torch testing.

The eventual formation of the bubble, or not, is generally consistent, but the exact timing and scale of the bubble is driven by the entropic nature of pyrolysis. The initial two minutes of testing has the most activity and is often predictive of how the film will perform overall. **Figure 5.5** focuses on the first two minutes of torch testing and highlights the bubble formation and resulting influence on thermal diffusivity. Definitive changes in the temperature recorded for

various samples can be seen. These sharp changes in temperature occur initially when the bubble first starts to grow, particularly as the film is forced away from the steel and a pocket of gas insulates it. This gaseous insulation improves when the bubble expands, as seen in points 2, 4, and 6. In each instance, the temperature temporarily decreases as the heat must traverse a greater distance to get to the vulnerable steel. This highlights the importance of the macroscale bubble in creating an effective thermal barrier.
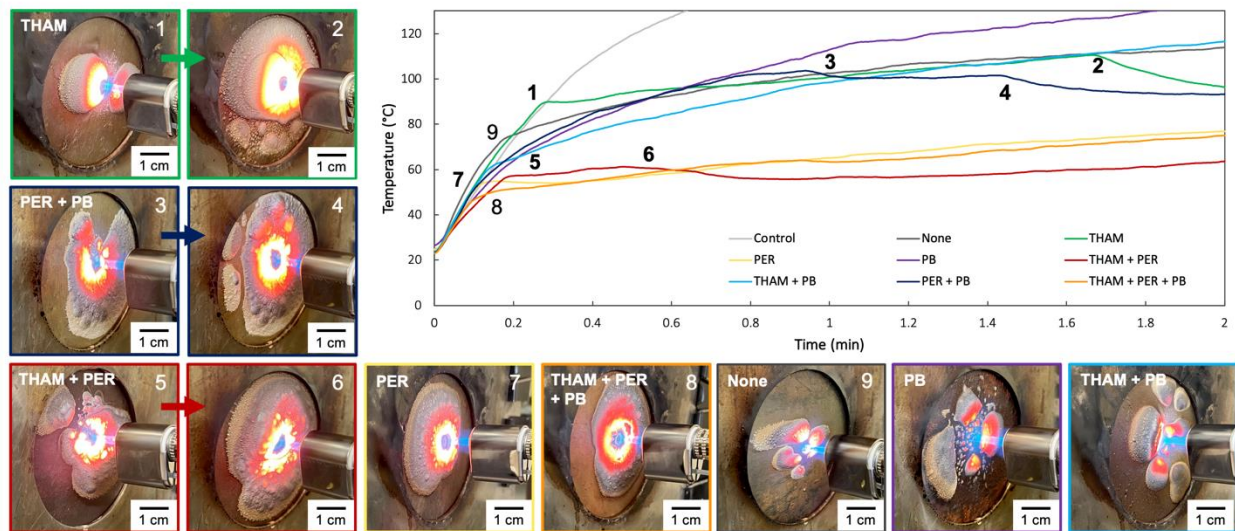
Figure 5.5. Formation of macroscale bubbles and the backside recorded temperature of the steel for each of the film types: No additive (gray), THAM (green), PER (yellow), PB (purple), THAM + PER (red), THAM + PB (blue), PB + PER (navy), and THAM + PB + PER (orange). Numbered points on the graph correspond to the surrounding film images.

5.3.4 Influence of Bubble Architecture

Material architecture has long been understood to be an integral part of the thermal resistance exhibited by heat shielding coatings. Films with pores generate greater thermal resistivity, whereas coatings with a greater level of filler interconnectivity can increase thermal conductivity.[181–183] For some of the samples, particularly those with THAM and PER as the additives, the bubble created is comparable on the macroscale level, each taking a large area of

the testing space. To evaluate the difference between these coatings, the structure and char formation of the bubbles are evaluated. **Figure 5.6** shows cross-sectional images of the four best performing films after testing, along with optical microscope images. The film that was grown with only THAM creates a cohesive macroscale bubble, with one large cavity, and is the only film that can be sheared to see the internal structure. The intermolecular bond strength of films with THAM is greater than the films grown with other additives, causing the film to be more durable, even after burning. This is likely because the hydrogen bonds formed between THAM and PEI are stronger as the NH_2 groups preferentially bond.

Bubbles formed by films without THAM, or with additional additives alongside, do not exhibit the same singular cavity between film and substrate. Optical images of these bubbles show that films with PER as one of the additives exhibit layering. This layered bubbling generates even greater thermal resistivity from the additional microdomains the energy must travel through. These pockets result as gases released during pyrolysis not only separate the film from the substrate but also delaminates the clay platelet layers. In the case of the film containing both THAM and PER, the two additives work synergistically to create a larger bubble, similar in scale to the neat THAM bubble, and the layering effect that diminishes heat transfer across the system. The addition of PB to the system results in reduced performance. While the THAM and PER still work in tandem to generate a large, layered bubble, the boric oxide from the PB still hinders the growth of the bubble, lessening the overall thermal resistance of the film.
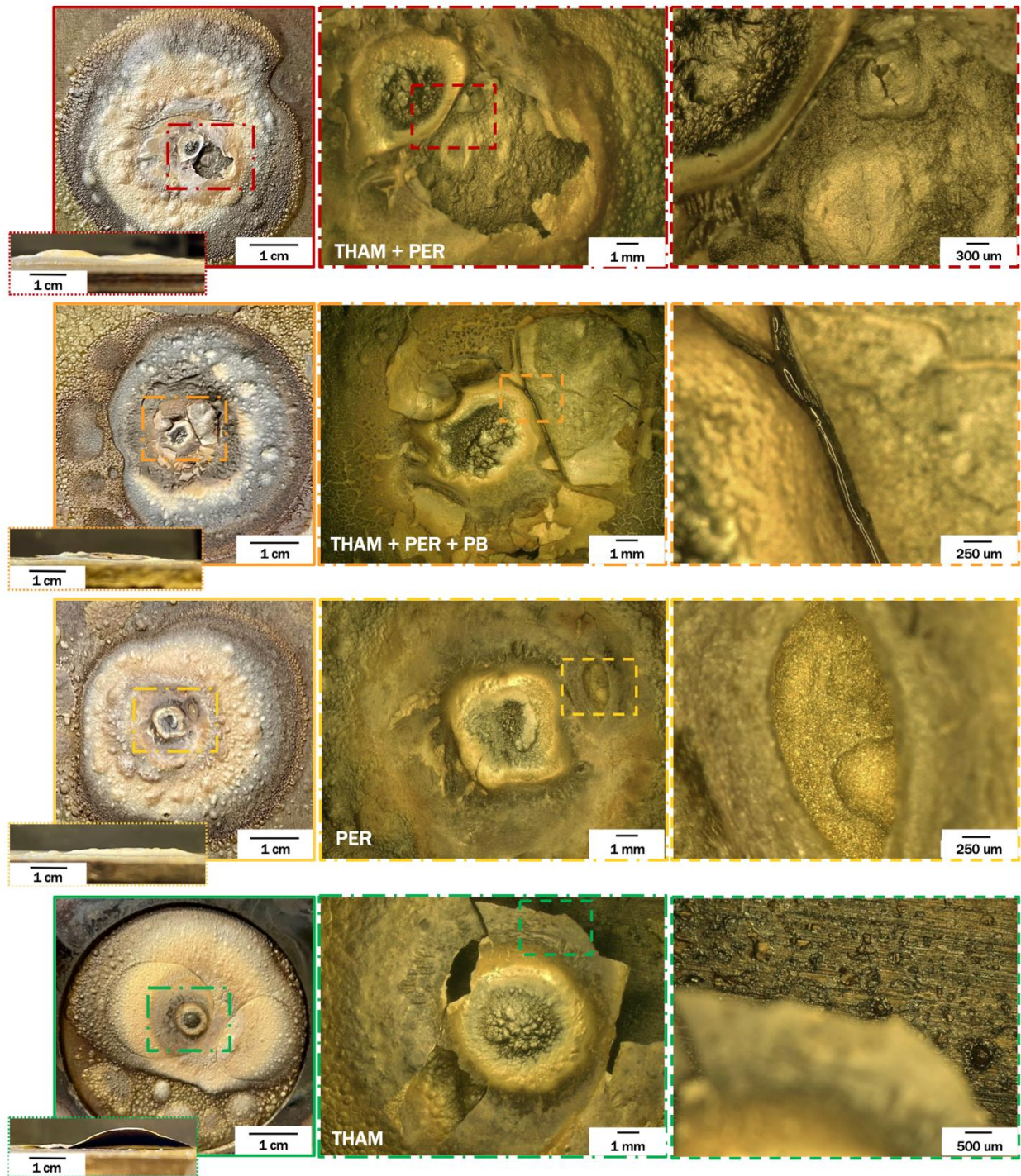
Figure 5.6. Digital and optical images of 14 BL films with THAM + PER (red), THAM + PER + PB (orange), PER (yellow), or THAM (red) after torch testing and corresponding cross-sectional image of each. Across each row, images of the bubble architecture are progressively zoomed in.

Another key feature in the architecture of the films after pyrolysis are nanodomains. SEM images of the films after burning, shown in **Figure 5.7**, reveals nano-characteristics that mimic the macroscale analysis. Three of the films (THAM + PER, PER, and THAM) exhibit nanoporosity. This nanoporosity results as the film intumesces and gases are trapped. Nanoporosity in thermal barrier coatings has been demonstrated to be effective at hindering thermal transport due to phonon scattering.[184–186] The film with the combined additives (THAM + PER + PB) does not display nanoporosity. While a macroscale bubble and layering result when the THAM and PER undergo pyrolysis, the PB that limits the bubble formation also likely hinders nanopore formation. In addition to the nanoporosity, the PER film shows signs of microscale layering. Like the larger pockets, these smaller pockets hinder thermal diffusion and provide additional surface for the presence of the intumesced bubbles to generate upon. The film with just THAM exhibits extensive nano- and microporosity but the cohesion in the film limits the expansion of these bubbles. The THAM + PER film manifests this same microscale porosity but to a greater extent, as the bubbles are larger and layered pockets are evident. This mimics the macroscale analysis in that THAM and PER contribute equally to the physical architecture of the intumesced coating and to the corresponding overall mechanism of heat shielding.
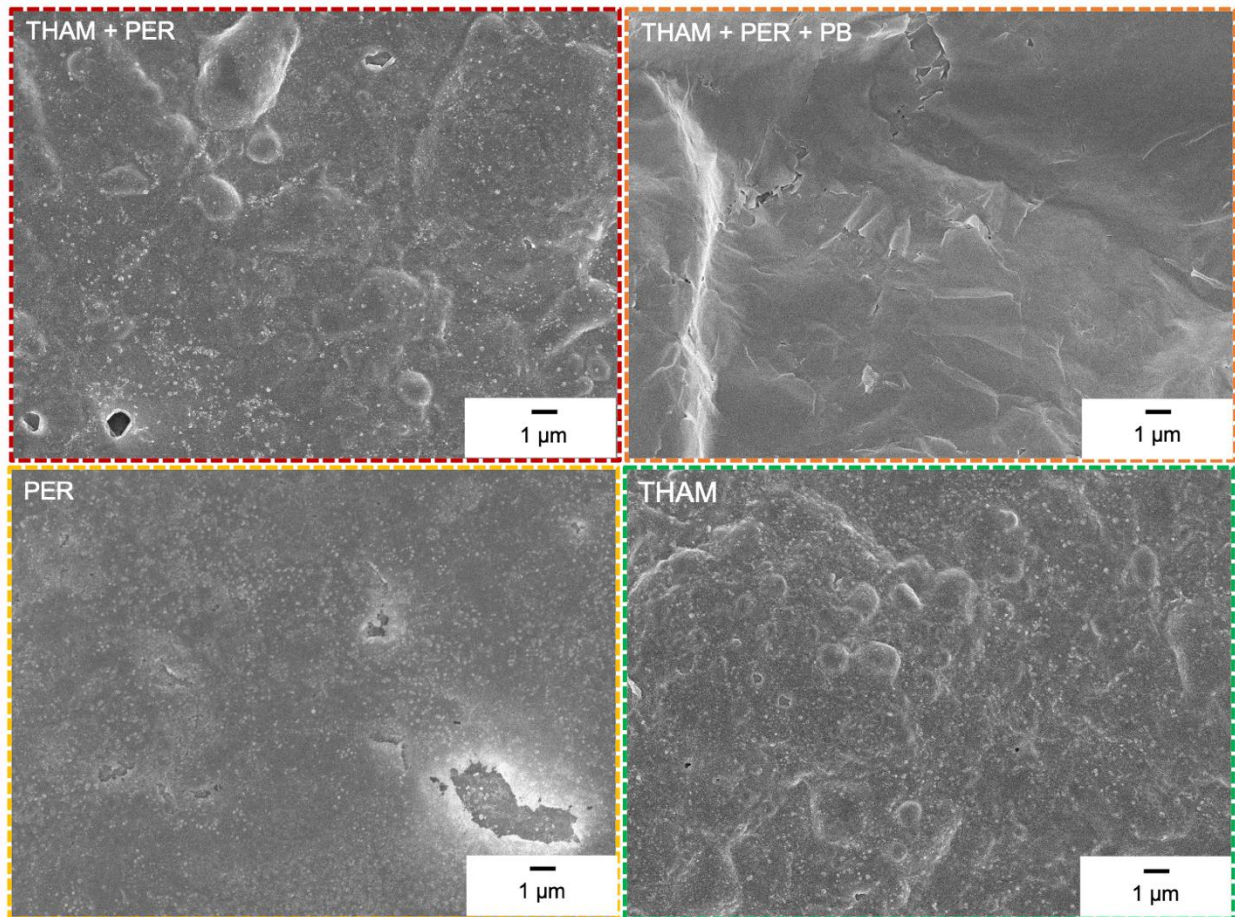
Figure 5.7. SEM images of 14 BL films with varying additives: THAM + PER (red), THAM + PER + PB (orange), PER (yellow), and THAM (green). Nanoporosity and microscale layering and bubbling, that contribute to the overall film thermal resistivity, can be observed.

In addition to physical structure, the molecular architecture of the material influences the thermal resistivity of the system. **Figure 5.8** shows the Raman analysis of the burnt films, which provides insight into the type and extent of char generated by each of the best performing samples. The bands of interest are the graphitic and defect bands, G-bands and D-bands, respectively.[187] The degree of disorder in carbonaceous materials can be described by the ratio of the intensity of the D-band peak relative to the G-band peak (I_D/I_G), where a larger ratio indicates greater disorder. The films with THAM and PER, independent of each other, have a distinct, sharp peak in the graphitic range. This Lorentzian style peak is indicative of well-ordered crystalline graphitic

char.[188] Though both exhibit the graphic char, the PER film, which has a higher intensity peak, has more char content than the THAM film, likely contributing to the better heat shielding. Conversely, the film containing THAM and PER together exhibits a low-profile Gaussian curve in the graphitic band region, which is representative of disorder and defects in the graphene.[189] The larger intensity curve in the defect band region, and consequently the larger I_D/I_G ratio is further indication of the disordered nature of this sample's char. The disordered atomic morphology results in more energy needed for thermal carriers to transport heat to neighboring sites.[190,191] This results in a loss of energy and subsequently less heat transferred. By contrast, graphitic char is thermally conductive, so even though there is more charring present it does not stem the heat as effectively. The film with the combined THAM, PER, and PB does not have any definitive peaks, likely because any carbonaceous charring that results is dominated by the boric oxide.
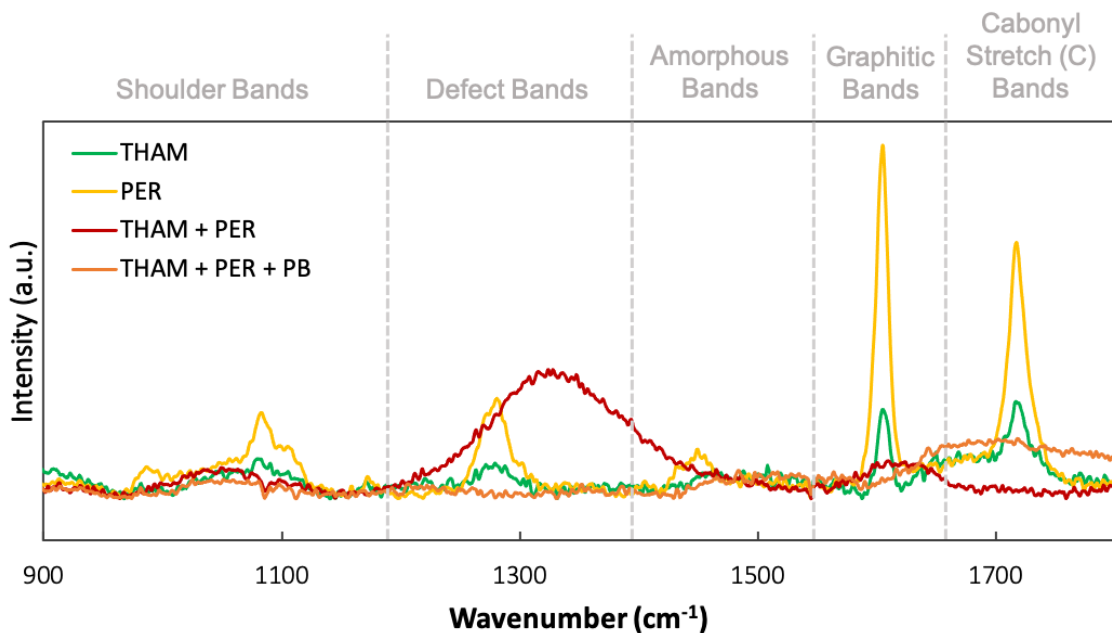
Figure 5.8. Raman spectra of 14 BL films after torch testing, showing definitive differences in the charring exhibited by the samples containing THAM (green), PER (yellow), THAM + PER (red), and THAM + PER + PB (orange).

5.4 Conclusions

Small molecule additives tris(hydroxymethyl)aminomethane, pentaerythritol, and pentaborate have a direct influence on the growth and heat shielding exhibited by PEI/VMT multilayer films. Each contributes to the film thickness, though THAM and PB contribute to substantially thicker growth due to charge screening of the polymer. The insulating role of the macroscale bubble is highlighted, as samples that do not form a cohesive bubble offer less thermal resistivity. This is particularly evident in films containing PB, which forms boric oxide at high temperatures that hinders the bubble creation. The most successful heat shielding coating contains PER and THAM together. Fourteen bilayer films consistently create a large macroscale bubble that exhibit a layering effect, in both the macro- and nanoscale domains, in addition to disordered char. Consequently, the two additives working together most effectively stems heat transfer through the combination of energy lost in the transport between various micro- and macrodomains, phonon scattering in nanodomains, and poor thermal diffusion along disordered molecular char.

CHAPTER VI – CONCLUSIONS AND FUTURE WORK

6.1 Thin Film Functionalization for Corrosion and Thermal Barrier Coatings

This dissertation has outlined several novel methods for improving the performance of polymer-clay thin films for the protection of steel from corrosion and thermal deterioration. The crosslinking and silanization of the nanobrick wall film helped to stem water absorption and improve adhesion of the film to the substrate, respectively, both of which were key factors in the success of corrosion barrier coatings. The addition of an amine salt, and a higher concentration of polymer in the deposition process, promoted thick growth of the film and provided the needed material for the creation of an insulating bubble. The presence of small molecule additives in the thick polymer-clay film generated additional thermal resistivity through the promotion of a more complex architecture within the insulating bubble and disordered charring.

6.1.1 Crosslinking and Silanization of Clay-Based Multilayer Films for Improved Corrosion Protection of Steel

Chapter III highlighted the viability of using polymer-clay nanobrick wall coatings as a primer in a multilayer insulating coating for corrosion protection. The barrier performance of the nanobrick wall was improved through the crosslinking of the polymer matrix with glutaraldehyde, improving moisture resistance and reducing diffusion of corrosive species through the film. Silanization of the steel-coating interface with APTES improved adhesion, reducing delamination, and subsequently improving the charge transfer resistance of the system. With this combined functionalization, a 30 BL PEI/VMT film (300 nm thick), with an epoxy topcoat, demonstrated more stable corrosion resistance over a 5-day testing period when compared to a neat epoxy system.

6.1.2 Efficient Heat Shielding of Steel with Multilayer Nanocomposite Thin Film

Chapter IV presented the use of a polymer-clay nanocomposite multilayer film for heat shielding. The combination of THAM, used as a buffer additive in the PEI and its rinse, and a 5% PEI solution generate a thicker growing film through charge screening, polymer kinetics, and intercalation. The 35 um, 14 BL PEI-THAM/VMT film stems heat transfer to the underlying steel through a combination of structural characteristics and material properties. Upon exposure to high levels of heat from a butane torch, the material intumesces to form a ceramic bubble that insulates the steel. The macroscale bubble, coupled with the high emissivity of the material, generates a large thermal resistivity across the system and a temperature differential of over 100 °C results.

6.1.3 Small Molecule Additives in Polymer-Clay Thin Films for the Promotion of Thick Growth and Improved Thermal Shielding

Chapter V showed how the heat shielding of the film in Chapter IV can be improved through the addition of small molecule additives. THAM, pentaerythritol (PER) and ammonium pentaborate (PB) were used as additives in the coating process. The addition of THAM and PER to a 14 BL PEI/VMT thick clay coating demonstrated the highest thermal resistivity. A more complex bubble architecture, with micro- and nano-layers, worked in tandem with additional disordered charring to decrease thermal transport through the system.

6.2 Heat Shielding of Carbon Fiber Reinforced Polymer Composites

6.2.1 Introduction

The studies presented in this dissertation focus on the protection of steel using polymer-clay nanocomposites. A natural extension of this research is evaluating these coatings in the protection of carbon fiber reinforced polymer (CFRP) composites. Like steel, carbon fiber composites have a high level of mechanical strength, toughness, and rigidity.[192] Additionally, they have several advantages over steel, including corrosion resistance, fatigue resistance, a high strength-to-weight ratio, and are non-magnetic.[193,194] As a result, CFRP composites have attracted attention for applications in a wide range of fields including aerospace, civil engineering, and automotive. Similar to steel, the excellent mechanical properties achieved by CFRP composites degrades at elevated temperatures.[195] This is a consequence of the thermal properties of the polymeric matrix, which softens as it reaches its glass transition temperature (T_g) and then decomposes once it obtains its decomposition temperature (T_d).[196] The range of thermal degradation is dependent on the specific polymer used, but is generally between 100 and 200 °C for the T_g and rarely above 400 °C for the full degradation.[197,198] Studies have shown that the strength of the CFRP composite can decrease by more than 50% at these elevated temperatures, limiting its use in many applications. The mechanical properties of the composite are dependent on the quality of the interfacial bonding between the fibers and the polymer matrix, and the corresponding stress transfer capability of the matrix.[199–201] The nanobrick wall nanocomposite heat shield, detailed in Chapters IV and V, shows efficacy in protecting, and subsequently extending the life of, carbon fiber reinforced polymer composites at elevated temperatures.

6.2.1 Preliminary Test Results

10 and 15 BL of PEI-THAM/VMT were deposited on CFRP composite samples using LbL assembly. The deposition process follows the procedure outlined in Chapter IV, except an additional drying step was used after each bilayer to prevent film delamination. A 5 wt% PEI solution containing 50mM THAM was prepared and the pH was adjusted to 6. A 50mM THAM solution was also used as the cationic rinse at pH 6. The VMT suspension was diluted to 1 wt%. The VMT and the DI water anionic rinse were adjusted to pH 10. Prior to coating, CFRP composite samples were cleaned by rinsing with water, methanol, and then water again followed by drying with compressed air. The samples were then corona treated to provide negative surface charge prior to LbL deposition. For the first BL, samples were immersed in the PEI-THAM solution for 5 minutes, followed by rinsing in the cationic rinse for 1 minute. Next, the sample was immersed in VMT for 5 minutes and then rinsed in DI water for 1 minute. This completed the first bilayer and all subsequent BL used one minute dip times for each solution. Following each BL, the sample was placed in an over at 70 °C for 15 minutes before beginning the subsequent bilayer deposition.

To demonstrate the viability of the coating with the new substrate, a combined torch and mechanical test was performed. Neat composite, 10, and 15 BL PEI-THAM/VMT samples were compared. The samples were first mounted in an Instron Universal Testing Machine and a butane torch was aligned with the center of the sample, with the nozzle kept 1 inch from the sample. A thermocouple was placed directly opposite the nozzle to record the temperature rise of the sample, and silver paint was used to improve the thermal interface between the sample and thermocouple. The set up is shown in **Figure 6.1**. The samples were then placed under a fixed 0.5% strain and the flame applied for 10 seconds. The temperature increase and the drop in load over 10 seconds were recorded.
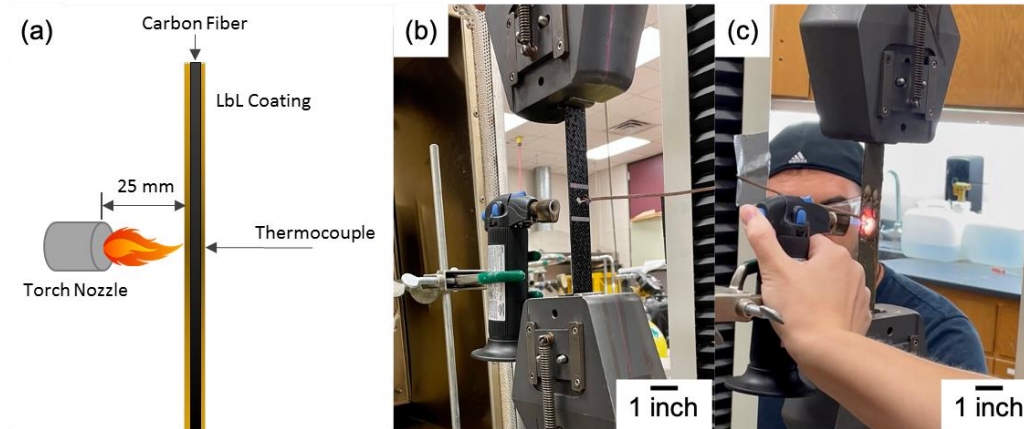
Figure 6.1. (a) Schematic of the butane torch flame and mechanical testing. Digital images from (b) the front, facing away from the torch with the thermocouple adhered, and (c) the back, the side exposed to the flame.

Upon exposure to the flame, the neat sample catches fire and burns for the entire 10 seconds of testing, before being manually extinguished. This confirms the flammability of the epoxy resin. Conversely, the samples with the polymer-clay shield do not catch fire. Instead, coated samples display intumescent bubbling, seen in **Figure 6.2(a)**, which creates a physical barrier, insulating the CFRP composite from the flame. As a result, any deterioration of the composite's mechanical properties is due to the heat transfer across the coating system. **Figure 6.2(b)** shows a closer look at the composite substrates following burning. The control sample (i.e. neat CFRP composite) shows clear signs of damage where the flame burned the epoxy matrix. The epoxy has completely decomposed, exposing the carbon fibers. By contrast, the samples coated with 10 and 15 BL appear largely untouched, displaying only minor signs of polymer softening.
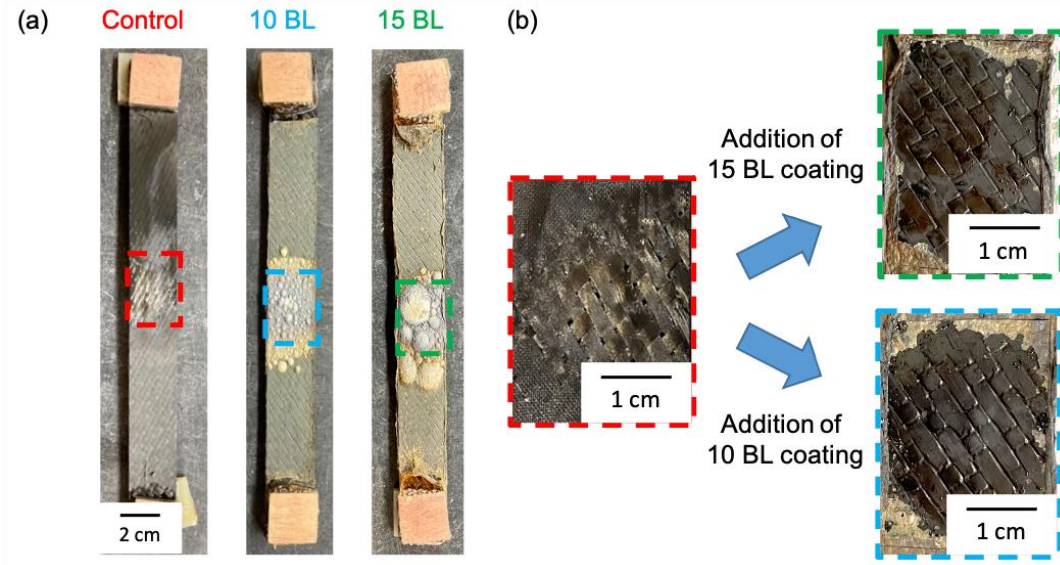
Figure 6.2. (a) Digital images each of PEI-THAM/VMT coated and uncoated (control) composite samples after exposure to the butane torch for 10 seconds. (b) Close up digital images of the uncoated composite, and the 10 and 15 BL coated samples with the intumescent bubbling cut away to show the exposed carbon fiber.

The temperature and stress analysis of the samples (**Fig. 6.3**) corroborates the conclusion that the polymer-clay coating provides substantial heat shielding for the composite. After 10 seconds of testing, the temperature on the backside of the uncoated sample was approximately 180 °C. With the addition of the 15 BL PEI-THAM/VMT coating, the recorded temperature reduced to 80 °C, indicating an increase in the overall thermal resistivity of the system. In addition to the substantial temperature differential between the neat and coated samples, the reduction in stress deterioration is significant. Without the heat shield the composite stress drops by 25% during the 10 seconds of testing. While some level of stress drop is expected, due to material relaxation, the significant drop can only be attributed to the decomposition of the epoxy matrix. Conversely, the samples coated with 10 and 15 BL only experienced 15 and 10% drops in load, respectively. The difference in performance is attributed to the internal temperature felt by the composite and its comparison to the glass transition temperature of the epoxy. As each sample still shows the

presence of the epoxy (**Fig. 6.2(b)**), the extent of mechanical degradation correlates with the extent of softening. The 15 BL sample, which experiences less heat, has less polymer softening, and therefore retains more of its mechanical strength. These preliminary results show a lot of promise, but further testing and characterization is needed to fully understand the extent of protection offered by the PEI-THAM/VMT coating.
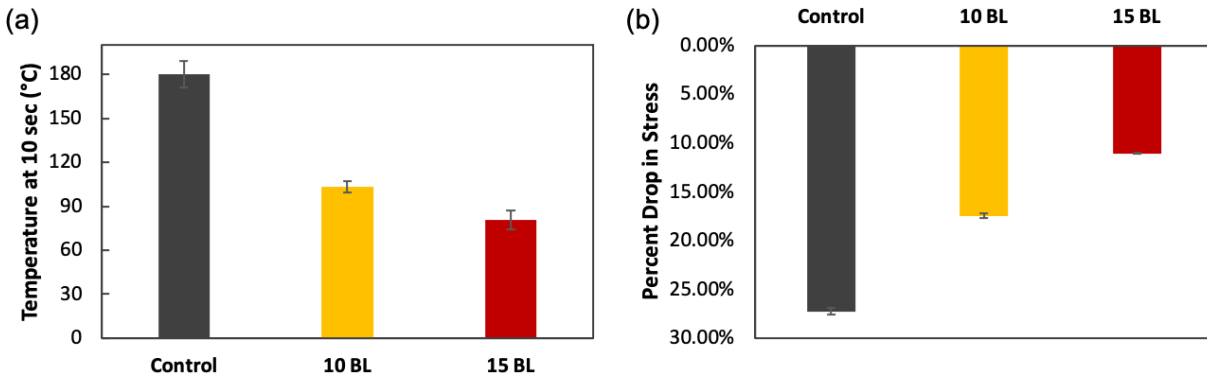
Figure 6.3. (a) The temperature felt, on the opposite side of the sample from the flame, after 10 seconds of torch testing. (b) The reduction in stress experienced by the composite after the flame was applied.

6.2.3 Next Steps

The next step of the CRFP composite study will investigate the ability of the PEI-THAM/VMT film to offer further thermal insulation. Given the additional protection the 15 BL coating exhibits, a sample coated with a 20 BL film will be tested. Both the study in Chapter IV and the preliminary testing for this research demonstrate that a thicker film offers additional protection. To truly determine the extent of protection offered, a sample will also be tested following the same procedure, but without applying the flame. This will provide a comparison for what amount of thermal degradation is still experienced by the coated composite. Material characterization will also help with determining if any deterioration of the carbon fiber has taken place. Carbon fiber reinforced polymer composites that experience thermal degradation show signs of oxidation.[196] X-ray photoelectron spectroscopy (XPS) of the composite substrate after

burning, both coated and uncoated, will demonstrate what extent of oxidation is present. Additionally, SEM will be used to see what, if any, damage has been physically done to the coated substrates. Carbon fiber composites that have experienced temperatures at or above the T_g of the polymer matrix will likely show signs of delamination from the carbon fibers.

Once the general insulation of these films has been established, the durability of the films will be tested. Extended testing of the samples will provide insight into how long the thermal protection can be maintained. The set up for this test will be similar to the initial test but instead of the time being held constant, the expected drop in load will be constant. The time it takes for a sample's load to drop a prescribed amount is driven by the thermal diffusion rate through the insulating systems, with thicker films likely leading to a longer lifespan of the underlying CFRP composite. Another test will evaluate cyclic loading of the samples. For this experiment, the samples will be placed under the same strain (e.g. 0.5%) and subjected to the flame for a fixed period of time (e.g. 30 seconds). The flame will be removed and the sample allowed to cool down before the flame is applied again for the same amount of time. This will be repeated a few times and the relaxation curves compared to determine if damage from previous cycles influences the relaxation time in future cycles.

6.2.4 Conclusion

The potential for polymer-clay multilayer coatings to offer heat shielding to carbon fiber composites is demonstrated. The addition of the thick growing nanobrick wall film will extend the life of a CFRP composite at temperatures above the T_g and T_d of the polymer matrix. The proposed study seeks to develop a full understanding of the extent of protection offered by these coatings and determine the long-term durability of the system. This type of coating will significantly extend the functionality of epoxy-based composites for applications in elevated temperatures.

6.3 Polyelectrolyte Complexes for Thermal and Corrosion Protection

While layer-by-layer assembly of coatings has many advantages, a consistent drawback is the number of processing step needed to achieve the excellent barrier properties. This is particularly a problem in commercial applications, where the ability to achieve the same barrier properties with reduced processing time/steps is highly desired. Recently, polyelectrolyte complex coatings (PECs) have gained in popularity for their ability to offer comparable gas barrier and flame retardant behavior with only a few processing steps.[15–17,202] Like LbL coatings, PECs involve the combination of a polycation and polyanion to generate a thin film. Instead of depositing these opposing species in layers, they are combined into one solution and deposited with a single step followed by a curing step. To deposit oppositely charged polyelectrolytes or nanoparticles simultaneously in one film, the electrostatic interactions must be inhibited to prevent complexation.[203] Mixing oppositely charged polyelectrolytes can result in an insoluble complex, metastable coacervate, or soluble solution. The complexation of the two species is driven by the intrinsic (polycation-polyanion) versus extrinsic (polyelectrolyte-counterion) pairs and is tuned by altering the pH, salt concentration, or combining under precise ratios.[204] Depending on the viscosity and density the film is generally applied via dip coating or bar coating. In the latter case, thickness is largely driven by the bar gap during the deposition, while in the former it is dependent upon the solution viscosity.[205,206]

One of the advantages to LbL coatings is the control over nanostructure, such as the highly aligned nanobrick wall structure. However, recent studies have found that clay nanoplatelets preferentially align when incorporated into a PEC and deposited via blade coating.[205,207] One example of this is a study that utilized chitosan (CH) and MMT in a PEC coating for flame

retarding acrylic fabric.[207] Solutions of the two species were first created, at 0.1 wt% and 2 wt%, respectively, and then combined at a 1:1 volume ratio and centrifuged to allow for separation of the resultant coacervate and polymer-poor liquid. The supernatant was removed, and the remaining gel coated via doctor-blading. This generated a preferentially aligned nanobrick wall structure with high clay loading. This type of coating can be used in developing nanobrick wall PECs for corrosion and/or thermal barrier applications that would be easier to apply in an industrial setting than LbL coatings. Initial experimentation can focus on a PEI/VMT PEC, following the deposition process outlined above. The ratio of polymer to clay can be tailored and compared to achieve more desirable end properties. For anti-corrosion applications, similar crosslinking and silanization steps as those in Chapter III can be evaluated. For heat shielding, PER and/or THAM can be added to the PEC before centrifuging.

REFERENCES

(1)   El Haggar, S. M. Rural and Developing Country Solutions. In *Environmental Solutions*; Elsevier, 2005; pp 313–400. https://doi.org/10.1016/B978-012088441-4/50015-0.

(2)   Iron and steel - Introduction to their science, properties, uses http://www.explainthatstuff.com/ironsteel.html (accessed 2020 -01 -29).

(3)   Revie, R. W.; Uhlig, H. H. *Corrosion and Corrosion Control: An Introduction to Corrosion Science and Engineering*, 4th ed.; Wiley-Interscience: Hoboken, N.J, 2008.

(4)   Thakare, J. G.; Pandey, C.; Mahapatra, M. M.; Mulik, R. S. Thermal Barrier Coatings—A State of the Art Review. *Met. Mater. Int.* **2021**, *27* (7), 1947–1968. https://doi.org/10.1007/s12540-020-00705-w.

(5)   Kadlec, M.; Haušild, P.; Siegl, J.; Materna, A.; Bystrianský, J. Thermal Fatigue Crack Growth in Stainless Steel. *International Journal of Pressure Vessels and Piping* **2012**, *98*, 89–94. https://doi.org/10.1016/j.ijpvp.2012.07.005.

(6)   Gharbi, O.; Thomas, S.; Smith, C.; Birbilis, N. Chromate Replacement: What Does the Future Hold? *npj Materials Degradation* **2018**, *2* (1), 1–8. https://doi.org/10.1038/s41529-018-0034-5.

(7)   Feuerstein, A.; Knapp, J.; Taylor, T.; Ashary, A.; Bolcavage, A.; Hitchman, N. Technical and Economical Aspects of Current Thermal Barrier Coating Systems for Gas Turbine Engines by Thermal Spray and EBPVD: A Review. *J Therm Spray Tech* **2008**, *17* (2), 199–213. https://doi.org/10.1007/s11666-007-9148-y.

(8)   Shchukin, D. G.; Zheludkevich, M.; Yasakau, K.; Lamaka, S.; Ferreira, M. G. S.; Möhwald, H. Layer-by-Layer Assembled Nanocontainers for Self-Healing Corrosion Protection. *Advanced Materials* **2006**, *18* (13), 1672–1678. https://doi.org/10.1002/adma.200502053.

(9)   Lakiza, S. M.; Grechanyuk, M. I.; Ruban, O. K.; Redko, V. P.; Glabay, M. S.; Myloserdov, O. B.; Dudnik, O. V.; Prokhorenko, S. V. Thermal Barrier Coatings: Current Status, Search, and Analysis. *Powder Metall Met Ceram* **2018**, *57* (1–2), 82–113. https://doi.org/10.1007/s11106-018-9958-0.

(10)   Priolo, M. A.; Holder, K. M.; Guin, T.; Grunlan, J. C. Recent Advances in Gas Barrier Thin Films via Layer-by-Layer Assembly of Polymers and Platelets. *Macromol. Rapid Commun.* **2015**, *36* (10), 866–879. https://doi.org/10.1002/marc.201500055.

(11)   Holder, K. M.; Smith, R. J.; Grunlan, J. C. A Review of Flame Retardant Nanocoatings Prepared Using Layer-by-Layer Assembly of Polyelectrolytes. *J Mater Sci* **2017**, *52* (22), 12923–12959. https://doi.org/10.1007/s10853-017-1390-1.

(12)   Lazar, S. T.; Kolibaba, T. J.; Grunlan, J. C. Flame-Retardant Surface Treatments. *Nature Reviews Materials* **2020**, 1–17. https://doi.org/10.1038/s41578-019-0164-6.

(13) Richardson, J. J.; Cui, J.; Björnmalm, M.; Braunger, J. A.; Ejima, H.; Caruso, F. Innovation in Layer-by-Layer Assembly. *Chem. Rev.* **2016**, *116* (23), 14828–14867. https://doi.org/10.1021/acs.chemrev.6b00627.

(14) Andreeva, D. V.; Skorb, E. V. 13 - Multi-Layer Smart Coatings for Corrosion Protection of Aluminium Alloys and Steel. In *Handbook of Smart Coatings for Materials Protection*; Makhlouf, A. S. H., Ed.; Woodhead Publishing, 2014; pp 307–327. https://doi.org/10.1533/9780857096883.2.307.

(15) Palen, B.; Kolibaba, T. J.; Brehm, J. T.; Shen, R.; Quan, Y.; Wang, Q.; Grunlan, J. C. Clay-Filled Polyelectrolyte Complex Nanocoating for Flame-Retardant Polyurethane Foam. *ACS Omega* **2021**, *6* (12), 8016–8020. https://doi.org/10.1021/acsomega.0c05354.

(16) Kolibaba, T. J.; Grunlan, J. C. Environmentally Benign Polyelectrolyte Complex That Renders Wood Flame Retardant and Mechanically Strengthened. *Macromol. Mater. Eng.* **2019**, *304* (8), 1900179. https://doi.org/10.1002/mame.201900179.

(17) Haile, M.; Sarwar, O.; Henderson, R.; Smith, R.; Grunlan, J. C. Polyelectrolyte Coacervates Deposited as High Gas Barrier Thin Films. *Macromol. Rapid Commun.* **2017**, *38* (1), 1600594. https://doi.org/10.1002/marc.201600594.

(18) Renner, F. U.; Stierle, A.; Dosch, H.; Kolb, D. M.; Lee, T.-L.; Zegenhagen, J. Initial Corrosion Observed on the Atomic Scale. *Nature* **2006**, *439* (7077), 707–710. https://doi.org/10.1038/nature04465.

(19) Anticorrosive coatings: a review | SpringerLink https://link.springer.com/article/10.1007/s11998-008-9144-2 (accessed 2019 -10 -11).

(20) Hou, Y.; Lei, D.; Li, S.; Yang, W.; Li, C.-Q. Experimental Investigation on Corrosion Effect on Mechanical Properties of Buried Metal Pipes https://www.hindawi.com/journals/ijc/2016/5808372/ (accessed 2020 -02 -14). https://doi.org/10.1155/2016/5808372.

(21) Temperature Effects on Metals Strength https://tubingchina.com/Temperature-Effects-on-Metal-Strength.htm (accessed 2020 -02 -14).

(22) Hou, Y.; Lei, D.; Li, S.; Yang, W.; Li, C.-Q. Experimental Investigation on Corrosion Effect on Mechanical Properties of Buried Metal Pipes. *International Journal of Corrosion* **2016**, *2016*, 5808372. https://doi.org/10.1155/2016/5808372.

(23) Geary, W.; Hobbs, J. Catastrophic Failure of a Carbon Steel Storage Tank Due to Internal Corrosion. *Case Studies in Engineering Failure Analysis* **2013**, *1* (4), 257–264. https://doi.org/10.1016/j.csefa.2013.09.002.

(24) Renner, F. U.; Stierle, A.; Dosch, H.; Kolb, D. M.; Lee, T.-L.; Zegenhagen, J. Initial Corrosion Observed on the Atomic Scale. *Nature* **2006**, *439* (7077), 707–710. https://doi.org/10.1038/nature04465.

(25)   Stierle, A. Tracking Corrosion Cracking. *Science* **2008**, *321* (5887), 349–350.
         https://doi.org/10.1126/science.1160939.

(26)   Zarras, P.; Stenger-Smith, J. D. 1 - Corrosion Processes and Strategies for Prevention: An
         Introduction. In *Handbook of Smart Coatings for Materials Protection*; Makhlouf, A. S.
         H., Ed.; Woodhead Publishing, 2014; pp 3–28.
         https://doi.org/10.1533/9780857096883.1.3.

(27)   *Impedance Spectroscopy: Theory, Experiment, and Applications*, 2nd ed.; Barsoukov, E.,
         Macdonald, J. R., Eds.; Wiley-Interscience: Hoboken, N.J, 2005.

(28)   Marino, K. A.; Hinnemann, B.; Carter, E. A. Atomic-Scale Insight and Design Principles
         for Turbine Engine Thermal Barrier Coatings from Theory. *Proceedings of the National
         Academy of Sciences* **2011**, *108* (14), 5480–5487.
         https://doi.org/10.1073/pnas.1102426108.

(29)   6.8B: Band Theory of Metals and Insulators
         https://chem.libretexts.org/Bookshelves/Inorganic_Chemistry/Map%3A_Inorganic_Che
         mistry_(Housecroft)/06%3A_Structures_and_energetics_of_metallic_and_ionic_solids/6
         .08%3A_Bonding_in_Metals_and_Semicondoctors/6.8B%3A_Band_Theory_of_Metals
         _and_Insulators (accessed 2020 -03 -09).

(30)   Jimenez, M.; Duquesne, S.; Bourbigot, S. Intumescent Fire Protective Coating: Toward a
         Better Understanding of Their Mechanism of Action. *Thermochimica Acta* **2006**, *449* (1–
         2), 16–26. https://doi.org/10.1016/j.tca.2006.07.008.

(31)   Remy, L. Fatigue and Thermomechanical Fatigue at High Temperature. In *Encyclopedia
         of Materials: Science and Technology (Second Edition)*; Elsevier Science Ltd., 2001; pp
         2866–2877.

(32)   Xin, Q. 2 - Durability and Reliability in Diesel Engine System Design. In *Diesel Engine
         System Design*; Woodhead Publishing, 2013; pp 113–202.

(33)   Campbell, J. Properties of Castings. In *Complete Casting Handbook*; Elsevier, 2011; pp
         499–597. https://doi.org/10.1016/B978-1-85617-809-9.10009-X.

(34)   Bose, S. Chapter 6 - Oxidation- and Corrosion-Resistant Coatings. In *High Temperature
         Coatings*; Butterworth-Heinemann, 2018; pp 97–198.

(35)   Mandal, J.; Fu, Y.; Overvig, A. C.; Jia, M.; Sun, K.; Shi, N. N.; Zhou, H.; Xiao, X.; Yu,
         N.; Yang, Y. Hierarchically Porous Polymer Coatings for Highly Efficient Passive
         Daytime Radiative Cooling. *Science* **2018**, *362* (6412), 315–319.
         https://doi.org/10.1126/science.aat9513.

(36)   Bell, T. Here Are the Different Methods of Corrosion Prevention for Metals
         https://www.thebalance.com/corrosion-prevention-2340000 (accessed 2019 -04 -15).

(37)   Zarras, P.; Stenger-Smith, J. D. 1 - Corrosion Processes and Strategies for Prevention: An Introduction. In *Handbook of Smart Coatings for Materials Protection*; Makhlouf, A. S. H., Ed.; Woodhead Publishing, 2014; pp 3–28. https://doi.org/10.1533/9780857096883.1.3.

(38)   Angst, U. M. A Critical Review of the Science and Engineering of Cathodic Protection of Steel in Soil and Concrete. *Corrosion* **2019**, *75* (12), 1420–1433. https://doi.org/10.5006/3355.

(39)   McMahon, M. E.; Santucci, R. J.; Glover, C. F.; Kannan, B.; Walsh, Z. R.; Scully, J. R. A Review of Modern Assessment Methods for Metal and Metal-Oxide Based Primers for Substrate Corrosion Protection. *Front. Mater.* **2019**, *6*, 190. https://doi.org/10.3389/fmats.2019.00190.

(40)   Kozhukharov, S. V. Advanced Multifunctional Corrosion Protective Coating Systems for Light-Weight Aircraft Alloys—Actual Trends and Challenges. In *Thin Film Processes - Artifacts on Surface Phenomena and Technological Facets*; Thirumalai, J., Ed.; InTech, 2017. https://doi.org/10.5772/67237.

(41)   Andreeva, D. V.; Skorb, E. V. Multi-Layer Smart Coatings for Corrosion Protection of Aluminium Alloys and Steel. In *Handbook of Smart Coatings for Materials Protection*; Elsevier, 2014; pp 307–327. https://doi.org/10.1533/9780857096883.2.307.

(42)   Snihirova, D.; Lamaka, S. V.; Montemor, M. F. Smart Composite Coatings for Corrosion Protection of Aluminium Alloys in Aerospace Applications. In *Smart Composite Coatings and Membranes*; Elsevier, 2016; pp 85–121. https://doi.org/10.1016/B978-1-78242-283-9.00004-X.

(43)   Campestrini, P.; Terryn, H.; Vereecken, J.; Wit, J. H. W. de. Chromate Conversion Coating on Aluminum Alloys III. Corrosion Protection. *J. Electrochem. Soc.* **2004**, *151* (6), B370–B377. https://doi.org/10.1149/1.1736683.

(44)   Narayanan, S. Surface Pretreatment By Phosphate Conversion Coatings - A Review. *Rev. Adv, Mater. Sci.* **2005**, *9*, 130–177.

(45)   al-Swaidani, A. A. Modified Zinc Phosphate Coatings: A Promising Approach to Enhance the Anti-Corrosion Properties of Reinforcing Steel. *MOJCE* **2017**, *3* (5). https://doi.org/10.15406/mojce.2017.03.00083.

(46)   Ucaroglu, S.; Talinli, İ. Recovery and Safer Disposal of Phosphate Coating Sludge by Solidification/Stabilization. *Journal of Environmental Management* **2012**, *105*, 131–137. https://doi.org/10.1016/j.jenvman.2012.03.029.

(47)   Aneja, K.; Böhm, S.; Khanna, A.; Bohm, M. Graphene Based Anticorrosive Coatings for Cr (VI) Replacement. *Nanoscale* **2015**, *7*. https://doi.org/10.1039/C5NR04702A.

(48)   Kulinich, S.; S. Akhtar, A. On Conversion Coating Treatments to Replace Chromating for Al Alloys: Recent Developments and Possible Future Directions. *Russian Journal of Non-Ferrous Metals* **2012**, *53*, 176–203. https://doi.org/10.3103/S1067821212020071.

(49)   Qin, S.; Cubides, Y.; Lazar, S.; Ly, R.; Song, Y.; Gerringer, J.; Castaneda, H.; Grunlan, J. C. Ultrathin Transparent Nanobrick Wall Anticorrosion Coatings. *ACS Applied Nano Materials* **2018**, *1* (10), 5516–5523. https://doi.org/10.1021/acsanm.8b01032.

(50)   Clarke, D. R.; Levi, C. G. Materials Design for the Next Generation Thermal Barrier Coatings. *Annual Review of Materials Research* **2003**, *33* (1), 383–417. https://doi.org/10.1146/annurev.matsci.33.011403.113718.

(51)   Kumar, V.; Kandasubramanian, B. Processing and Design Methodologies for Advanced and Novel Thermal Barrier Coatings for Engineering Applications. *Particuology* **2016**, *27*, 1–28. https://doi.org/10.1016/j.partic.2016.01.007.

(52)   Staggs, J. Important Parameter Groups in Thermal Protection of Polymers. *Materials* **2015**, *8* (8), 4679–4698. https://doi.org/10.3390/ma8084679.

(53)   Li, G.-R.; Yang, G.-J. Chapter 7 - Structure Evolution of Multiscaled Thermal Barrier Coatings During Thermal Exposure. In *Advanced Nanomaterials and Coatings by Thermal Spray*; Micro and Nano Technologies; Elsevier, 2019; pp 221–255.

(54)   Dorfman, M. R. Chapter 22 - Thermal Spray Coatings. In *Handbook of Environmental Degradation of Materials*; William Andrew Publishing, 2018; pp 469–488.

(55)   Vaßen, R.; Jarligo, M. O.; Steinke, T.; Mack, D. E.; Stöver, D. Overview on Advanced Thermal Barrier Coatings. *Surface and Coatings Technology* **2010**, *205* (4), 938–942. https://doi.org/10.1016/j.surfcoat.2010.08.151.

(56)   Gok, M. G.; Goller, G. State of the Art of Gadolinium Zirconate Based Thermal Barrier Coatings: Design, Processing and Characterization. *Methods for Film Synthesis and Coating Procedures* **2019**. https://doi.org/10.5772/intechopen.85451.

(57)   Aabid, A.; Khan, S. A. Optimization of Heat Transfer on Thermal Barrier Coated Gas Turbine Blade. *IOP Conf. Ser.: Mater. Sci. Eng.* **2018**, *370*, 012022. https://doi.org/10.1088/1757-899X/370/1/012022.

(58)   Karaoglanli, A. C.; Ogawa, K.; Ozdemir, A. T. and I. Thermal Shock and Cycling Behavior of Thermal Barrier Coatings (TBCs) Used in Gas Turbines. *Progress in Gas Turbine Performance* **2013**. https://doi.org/10.5772/54412.

(59)   Wright, P. Mechanisms Governing the Performance of Thermal Barrier Coatings. *Current Opinion in Solid State and Materials Science* **1999**, *4* (3), 255–265. https://doi.org/10.1016/S1359-0286(99)00024-8.

(60)   Padture, N. P. Thermal Barrier Coatings for Gas-Turbine Engine Applications. *Science* **2002**, *296* (5566), 280–284. https://doi.org/10.1126/science.1068609.

(61)   Barroso, G.; Li, Q.; Bordia, R. K.; Motz, G. Polymeric and Ceramic Silicon-Based Coatings – a Review. *J. Mater. Chem. A* **2019**, *7* (5), 1936–1963. https://doi.org/10.1039/C8TA09054H.

(62)   Clarke, D. R.; Levi, C. G. Materials Design for the Next Generation Thermal Barrier Coatings. *Annual Review of Materials Research* **2003**, *33* (1), 383–417. https://doi.org/10.1146/annurev.matsci.33.011403.113718.

(63)   Staggs, J. E. J. A Theoretical Appraisal of the Effectiveness of Idealised Ablative Coatings for Steel Protection. *Fire Safety Journal* **2008**, *43* (8), 618–625. https://doi.org/10.1016/j.firesaf.2008.03.006.

(64)   Feih, S.; Mouritz, A. P.; Mathys, Z.; Gibson, A. G. Fire Structural Modeling of Polymer Composites with Passive Thermal Barrier. *Journal of Fire Sciences* **2010**, *28* (2), 141–160. https://doi.org/10.1177/0734904109340878.

(65)   Yew, M. C.; Ramli Sulong, N. H. Fire-Resistive Performance of Intumescent Flame-Retardant Coatings for Steel. *Materials & Design* **2012**, *34*, 719–724. https://doi.org/10.1016/j.matdes.2011.05.032.

(66)   Liu, L.; Yu, Z.-L.; Qu, J.; Huang, J. Spray-Coated Barrier Coating on Copper Based on Exfoliated Vermiculite Sheets. *Mater. Chem. Front.* **2021**, *5* (12), 4658–4663. https://doi.org/10.1039/D1QM00340B.

(67)   Luangtriratana, P.; Kandola, B. K.; Duquesne, S.; Bourbigot, S. Quantification of Thermal Barrier Efficiency of Intumescent Coatings on Glass Fibre-Reinforced Epoxy Composites. *Coatings* **2018**, *8* (10), 347. https://doi.org/10.3390/coatings8100347.

(68)   Griffin, G. J. The Modeling of Heat Transfer across Intumescent Polymer Coatings: *Journal of Fire Sciences* **2009**. https://doi.org/10.1177/0734904109346396.

(69)   Lucherini, A.; Maluk, C. Intumescent Coatings Used for the Fire-Safe Design of Steel Structures: A Review. *Journal of Constructional Steel Research* **2019**, *162*, 105712. https://doi.org/10.1016/j.jcsr.2019.105712.

(70)   Ustinov, A.; Zybina, O.; Tanklevsky, L.; Lebedev, V.; Andreev, A. Intumescent Coatings with Improved Properties for High-Rise Construction. *E3S Web Conf.* **2018**, *33*, 02039. https://doi.org/10.1051/e3sconf/20183302039.

(71)   Duquesne, S.; Magnet, S.; Jama, C.; Delobel, R. Intumescent Paints: Fire Protective Coatings for Metallic Substrates. *Surface and Coatings Technology* **2004**, *180–181*, 302–307. https://doi.org/10.1016/j.surfcoat.2003.10.075.

(72)   Dantas de Oliveira, A.; Augusto Gonçalves Beatrice, C. Polymer Nanocomposites with Different Types of Nanofiller. In *Nanocomposites - Recent Evolutions*; Sivasankaran, S., Ed.; IntechOpen, 2019. https://doi.org/10.5772/intechopen.81329.

(73)   Cui, Y.; Kumar, S.; Rao Kona, B.; van Houcke, D. Gas Barrier Properties of Polymer/Clay Nanocomposites. *RSC Adv.* **2015**, *5* (78), 63669–63690. https://doi.org/10.1039/C5RA10333A.

(74)   Ashraf, A.; Jani, N.; Farmer, F.; Lynch-Branzoi, J. K. Non-Destructive Investigation of Dispersion, Bonding, and Thermal Properties of Emerging Polymer Nanocomposites Using Close-Up Lens Assisted Infrared Thermography. *MRS Adv.* **2020**, *5* (14–15), 735–742. https://doi.org/10.1557/adv.2020.121.

(75)   Passador, F. R. 7 - Nanocomposites of Polymer Matrices and Lamellar Clays. 21.

(76)   Lazar, S.; Carosio, F.; Davesne, A.-L.; Jimenez, M.; Bourbigot, S.; Grunlan, J. Extreme Heat Shielding of Clay/Chitosan Nanobrick Wall on Flexible Foam. *ACS Applied Materials & Interfaces* **2018**, *10* (37), 31686–31696. https://doi.org/10.1021/acsami.8b10227.

(77)   Pielichowski, K.; Pielichowska, K. Chapter 11 - Polymer Nanocomposites. In *Handbook of Thermal Analysis and Calorimetry*; Elsevier Science B.V.; 2018; Vol. 6, pp 431–485.

(78)   Alexandre, M.; Dubois, P. Polymer-Layered Silicate Nanocomposites: Preparation, Properties and Uses of a New Class of Materials. *Materials Science and Engineering: R: Reports* **2000**, *28* (1–2), 1–63. https://doi.org/10.1016/S0927-796X(00)00012-7.

(79)   Mittal, V. Polymer Layered Silicate Nanocomposites: A Review. *Materials* **2009**, *2* (3), 992–1057. https://doi.org/10.3390/ma2030992.

(80)   Rawtani, D.; Agrawal, Y. K. Emerging Strategies and Applications of Layer-by-Layer Self-Assembly. *Nanobiomedicine* **2014**, *1*, 8. https://doi.org/10.5772/60009.

(81)   Hua, F.; Lvov, Y. M. Layer-by-Layer Assembly. In *The New Frontiers of Organic and Composite Nanotechnology*; Elsevier, 2008; pp 1–44. https://doi.org/10.1016/B978-008045052-0.50003-8.

(82)   Lyklema, J.; Deschênes, L. The First Step in Layer-by-Layer Deposition: Electrostatics and/or Non-Electrostatics? *Advances in Colloid and Interface Science* **2011**, *168* (1–2), 135–148. https://doi.org/10.1016/j.cis.2011.03.008.

(83)   Qin, S.; Song, Y.; Floto, M. E.; Grunlan, J. C. Combined High Stretchability and Gas Barrier in Hydrogen-Bonded Multilayer Nanobrick Wall Thin Films. *ACS Appl. Mater. Interfaces* **2017**, *9* (9), 7903–7907. https://doi.org/10.1021/acsami.7b00844.

(84)   Bergbreiter, D. E.; Liao, K.-S. Covalent Layer-by-Layer Assembly—an Effective, Forgiving Way to Construct Functional Robust Ultrathin Films and Nanocomposites. *Soft Matter* **2009**, *5* (1), 23–28. https://doi.org/10.1039/B810852H.

(85)   Borges, J.; Mano, J. F. Molecular Interactions Driving the Layer-by-Layer Assembly of Multilayers. *Chem. Rev.* **2014**, *114* (18), 8883–8942. https://doi.org/10.1021/cr400531v.

(86)   Picart, C.; Mutterer, J.; Richert, L.; Luo, Y.; Prestwich, G. D.; Schaaf, P.; Voegel, J.-C.; Lavalle, P. Molecular Basis for the Explanation of the Exponential Growth of Polyelectrolyte Multilayers. *Proceedings of the National Academy of Sciences* **2002**, *99* (20), 12531–12535. https://doi.org/10.1073/pnas.202486099.

(87)   Richardson, J. J.; Björnmalm, M.; Caruso, F. Technology-Driven Layer-by-Layer Assembly of Nanofilms. *Science* **2015**, *348* (6233), aaa2491. https://doi.org/10.1126/science.aaa2491.

(88)   Hagen, D. A.; Song, Y.; Saucier, L.; Milhorn, A.; Stevens, B.; Grunlan, J. C. Balancing Polyelectrolyte Diffusion and Clay Deposition for High Gas Barrier. *Green Materials* **2016**, *4* (3), 98–103. https://doi.org/10.1680/jgrma.16.00012.

(89)   Mendelsohn, J. D.; Barrett, C. J.; Chan, V. V.; Pal, A. J.; Mayes, A. M.; Rubner, M. F. Fabrication of Microporous Thin Films from Polyelectrolyte Multilayers. *Langmuir* **2000**, *16* (11), 5017–5023. https://doi.org/10.1021/la000075g.

(90)   Fu, J.; Fares, H. M.; Schlenoff, J. B. Ion-Pairing Strength in Polyelectrolyte Complexes. *Macromolecules* **2017**, *50* (3), 1066–1074. https://doi.org/10.1021/acs.macromol.6b02445.

(91)   Sui, Z.; Salloum, D.; Schlenoff, J. B. Effect of Molecular Weight on the Construction of Polyelectrolyte Multilayers: Stripping versus Sticking. *Langmuir* **2003**, *19* (6), 2491–2495. https://doi.org/10.1021/la026531d.

(92)   Zhang, H.; Wang, D.; Wang, Z.; Zhang, X. Hydrogen Bonded Layer-by-Layer Assembly of Poly(2-Vinylpyridine) and Poly(Acrylic Acid): Influence of Molecular Weight on the Formation of Microporous Film by Post-Base Treatment. *European Polymer Journal* **2007**, *43* (7), 2784–2791. https://doi.org/10.1016/j.eurpolymj.2007.04.010.

(93)   Garg, A.; Heflin, J. R.; Gibson, H. W.; Davis, R. M. Study of Film Structure and Adsorption Kinetics of Polyelectrolyte Multilayer Films: Effect of PH and Polymer Concentration. *Langmuir* **2008**, *24* (19), 10887–10894. https://doi.org/10.1021/la8005053.

(94)   Hagen, D. A.; Foster, B.; Stevens, B.; Grunlan, J. C. Shift-Time Polyelectrolyte Multilayer Assembly: Fast Film Growth and High Gas Barrier with Fewer Layers by Adjusting Deposition Time. *ACS Macro Letters* **2014**, *3* (7), 663–666. https://doi.org/10.1021/mz500276r.

(95)   Tan, H. L.; McMurdo, M. J.; Pan, G.; Van Patten, P. G. Temperature Dependence of Polyelectrolyte Multilayer Assembly. *Langmuir* **2003**, *19* (22), 9311–9314. https://doi.org/10.1021/la035094f.

(96)   McAloney, R. A.; Sinyor, M.; Dudnik, V.; Goh, M. C. Atomic Force Microscopy Studies of Salt Effects on Polyelectrolyte Multilayer Film Morphology. *Langmuir* **2001**, *17* (21), 6655–6663. https://doi.org/10.1021/la010136q.

(97)   Mermut, O.; Barrett, C. J. Effects of Charge Density and Counterions on the Assembly of Polyelectrolyte Multilayers. *J. Phys. Chem. B* **2003**, *107* (11), 2525–2530. https://doi.org/10.1021/jp027278t.

(98)   Zhang, X.; Xu, Y.; Zhang, X.; Wu, H.; Shen, J.; Chen, R.; Xiong, Y.; Li, J.; Guo, S. Progress on the Layer-by-Layer Assembly of Multilayered Polymer Composites: Strategy, Structural Control and Applications. *Progress in Polymer Science* **2019**, *89*, 76–107. https://doi.org/10.1016/j.progpolymsci.2018.10.002.

(99)   Borges, J.; Mano, J. F. Molecular Interactions Driving the Layer-by-Layer Assembly of Multilayers. *Chem. Rev.* **2014**, *114* (18), 8883–8942. https://doi.org/10.1021/cr400531v.

(100)   Stevens, B. E.; Odenborg, P. K.; Priolo, M. A.; Grunlan, J. C. Hydrophobically Modified Polyelectrolyte for Improved Oxygen Barrier in Nanobrick Wall Multilayer Thin Films. *J. Polym. Sci. Part B: Polym. Phys.* **2014**, *52* (17), 1153–1156. https://doi.org/10.1002/polb.23543.

(101)   Hagen, D. A.; Box, C.; Greenlee, S.; Xiang, F.; Regev, O.; Grunlan, J. C. High Gas Barrier Imparted by Similarly Charged Multilayers in Nanobrick Wall Thin Films. *RSC Adv.* **2014**, *4* (35), 18354–18359. https://doi.org/10.1039/C4RA01621A.

(102)   Heidarian, M.; Shishesaz, M. R.; Kassiriha, S. M.; Nematollahi, M. Characterization of Structure and Corrosion Resistivity of Polyurethane/Organoclay Nanocomposite Coatings Prepared through an Ultrasonication Assisted Process. *Progress in Organic Coatings* **2010**, *68* (3), 180–188. https://doi.org/10.1016/j.porgcoat.2010.02.006.

(103)   Priolo, M. A.; Holder, K. M.; Gamboa, D.; Grunlan, J. C. Influence of Clay Concentration on the Gas Barrier of Clay–Polymer Nanobrick Wall Thin Film Assemblies. *Langmuir* **2011**, *27* (19), 12106–12114. https://doi.org/10.1021/la201584r.

(104)   Laufer, G.; Kirkland, C.; Cain, A. A.; Grunlan, J. C. Clay–Chitosan Nanobrick Walls: Completely Renewable Gas Barrier and Flame-Retardant Nanocoatings. *ACS Appl. Mater. Interfaces* **2012**, *4* (3), 1643–1649. https://doi.org/10.1021/am2017915.

(105)   Priolo, M. A.; Gamboa, D.; Grunlan, J. C. Transparent Clay−Polymer Nano Brick Wall Assemblies with Tailorable Oxygen Barrier. *ACS Appl. Mater. Interfaces* **2010**, *2* (1), 312–320. https://doi.org/10.1021/am900820k.

(106)   Priolo, M. A.; Holder, K. M.; Greenlee, S. M.; Grunlan, J. C. Transparency, Gas Barrier, and Moisture Resistance of Large-Aspect-Ratio Vermiculite Nanobrick Wall Thin Films. *ACS Appl. Mater. Interfaces* **2012**, *4* (10), 5529–5533. https://doi.org/10.1021/am3014289.

(107)   Hiemenz, P. C.; Lodge, T. *Polymer Chemistry*, 2nd ed.; CRC Press: Boca Raton, 2007.

(108)   Tong, W.; Gao, C.; Möhwald, H. Manipulating the Properties of Polyelectrolyte Microcapsules by Glutaraldehyde Cross-Linking. *Chem. Mater.* **2005**, *17* (18), 4610–4616. https://doi.org/10.1021/cm0507516.

(109) Yang, Y.-H.; Bolling, L.; Haile, M.; C. Grunlan, J. Improving Oxygen Barrier and Reducing Moisture Sensitivity of Weak Polyelectrolyte Multilayer Thin Films with Crosslinking. *RSC Advances* **2012**, *2* (32), 12355–12363. https://doi.org/10.1039/C2RA21845C.

(110) Ducker, R. E.; Montague, M. T.; Leggett, G. J. A Comparative Investigation of Methods for Protein Immobilization on Self-Assembled Monolayers Using Glutaraldehyde, Carbodiimide, and Anhydride Reagents. *Biointerphases* **2008**, *3* (3), 59–65. https://doi.org/10.1116/1.2976451.

(111) Lehaf, A. M.; Moussallem, M. D.; Schlenoff, J. B. Correlating the Compliance and Permeability of Photo-Cross-Linked Polyelectrolyte Multilayers. *Langmuir* **2011**, *27* (8), 4756–4763. https://doi.org/10.1021/la200229h.

(112) Yang, S. Y.; Rubner, M. F. Micropatterning of Polymer Thin Films with PH-Sensitive and Cross-Linkable Hydrogen-Bonded Polyelectrolyte Multilayers. *J. Am. Chem. Soc.* **2002**, *124* (10), 2100–2101. https://doi.org/10.1021/ja017681y.

(113) Vanherck, K.; Koeckelberghs, G.; Vankelecom, I. F. J. Crosslinking Polyimides for Membrane Applications: A Review. *Progress in Polymer Science* **2013**, *38* (6), 874–896. https://doi.org/10.1016/j.progpolymsci.2012.11.001.

(114) Maitra, J.; Shukla. Hydrogels, Cross Linking, Gel, Polymer. *American Journal of Polymer Science* **2014**, 7.

(115) Chen, J.; Garcia, E. S.; Zimmerman, S. C. Intramolecularly Cross-Linked Polymers: From Structure to Function with Applications as Artificial Antibodies and Artificial Enzymes. *Acc. Chem. Res.* **2020**, *53* (6), 1244–1256. https://doi.org/10.1021/acs.accounts.0c00178.

(116) Lazar, S.; Garcia-Valdez, O.; Kennedy, E.; Champagne, P.; Cunningham, M.; Grunlan, J. Crosslinkable-Chitosan-Enabled Moisture-Resistant Multilayer Gas Barrier Thin Film. *Macromol. Rapid Commun.* **2019**, *40* (6), 1800853. https://doi.org/10.1002/marc.201800853.

(117) Luckachan, G. E.; Mittal, V. Anti-Corrosion Behavior of Layer by Layer Coatings of Cross-Linked Chitosan and Poly(Vinyl Butyral) on Carbon Steel. *Cellulose* **2015**, *22* (5), 3275–3290. https://doi.org/10.1007/s10570-015-0711-2.

(118) Arkles, B. Hydrophobicity, Hydrophilicity and Silanes. *Paint and Coatings Industry* **2006**, *22*, 114.

(119) Howarter, J. A.; Youngblood, J. P. Optimization of Silica Silanization by 3-Aminopropyltriethoxysilane. *Langmuir* **2006**, *22* (26), 11142–11147. https://doi.org/10.1021/la061240g.

(120) Parhizkar, N.; Ramezanzadeh, B.; Shahrabi, T. Corrosion Protection and Adhesion Properties of the Epoxy Coating Applied on the Steel Substrate Pre-Treated by a Sol-Gel

Based Silane Coating Filled with Amino and Isocyanate Silane Functionalized Graphene Oxide Nanosheets. *Applied Surface Science* **2018**, *439*, 45–59. https://doi.org/10.1016/j.apsusc.2017.12.240.

(121) Lee, J. H.; Kim, S. H. Fabrication of Silane-Grafted Graphene Oxide and Its Effect on the Structural, Thermal, Mechanical, and Hysteretic Behavior of Polyurethane. *Sci Rep* **2020**, *10* (1), 19152. https://doi.org/10.1038/s41598-020-76153-8.

(122) Xu, L.; Wang, L.; Shen, Y.; Ding, Y.; Cai, Z. Preparation of Hexadecyltrimethoxysilane-Modified Silica Nanocomposite Hydrosol and Superhydrophobic Cotton Coating. *Fibers Polym* **2015**, *16* (5), 1082–1091. https://doi.org/10.1007/s12221-015-1082-x.

(123) P. Singh, M.; K. Keister, H.; Matisons, J.; Pan, Y.; Zazyczny, J.; Arkles, B. Dipodal Silanes: Important Tool for Surface Modification to Improve Durability. *MRS Online Proceeding Library* **2014**, *1648*. https://doi.org/10.1557/opl.2014.257.

(124) He, Z.; Zhang, Z.; Bi, S.; Chen, J.; Li, D. Conjugated Polymer Controlled Morphology and Charge Transport of Small-Molecule Organic Semiconductors. *Sci Rep* **2020**, *10* (1), 4344. https://doi.org/10.1038/s41598-020-61282-x.

(125) Guin, T.; Krecker, M.; Milhorn, A.; Hagen, D. A.; Stevens, B.; Grunlan, J. C. Exceptional Flame Resistance and Gas Barrier with Thick Multilayer Nanobrick Wall Thin Films. *Advanced Materials Interfaces* **2015**, *2* (11), 1500214. https://doi.org/10.1002/admi.201500214.

(126) Hutton-Prager, B.; Khan, M. M.; Gentry, C.; Knight, C. B.; Al-Abri, A. K. A. Thermal Barrier Enhancement of Calcium Carbonate Coatings with Nanoparticle Additives, and Their Effect on Hydrophobicity. *Cellulose* **2019**, *26* (8), 4865–4880. https://doi.org/10.1007/s10570-019-02426-9.

(127) Tang, K.; Besseling, N. A. M. Formation of Polyelectrolyte Multilayers: Ionic Strengths and Growth Regimes. *Soft Matter* **2016**, *12* (4), 1032–1040. https://doi.org/10.1039/C5SM02118A.

(128) Stevens, D. L.; Gamage, G. A.; Ren, Z.; Grunlan, J. C. Salt Doping to Improve Thermoelectric Power Factor of Organic Nanocomposite Thin Films. *RSC Adv.* **2020**, *10* (20), 11800–11807. https://doi.org/10.1039/D0RA00763C.

(129) McPherson, A.; Nguyen, C.; Cudney, R.; Larson, S. B. The Role of Small Molecule Additives and Chemical Modification in Protein Crystallization. *Crystal Growth & Design* **2011**, *11* (5), 1469–1474. https://doi.org/10.1021/cg101308r.

(130) Lazar, S.; Eberle, B.; Bellevergue, E.; Grunlan, J. Amine Salt Thickening of Intumescent Multilayer Flame Retardant Treatment. *Ind. Eng. Chem. Res.* **2020**, *59* (7), 2689–2695. https://doi.org/10.1021/acs.iecr.9b06359.

(131) Manion, J. G.; Gao, D.; Brodersen, P. M.; Seferos, D. S. Insulating Polymer Additives in Small Molecule and Polymer Photovoltaics: How They Are Tolerated and Their Use as

Potential Interlayers. *J. Mater. Chem. C* **2017**, *5* (13), 3315–3322. https://doi.org/10.1039/C7TC00525C.

(132) Rumer, J. W.; Ashraf, R. S.; Eisenmenger, N. D.; Huang, Z.; Meager, I.; Nielsen, C. B.; Schroeder, B. C.; Chabinyc, M. L.; McCulloch, I. Dual Function Additives: A Small Molecule Crosslinker for Enhanced Efficiency and Stability in Organic Solar Cells. *Adv. Energy Mater.* **2015**, *5* (9), 1401426. https://doi.org/10.1002/aenm.201401426.

(133) Schlenoff, J. B.; Ly, H.; Li, M. Charge and Mass Balance in Polyelectrolyte Multilayers. *J. Am. Chem. Soc.* **1998**, *120* (30), 7626–7634. https://doi.org/10.1021/ja980350+.

(134) Tertre, E.; Delville, A.; Prêt, D.; Hubert, F.; Ferrage, E. Cation Diffusion in the Interlayer Space of Swelling Clay Minerals – A Combined Macroscopic and Microscopic Study. *Geochimica et Cosmochimica Acta* **2015**, *149*, 251–267. https://doi.org/10.1016/j.gca.2014.10.011.

(135) Priolo, M. A.; Holder, K. M.; Greenlee, S. M.; Grunlan, J. C. Transparency, Gas Barrier, and Moisture Resistance of Large-Aspect-Ratio Vermiculite Nanobrick Wall Thin Films. *ACS Appl. Mater. Interfaces* **2012**, *4* (10), 5529–5533. https://doi.org/10.1021/am3014289.

(136) Guin, T.; Krecker, M.; Milhorn, A.; Hagen, D. A.; Stevens, B.; Grunlan, J. C. Exceptional Flame Resistance and Gas Barrier with Thick Multilayer Nanobrick Wall Thin Films. *Advanced Materials Interfaces* **2015**, *2* (11), 1500214. https://doi.org/10.1002/admi.201500214.

(137) Tang, L.; Hao, Q.; Ge, Y.; Li, Y. Flame Retardancy Comparison of Type I and Type II Ammonium Polyphosphate Respective in Combination with 1,3,5-Tris(2-Hydroxyethyl)Cyanurate in Polypropylene. *Asian J. Chem.* **2013**, *25* (16), 8879–8882. https://doi.org/10.14233/ajchem.2013.14879.

(138) Liu, X.; Qin, S.; Li, H.; Sun, J.; Gu, X.; Zhang, S.; Grunlan, J. C. Combination Intumescent and Kaolin-Filled Multilayer Nanocoatings That Reduce Polyurethane Flammability. *Macromol. Mater. Eng.* **2019**, *304* (2), 1800531. https://doi.org/10.1002/mame.201800531.

(139) Laufer, G.; Kirkland, C.; Morgan, A. B.; Grunlan, J. C. Intumescent Multilayer Nanocoating, Made with Renewable Polyelectrolytes, for Flame-Retardant Cotton. *Biomacromolecules* **2012**, *13* (9), 2843–2848. https://doi.org/10.1021/bm300873b.

(140) Kolibaba, T. J.; Shih, C.-C.; Lazar, S.; Tai, B. L.; Grunlan, J. C. Self-Extinguishing Additive Manufacturing Filament from a Unique Combination of Polylactic Acid and a Polyelectrolyte Complex. **2020**, 5.

(141) Gu, J.; Zhang, G.; Dong, S.; Zhang, Q.; Kong, J. Study on Preparation and Fire-Retardant Mechanism Analysis of Intumescent Flame-Retardant Coatings. *Surface and Coatings Technology* **2007**, *201* (18), 7835–7841. https://doi.org/10.1016/j.surfcoat.2007.03.020.

(142) Qian, Y.; Li, Y.; Jungwirth, S.; Seely, N.; Fang, Y.; Shi, X. The Application of Anti-Corrosion Coating for Preserving the Value of Equipment Asset in Chloride-Laden Environments: A Review. *Int. J. Electrochem. Sci.* **2015**, *10*, 26.

(143) Sinha Ray, S.; Okamoto, M. Polymer/Layered Silicate Nanocomposites: A Review from Preparation to Processing. *Progress in Polymer Science* **2003**, *28* (11), 1539–1641. https://doi.org/10.1016/j.progpolymsci.2003.08.002.

(144) Suarez-Martinez, P. C.; Robinson, J.; An, H.; Nahas, R. C.; Cinoman, D.; Lutkenhaus, J. L. Polymer-Clay Nanocomposite Coatings as Efficient, Environment-Friendly Surface Pretreatments for Aluminum Alloy 2024-T3. *Electrochimica Acta* **2018**, *260*, 73–81. https://doi.org/10.1016/j.electacta.2017.11.046.

(145) Yeh, J.-M.; Liou, S.-J.; Lai, C.-Y.; Wu, P.-C.; Tsai, T.-Y. Enhancement of Corrosion Protection Effect in Polyaniline via the Formation of Polyaniline−Clay Nanocomposite Materials. *Chem. Mater.* **2001**, *13* (3), 1131–1136. https://doi.org/10.1021/cm000938r.

(146) Qin, S.; Cubides, Y.; Lazar, S.; Ly, R.; Song, Y.; Gerringer, J.; Castaneda, H.; Grunlan, J. C. Ultrathin Transparent Nanobrick Wall Anticorrosion Coatings. *ACS Applied Nano Materials* **2018**, *1* (10), 5516–5523. https://doi.org/10.1021/acsanm.8b01032.

(147) Percival, S. J.; Melia, M. A.; Alexander, C. L.; Nelson, D. W.; Schindelholz, E. J.; Spoerke, E. D. Nanoscale Thin Film Corrosion Barriers Enabled by Multilayer Polymer Clay Nanocomposites. *Surface and Coatings Technology* **2020**, *383*, 125228. https://doi.org/10.1016/j.surfcoat.2019.125228.

(148) Xiang, F.; Tzeng, P.; Sawyer, J. S.; Regev, O.; Grunlan, J. C. Improving the Gas Barrier Property of Clay–Polymer Multilayer Thin Films Using Shorter Deposition Times. *ACS Appl. Mater. Interfaces* **2014**, *6* (9), 6040–6048. https://doi.org/10.1021/am403445z.

(149) Lindén, J. B.; Larsson, M.; Kaur, S.; Nosrati, A.; Nydén, M. Glutaraldehyde-Crosslinking for Improved Copper Absorption Selectivity and Chemical Stability of Polyethyleneimine Coatings. *J. Appl. Polym. Sci.* **2016**, *133* (37). https://doi.org/10.1002/app.43954.

(150) Liu, Y.; Cao, H.-J.; Yu, Y.; Chen, S. Corrosion Protection of Silane Coatings Modified by Carbon Nanotubes on Stainless Steel. *International Journal of Electrochemical Science* **2015**, *10*, 3497–3509.

(151) Jang, W. S.; Grunlan, J. C. Robotic Dipping System for Layer-by-Layer Assembly of Multi-Functional Thin Films. *Rev. Sci. Instr.* **2005**, *76*, 103904.

(152) Hagen, D. A.; Saucier, L.; Grunlan, J. C. Controlling Effective Aspect Ratio and Packing of Clay with PH for Improved Gas Barrier in Nanobrick Wall Thin Films. *ACS Appl. Mater. Interfaces* **2014**, *6* (24), 22914–22919. https://doi.org/10.1021/am507603z.

(153) Karabanova, L.; Sergeeva, L.; Boiteux, G. Filler Effect on Formation and Properties of Reinforced Interpenetrating Polymer Networks. *Composite Interfaces* **2001**, *8* (3–4), 207–219. https://doi.org/10.1163/15685540152594677.

(154) Ruijgrok, J. M.; De Wijn, J. R.; Boon, M. E. Optimizing Glutaraldehyde Crosslinking of Collagen: Effects of Time, Temperature and Concentration as Measured by Shrinkage Temperature. *J Mater Sci: Mater Med* **1994**, *5* (2), 80–87. https://doi.org/10.1007/BF00121695.

(155) Yuan, X.; Wolf, N.; Mayer, D.; Offenha?usser, A.; Wo?rdenweber, R. Vapor-Phase Deposition and Electronic Characterization of 3-Aminopropyltriethoxysilane Self-Assembled Monolayers on Silicon Dioxide. *Langmuir* **2019**, *35* (25), 8183–8190. https://doi.org/10.1021/acs.langmuir.8b03832.

(156) Zhang, F.; Sautter, K.; Larsen, A. M.; Findley, D. A.; Davis, R. C.; Samha, H.; Linford, M. R. Chemical Vapor Deposition of Three Aminosilanes on Silicon Dioxide: Surface Characterization, Stability, Effects of Silane Concentration, and Cyanine Dye Adsorption. *Langmuir* **2010**, *26* (18), 14648–14654. https://doi.org/10.1021/la102447y.

(157) de Miranda, M. I. G.; Tomedi, C.; Bica, C. I. D.; Samios, D. A d.s.c. Kinetic Study on the Effect of Filler Concentration on Crosslinking of Diglycidylether of Bisphenol-A with 4,4′-Diaminodiphenylmethane. *Polymer* **1997**, *38* (5), 1017–1020. https://doi.org/10.1016/S0032-3861(96)00601-5.

(158) Vermeirssen, E. L. M.; Dietschweiler, C.; Werner, I.; Burkhardt, M. Corrosion Protection Products as a Source of Bisphenol A and Toxicity to the Aquatic Environment. *Water Research* **2017**, *123*, 586–593. https://doi.org/10.1016/j.watres.2017.07.006.

(159) Suvorov, S. A.; Skurikhin, V. V. VERMICULITE — A PROMISING MATERIAL FOR HIGH-TEMPERATURE HEAT INSULATORS. *Refractories and Industrial Ceramics* **2003**, *44* (3), 186–193. https://doi.org/10.1023/A:1026312619843.

(160) Michel, M.; Toniazzo, V.; Ruch, D.; Ball, V. Deposition Mechanisms in Layer-by-Layer or Step-by-Step Deposition Methods: From Elastic and Impermeable Films to Soft Membranes with Ion Exchange Properties. *ISRN Materials Science* **2012**, *2012*, 1–13. https://doi.org/10.5402/2012/701695.

(161) Dong, L. L.; Leung, C. W.; Cheung, C. S. Heat Transfer Characteristics of Premixed Butane/Air Flame Jet Impinging on an Inclined Flat Surface. *Heat and Mass Transfer* **2002**, *39* (1), 19–26. https://doi.org/10.1007/s00231-001-0288-1.

(162) Zhao, Z.; Wong, T. T.; Leung, C. W. Impinging Premixed Butane/Air Circular Laminar Flame Jet—Influence of Impingement Plate on Heat Transfer Characteristics. *International Journal of Heat and Mass Transfer* **2004**, *47* (23), 5021–5031. https://doi.org/10.1016/j.ijheatmasstransfer.2004.06.022.

(163) Milson, A.; Chigier, N. A. Studies of Methane and Methane - Air Flames Impinging on a Cold Plates. *Combustion and Flame* **1973**, *21* (3), 295–305.

(164) Holder, K. M.; Huff, M. E.; Cosio, M. N.; Grunlan, J. C. Intumescing Multilayer Thin Film Deposited on Clay-Based Nanobrick Wall to Produce Self-Extinguishing Flame Retardant Polyurethane. *J Mater Sci* **2015**, *50* (6), 2451–2458. https://doi.org/10.1007/s10853-014-8800-4.

(165) Mohammadi, M.; Salehi, A.; Branch, R. J.; Cygan, L. J.; Besirli, C. G.; Larson, R. G. Growth Kinetics in Layer-by-Layer Assemblies of Organic Nanoparticles and Polyelectrolytes. *ChemPhysChem* **2017**, *18* (1), 128–141. https://doi.org/10.1002/cphc.201600789.

(166) Ali, S. W.; Rajendran, S.; Joshi, M. Effect of Process Parameters on Layer-by-Layer Self-Assembly of Polyelectrolytes on Cotton Substrate. *Polymers and Polymer Composites* **2010**, *18* (5), 237–249. https://doi.org/10.1177/096739111001800501.

(167) Buchman, Y. K.; Lellouche, E.; Zigdon, S.; Bechor, M.; Michaeli, S.; Lellouche, J.-P. Silica Nanoparticles and Polyethyleneimine (PEI)-Mediated Functionalization: A New Method of PEI Covalent Attachment for SiRNA Delivery Applications. *Bioconjugate Chem.* **2013**, *24* (12), 2076–2087. https://doi.org/10.1021/bc4004316.

(168) Okada, T.; Ishige, R.; Ando, S. Analysis of Thermal Radiation Properties of Polyimide and Polymeric Materials Based on ATR-IR Spectroscopy. *J. Photopol. Sci. Technol.* **2016**, *29* (2), 251–254. https://doi.org/10.2494/photopolymer.29.251.

(169) Mills, A. F.; Coimbra, C. F. M. *Heat Transfer*, 3rd ed.; Temporal Publishing: San Diego, CA, 2016.

(170) Martinez, A. *Nanocomposites and Polymers with Analytical Methods*; Magnum Publishing LLC, 2016.

(171) Chen, J.; Zhou, Y.; Nan, Q.; Sun, Y.; Ye, X.; Wang, Z. Synthesis, Characterization and Infrared Emissivity Study of Polyurethane/TiO2 Nanocomposites. *Applied Surface Science* **2007**, *253* (23), 9154–9158. https://doi.org/10.1016/j.apsusc.2007.05.046.

(172) Song, Y.; Hagen, D. A.; Qin, S.; Holder, K. M.; Falke, K.; Grunlan, J. C. Edge Charge Neutralization of Clay for Improved Oxygen Gas Barrier in Multilayer Nanobrick Wall Thin Films. *ACS Appl. Mater. Interfaces* **2016**, *8* (50), 34784–34790. https://doi.org/10.1021/acsami.6b12937.

(173) Suvorov, S. A.; Skurikhin, V. V. VERMICULITE — A PROMISING MATERIAL FOR HIGH-TEMPERATURE HEAT INSULATORS. 8.

(174) Long, C. T.; Wang, R.; Shoalmire, C.; Antao, D. S.; Shamberger, P. J.; Grunlan, J. C. Efficient Heat Shielding of Steel with Multilayer Nanocomposite Thin Film. *ACS Appl. Mater. Interfaces* **2021**, *13* (16), 19369–19376. https://doi.org/10.1021/acsami.1c03781.

(175) Velencoso, M. M.; Battig, A.; Markwart, J. C.; Schartel, B.; Wurm, F. R. Molecular Firefighting—How Modern Phosphorus Chemistry Can Help Solve the Challenge of

Flame Retardancy. *Angew. Chem. Int. Ed.* **2018**, *57* (33), 10450–10467. https://doi.org/10.1002/anie.201711735.

(176)   Mariappan, T. Recent Developments of Intumescent Fire Protection Coatings for Structural Steel: A Review. *Journal of Fire Sciences* **2016**, *34* (2), 120–163. https://doi.org/10.1177/0734904115626720.

(177)   Myers, R. E.; Dickens, E. D.; Licursi, E.; Evans, R. E. Ammonium Pentaborate: An Intumescent Flame Retardant for Thermoplastic Polyurethanes. *Journal of Fire Sciences* **1985**, *3* (6), 432–449. https://doi.org/10.1177/073490418500300604.

(178)   Dogan, M.; Dogan, S. D.; Savas, L. A.; Ozcelik, G.; Tayfun, U. Flame Retardant Effect of Boron Compounds in Polymeric Materials. *Composites Part B: Engineering* **2021**, *222*, 109088. https://doi.org/10.1016/j.compositesb.2021.109088.

(179)   Levchik, S. V.; Levchik, G. F.; Balabanovich, A. I.; Camino, G.; Costa, L. Mechanistic Study of Combustion Performance and Thermal Decomposition Behaviour of Nylon 6 with Added Halogen-Free Fire Retardants. *Polymer Degradation and Stability* **1996**, *54* (2–3), 217–222. https://doi.org/10.1016/S0141-3910(96)00046-8.

(180)   Dong, Z.; Yang, H.; Liu, Z.; Chen, P.; Chen, Y.; Wang, X.; Chen, H. Effect of Boron-Based Additives on Char Agglomeration and Boron Doped Carbon Microspheres Structure from Lignin Pyrolysis. *Fuel* **2021**, *303*, 121237. https://doi.org/10.1016/j.fuel.2021.121237.

(181)   Sun, F.; Fan, X.; Zhang, T.; Jiang, P.; Yang, J. Numerical Analysis of the Influence of Pore Microstructure on Thermal Conductivity and Young's Modulus of Thermal Barrier Coating. *Ceramics International* **2020**, *46* (15), 24326–24332. https://doi.org/10.1016/j.ceramint.2020.06.214.

(182)   Zhao, Y.; Wen, J.; Peyraut, F.; Planche, M.-P.; Misra, S.; Lenoir, B.; Ilavsky, J.; Liao, H.; Montavon, G. Porous Architecture and Thermal Properties of Thermal Barrier Coatings Deposited by Suspension Plasma Spray. *Surface and Coatings Technology* **2020**, *386*, 125462. https://doi.org/10.1016/j.surfcoat.2020.125462.

(183)   Huang, C.; Qian, X.; Yang, R. Thermal Conductivity of Polymers and Polymer Nanocomposites. *Materials Science and Engineering: R: Reports* **2018**, *132*, 1–22. https://doi.org/10.1016/j.mser.2018.06.002.

(184)   Machrafi, H.; Lebon, G. Size and Porosity Effects on Thermal Conductivity of Nanoporous Material with an Extension to Nanoporous Particles Embedded in a Host Matrix. *Physics Letters A* **2015**, *379* (12–13), 968–973. https://doi.org/10.1016/j.physleta.2015.01.027.

(185)   Yan, Y.; King, S. C.; Li, M.; Galy, T.; Marszewski, M.; Kang, J. S.; Pilon, L.; Hu, Y.; Tolbert, S. H. Exploring the Effect of Porous Structure on Thermal Conductivity in Templated Mesoporous Silica Films. *J. Phys. Chem. C* **2019**, *123* (35), 21721–21730. https://doi.org/10.1021/acs.jpcc.9b03767.

(186)   Smith, D. S.; Alzina, A.; Bourret, J.; Nait-Ali, B.; Pennec, F.; Tessier-Doyen, N.; Otsu, K.; Matsubara, H.; Elser, P.; Gonzenbach, U. T. Thermal Conductivity of Porous Materials. *J. Mater. Res.* **2013**, *28* (17), 2260–2272. https://doi.org/10.1557/jmr.2013.179.

(187)   Smith, M. W.; Dallmeyer, I.; Johnson, T. J.; Brauer, C. S.; McEwen, J.-S.; Espinal, J. F.; Garcia-Perez, M. Structural Analysis of Char by Raman Spectroscopy: Improving Band Assignments through Computational Calculations from First Principles. *Carbon* **2016**, *100*, 678–692. https://doi.org/10.1016/j.carbon.2016.01.031.

(188)   Gouadec, G.; Colomban, P. Raman Spectroscopy of Nanomaterials: How Spectra Relate to Disorder, Particle Size and Mechanical Properties. *Progress in Crystal Growth and Characterization of Materials* **2007**, *53* (1), 1–56. https://doi.org/10.1016/j.pcrysgrow.2007.01.001.

(189)   Pan, D.; Wang, S.; Zhao, B.; Wu, M.; Zhang, H.; Wang, Y.; Jiao, Z. Li Storage Properties of Disordered Graphene Nanosheets. *Chem. Mater.* **2009**, *21* (14), 3136–3142. https://doi.org/10.1021/cm900395k.

(190)   Mu, X.; Wu, X.; Zhang, T.; Go, D. B.; Luo, T. Thermal Transport in Graphene Oxide – From Ballistic Extreme to Amorphous Limit. *Sci Rep* **2015**, *4* (1), 3909. https://doi.org/10.1038/srep03909.

(191)   Antidormi, A.; Colombo, L.; Roche, S. Thermal Transport in Amorphous Graphene with Varying Structural Quality. *2D Mater.* **2020**, *8* (1), 015028. https://doi.org/10.1088/2053-1583/abc7f8.

(192)   Zhao, G.; Hu, P.; Zhou, S.; Chen, G.; An, Y.; Cheng, Y.; An, J.; Zhang, X.; Han, W. Ordered Silica Nanoparticles Grown on a Three-Dimensional Carbon Fiber Architecture Substrate with Siliconborocarbonitride Ceramic as a Thermal Barrier Coating. *ACS Appl. Mater. Interfaces* **2016**, *8* (6), 4216–4225. https://doi.org/10.1021/acsami.5b12140.

(193)   Al-Saleh, M. H.; Sundararaj, U. Review of the Mechanical Properties of Carbon Nanofiber/Polymer Composites. *Composites Part A: Applied Science and Manufacturing* **2011**, *42* (12), 2126–2142. https://doi.org/10.1016/j.compositesa.2011.08.005.

(194)   Jin, F.-L.; Park, S.-J. Preparation and Characterization of Carbon Fiber-Reinforced Thermosetting Composites: A Review. *Carbon letters* **2015**, *16* (2), 67–77. https://doi.org/10.5714/CL.2015.16.2.067.

(195)   Gabrion, X.; Placet, V.; Trivaudey, F.; Boubakar, L. About the Thermomechanical Behaviour of a Carbon Fibre Reinforced High-Temperature Thermoplastic Composite. *Composites Part B: Engineering* **2016**, *95*, 386–394. https://doi.org/10.1016/j.compositesb.2016.03.068.

(196)   Wolfrum, J.; Eibl, S.; Lietch, L. Rapid Evaluation of Long-Term Thermal Degradation of Carbon Fibre Epoxy Composites. *Composites Science and Technology* **2009**, *69* (3–4), 523–530. https://doi.org/10.1016/j.compscitech.2008.11.018.

(197) Zhou, F.; Zhang, J.; Song, S.; Yang, D.; Wang, C. Effect of Temperature on Material Properties of Carbon Fiber Reinforced Polymer (CFRP) Tendons: Experiments and Model Assessment. *Materials* **2019**, *12* (7), 1025. https://doi.org/10.3390/ma12071025.

(198) Yu, B.; Kodur, V. Effect of Temperature on Strength and Stiffness Properties of Near-Surface Mounted FRP Reinforcement. *Composites Part B: Engineering* **2014**, *58*, 510–517. https://doi.org/10.1016/j.compositesb.2013.10.055.

(199) Zhang, X.; Fan, X.; Yan, C.; Li, H.; Zhu, Y.; Li, X.; Yu, L. Interfacial Microstructure and Properties of Carbon Fiber Composites Modified with Graphene Oxide. *ACS Appl. Mater. Interfaces* **2012**, *4* (3), 1543–1552. https://doi.org/10.1021/am201757v.

(200) Dhakate, S. R.; Bahl, O. P. Effect of Carbon FIber Surface Functional Groups on the Mechanical Properties of Carbon–Carbon Composites with HTT. **2003**, 11.

(201) Yao, S.-S.; Jin, F.-L.; Rhee, K. Y.; Hui, D.; Park, S.-J. Recent Advances in Carbon-Fiber-Reinforced Thermoplastic Composites: A Review. *Composites Part B: Engineering* **2018**, *142*, 241–250. https://doi.org/10.1016/j.compositesb.2017.12.007.

(202) Smith, R. J.; Long, C. T.; Grunlan, J. C. Transparent Polyelectrolyte Complex Thin Films with Ultralow Oxygen Transmission Rate. *Langmuir* **2018**, *34* (37), 11086–11091. https://doi.org/10.1021/acs.langmuir.8b02391.

(203) Wang, Q.; Schlenoff, J. B. The Polyelectrolyte Complex/Coacervate Continuum. *Macromolecules* **2014**, *47* (9), 3108–3116. https://doi.org/10.1021/ma500500q.

(204) Rumyantsev, A. M.; Jackson, N. E.; de Pablo, J. J. Polyelectrolyte Complex Coacervates: Recent Developments and New Frontiers. *Annu. Rev. Condens. Matter Phys.* **2021**, *12* (1), 155–176. https://doi.org/10.1146/annurev-conmatphys-042020-113457.

(205) Chiang, H.; Kolibaba, T. J.; Eberle, B.; Grunlan, J. C. Super Gas Barrier of a Polyelectrolyte/Clay Coacervate Thin Film. *Macromol. Rapid Commun.* **2021**, *42* (4), 2000540. https://doi.org/10.1002/marc.202000540.

(206) Kelly, K. D.; Schlenoff, J. B. Spin-Coated Polyelectrolyte Coacervate Films. *ACS Appl. Mater. Interfaces* **2015**, *7* (25), 13980–13986. https://doi.org/10.1021/acsami.5b02988.

(207) Carosio, F.; Alongi, J. Flame Retardant Multilayered Coatings on Acrylic Fabrics Prepared by One-Step Deposition of Chitosan/Montmorillonite Complexes. *Fibers* **2018**, *6* (2), 36. https://doi.org/10.3390/fib6020036.